Chapter 5

Syntheses, spectral characterization and antidiabetic activities of vanadium(IV/V) complexes with bi- and tridentate ligands (In situ reaction)

1 Introduction

Metal compounds have been used in medicine since the olden days. Though, organic medicines have generally dominated modern medicinal chemistry and pharmacology. Inorganic medicinal chemistry is a growing research area whose modern development has been prompted by the serendipidous discovery of the anti-cancer activity of cisplatin. This development utilizes the singular properties of metal ions for designing metal compounds with medicinal applications. The medicinal chemistry of vanadium has been mainly focused on improving biodistribution, oral bioavailability and acceptability of the compounds [1-8]. Various vanadium complexes with different coordination sites have been suggested to have *in-vitro* and *in-vivo* insulin-mimetic activity [9-17].

Aroylhydrazones and their transition metal complexes are well studied due to their varied applications in functional materials and medicinal chemistry [18-22]. The hydrazones have drawn attention for their biological potential [23-25]. These ligands coordinate with metal ions in different ways [26]. The glucose lowering effect of vanadium complexes has been a subject of medical research and several vanadium complexes have been examined as candidates for antidiabetic treatment [27]. The insulin enhancing activity of bis(maltato)oxovanadium(IV) inspired the search for plausible vanadium complexes for the treatment of type II diabetes [28].

This chapter describes syntheses, spectral characterization and electrochemical behavior of eleven new vanadium (V) complexes with NNN/ONO tridentate ligands and different co-ligands. In complexes **1-3** 2,2'-bis(pyridylmethyl)amine (BPA) was used as pro-ligand and water, 2,2-bipyridyl and 1,10-phenanthroline as a co-ligand. Similarly, for complexes,**4-11** aroylhydrazones was used as pro-ligand and maltol or ethyl maltols as ancillary ligands. The formulations of these newly synthesized complexes are as:$[VO(BPA)(OH_2)_2]SO_4$ (**1**), $[VO(BPA)(bipy)]SO_4$ (**2**), $[VO(BPA)(phen)]SO_4$(**3**), $[VO(L^1)(Mol)]$ (**4**), $[VO(L^2)(Mol)]$ (**5**), $[VO(L^3)(Mol)]$ (**6**), $[VO(L^4)(Mol)]$ (**7**), $[VO(L^1)(E\text{-}mol)]$ (**8**), $[VO(L^2)(E\text{-}mol)]$ (**9**), $[VO(L^3)(E\text{-}mol)]$ (**10**) and $[VO(L^4)(E\text{-}mol)]$ (**11**) (2,2'-bis(pyridylmethyl)amine (BPA), L^1-L^4 = aroylhydrazones and Mol = maltol and E-mol = ethyl maltol). Computational density functional theory has been used to establish the stable geometrical form of used ligand and its complexes. Quantum computational density functional theory (DFT) has also yielded significant electronic structural parameters. Besides, their antidiabetic activity was having been investigated.

2 Experimental

2.1 Materials and physical measurements

$VOSO_4.5H_2O$ (Across Organics), 2,2'-bis(pyridylmethyl)amine (Aldrich), 1,10-phenanthroline (S.D. Fine), 2,2-bipyridyl (CDH), Maltol (Sigma Aldrich), Ethyl Maltol (Sigma Aldrich), and DMSO (S.D. Fine) were reagent grade and used as purchased from commercial sources without any further purification. Infrared (IR) spectra were recorded on a Perkin Elmer Fourier transform IR (FTIR) spectrum RX 1 Spectrometer as KBr pellets. Mass spectra of the complexes were recorded on Trace GC ultra DSQ II. Elemental analyses of C, H and N were determined using a Perkin Elmer series-II 2400 elemental analyzer. Powder XRD was done by the Rigaku Desktop X-Ray diffractometer. Electronic spectra were recorded on a Perkin Elmer Lambda 35 UV-Vis spectrometer. ESR spectra of complexes were recorded with a Varian E-line Century Series X-band spectrometer. ESR measurements were carried out using an X-band instrument at ESR laboratory, SAIF, IIT, Bombay, at room temperature (RT) and liquid nitrogen temperature (LNT). Tetracyanoethylene (TCNE) was used as a reference (g = 2.0027). Electrochemical data were collected using a BAS-100 Epsilon Electrochemical Analyzer on compounds **1-11** in the DMSO solution using Ag/AgCl as a reference electrode and glassy carbon as a working electrode. Tetrabutylammonium perchlorate (TBAP) was used as a supporting electrolyte. ESI-mass spectra were recorded on Waters Q-ToF micro mass. A simultaneous TGA was performed using TG-DTA 6300 INCARP EXSTAR 6000 at a heating rate of 10 °C/min in the temperature range of 25-600°C with a nitrogen atmosphere maintained throughout the measurement. Magnetic susceptibility measurements at room temperature were made on a Gouy balance using mercury(II) tetrathiocynatocobaltate(II) as the calibrating agent (χ_g= 16.44×10^{-6} cgs units).Molar conductivities of the freshly prepared 1.0×10^{-3} M DMSO solutions were measured on a Systronics Conductivity 308 TDS meter.

2.2. Synthesis

2.2.1 Synthesis of $[VO(BPA)(OH_2)_2]SO_4$ 1

Vanadyl sulphate pentahydrate (0.254 g, 1mmol) in 10 mL and 2,2'-bis(pyridylmethyl)amine (BPA) (0.1 mL, 1 mmol) in 1 mL methanol were mixed and the

reaction mixture was refluxed for 3 hrs at 75 °C. A light blue precipitate was formed which was filtered, washed with methanol and dried in calcium chloride desiccator.

Yield: 65 %. Anal. Calc. (%) for $C_{12}H_{16}N_3O_3V$ (M = 397.27 g mol^{-1}): C, 36.27; H, 4.05; N, 10.57 %. Found: C, 36.23; H, 4.09; N, 10.55 %. FTIR bands (KBr, cm^{-1}): ν(C=N) 1608 vs, ν(V=O) 978 vs, ν(V-O) 483 m, ν(V-N) 430 cm^{-1}. ESI Mass (m/z) = 399.14.

2.2.2. Synthesis of [VO(BPA)(bipy)]SO_4 2

Vanadyl sulphate pentahydrate (0.254 g, 1 mmol) in 10 mL water and BPA (0.1mL, 1 mmol) were mixed and stirred for 1 hrs followed by the addition of an aqueous solution of 2,2-bipyridyl (0.156 g, 1 mmol). The reaction mixture was further refluxed for 3 hrs at 75 °C. The colour of the solution changed to blue and a blue precipitate was obtained which was filtered, washed with methanol and air-dried. The desired complex was stored in calcium chloride desiccators.

Yield: 70 %. Anal. Calc. for $C_{22}H_{20}N_5O_5SV$ (M = 517.43 g mol^{-1}): C, 51.06; H, 3.89; N, 13.53 %. Found: C, 51.10; H, 3.86; N, 13.57 %. FTIR bands (KBr, cm^{-1}): ν ν(C=N) 1610 vs, ν(V=O) 921 vs, ν(V-O) 476 m, ν(V-N) 440 cm^{-1}. ESI Mass (m/z) = 519.55.

2.2.3 Synthesis of [VO(BPA)(phen)]SO_4 3

The complex was synthesized by a similar procedure to **2**. Using 1,10-phenanthroline (0.198 g, 1 mmol) in place of 2,2-bipyridyl.

Yield: 73 %. Anal. Calc.for $C_{24}H_{20}N_5O_5SV$ (M = 541.45 g mol^{-1}): C, 53.23; H, 3.72; N, 12.93 %. Found: C, 53.26; H, 3.77; N, 12.95 %. FTIR bands (KBr, cm^{-1}): ν(C=N) 1608 vs, ν(V=O) 975 vs, ν(V-O) 482 m, ν(V-N) 431 cm^{-1}. ESI Mass (m/z) = 542.12.

2.2.4 Synthesis of [VO(L^1)(Mol)] 4

To a MeOH solution (20 mL) of 5-nitrosalicylaldehyde (0.167 g, 1.00 mmol), benzhydrazide (0.136 g, 1.00 mmol) was added and the resulting solution was heated to reflux for 1 hrs at 75 °C. The reaction mixture was cooled at room temperature. To this solution, maltol (0.126 g, 1.00 mmol) and $VOSO_4$ (0.163 g, 1.00 mmol) dissolved in MeOH were added. The reaction mixture was further stirred for 3 hrs to give a brown solution and

allowed to evaporate slowly in the air. After one weak, dark brown product separated, this was filtered and dried in a calcium chloride desiccator.

Yield: 73 %. Anal. Calc. for $C_{20}H_{14}N_3O_8V$ (M = 475.02 g mol^{-1}): C, 50.54; H, 2.97; N, 8.84 %. Found: C, 50.57; H, 2.99; N, 8.82 %. FTIR (KBr, cm^{-1}): ν(C=O) 1632 vs, ν(C=N) 1604 vs, ν(V=O) 952 vs, ν(V-O) 432 m, ν(V-N) 417 cm^{-1}. ESI Mass (m/z) = 475.73.

2.2.5 Synthesis of [VO(L^2)(Mol)] 5

To a MeOH solution (20 mL) of 5-bromosalicylaldehyde (0.167 g, 1.00 mmol), 3-hydroxylbenzohydrazide (0.152 g, 1.00 mmol) was added and the resulting solution was heated to reflux for 1 hrs at 75 °C. The reaction mixture was cooled at room temperature. To this solution, maltol (0.126g, 1.00 mmol) and $VOSO_4$ (0.163 g, 1.00 mmol) dissolved in MeOH were added. The reaction mixture was further stirred for 3 hrs to give a brown solution and allowed to separate, which was filtered and dried in a calcium chloride desiccator.

Yield: 73%. Anal. Calc. for $C_{20}H_{14}BrN_2O_7V$ (M = 525.18 g mol^{-1}): C, 45.74; H, 2.69; N, 5.33 %. Found: C, 45.76; H, 2.65; N, 5.36. %. FTIR (KBr, cm^{-1}): ν(C=O) 1621 vs, ν(C=N) 1596 vs, ν(V=O) 975 vs, ν(V-O) 484 m, ν(V-N) 445 cm^{-1}. ESI Mass (m/z) = 524.85.

2.2.6 Synthesis of [VO(L^3)(Mol)] 6

To a MeOH solution (20 mL) of 5-chlorosalicylaldehyde (0.156 g, 1.00 mmol), 3-hydroxylbenzohydrazide (0.152 g, 1.00 mmol) was added and the resulting solution was heated to reflux for 1 hrs at 75 °C. The reaction mixture was cooled at room temperature. To this solution, maltol (0.126g, 1.00 mmol) and $VOSO_4$ (0.163 g, 1.00 mmol) dissolved in MeOH were added. The reaction mixture was further stirred for 3 hrs to give a brown solution and allowed to separate, which was filtered and dried in a calcium chloride desiccator.

Yield: 73 %. Anal. Calc. For $C_{20}H_{14}ClN_2O_7V$ (M = 480.73 g mol^{-1}): C, 49.97; H, 2.94; N, 5.83 %. Found: C, 49.99; H, 2.96; N, 5.81 %. FTIR (KBr, cm^{-1}): ν(C=O) 1632, ν(C=N) 1606 vs, ν(V=O) 972 vs, ν(V-O) 459 m, ν(V-N) 409 cm^{-1}. ESI Mass (m/z) = 481.97.

2.2.7 Synthesis of [VO(L^4)(Mol)] 7

To a MeOH solution (20 mL) of 5-chlorosalicylaldehyde (0.156 g, 1.00 mmol), pivalohydrazide (0.116 g, 1.00 mmol) was added and the resulting solution was heated to reflux for 1 hrs at 75 °C. The reaction mixture was cooled at room temperature. To this solution, maltol (0.126g, 1.00 mmol) and $VOSO_4$ (0.163 g, 1.00 mmol) dissolved in MeOH were added. The reaction mixture was further stirred for 3 hrs to give a brown solution and allowed to separate, which was filtered and dried in a calcium chloride desiccator.

Yield: 73 %. Anal. Calc. for $C_{18}H_{18}ClN_2O_6V$ (M = 444.74 g mol^{-1}): C, 48.61; H, 4.08; N, 6.30 %. Found: C, 48.64; H, 4.10; N, 6.33 %. FTIR (KBr, cm^{-1}): ν(C=O) 1633 vs, ν(C=N) 1605 vs, ν(V=O) 973 vs, ν(V-O) 444 m, ν(V-N) 410 cm^{-1}. ESI Mass (m/z) = 446.94.

2.2.8 Synthesis of [VO(L^1)(E-mol)] 8

To a MeOH solution (20 mL) of 5-nitrosalicylaldehyde (0.167 g, 1.00 mmol), Benzohydrazide (0.136 g, 1.00 mmol) was added and resulting solution was heated to reflux for 1 hrs at 75 °C. The reaction mixture was cooled at room temperature. To this solution ethyl maltol (0.140 g, 1.00 mmol) and $VOSO_4$ (0.163 g, 1.00 mmol) dissolved in MeOH were added. The reaction mixture was further stirred for 3 hrs to give a brown solution and allowed to separate out, which was filtered and dried in calcium chloride desiccators.

Yield: 73 %. Anal. Calc. for $C_{21}H_{16}N_3O_8V$ (M = 489.31 g mol^{-1}): C, 51.55; H, 3.30; N, 8.59 %. Found: C, 51.50; H, 3.33; N, 8.56 %. FTIR (KBr, cm^{-1}): ν(C=O) 1633 vs, ν(C=N) 1602 vs, ν(V=O) 957 vs, ν(V-O) 483 m, ν(V-N) 436 cm^{-1}. ESI Mass (m/z) = 491.50.

2.2.9 Synthesis of [VO(L^2)(E-mol)] 9

To a MeOH solution (20mL) of 5-bromosalicylaldehyde (0.167 g, 1.00 mmol), 3-hydroxybenzohydrazide (0.150 g, 1.00 mmol) was added and the resulting solution was heated to reflux for 1 hrs 75 °C. The reaction mixture was cooled at room temperature. To this solution ethylmaltol (0.140g, 1.00 mmol) and $VOSO_4$ (0.163 g, 1.00 mmol) were added to the above solution. The reaction mixture was further stirred for 3 hrs to give a brown solution and allowed to separate, which was filtered and dried in a calcium chloride desiccator.

Yield: 73 %. Anal. Calc. For $C_{21}H_{16}BrN_2O_7V$ (M = 539.21 g mol^{-1}): C, 46.78; H, 2.99; N, 5.20 %. Found: C, 46.80; H, 2.96; N, 5.15 %. FTIR (KBr, cm^{-1}): ν(C=O) 1635 vs, ν(C=N) 1603 vs, ν(V=O) 971 vs, ν(V-O) 461 m, ν(V-N) 415 cm^{-1}. ESI Mass (m/z) 539.16.

2.2.10 Synthesis of [VO(L^3)(E-mol)] 10

To a MeOH solution (20mL) of 5-chlorosalicylaldehyde (0.167 g, 1.00 mmol), 3-hydroxylbenzohydrazide (0.150 g, 1.00 mmol) was added and the resulting solution was heated to reflux for 1 hrs 75 °C. The reaction mixture was cooled at room temperature. To this solution ethylmaltol (0.140g, 1.00 mmol) and $VOSO_4$ (0.163 g, 1.00 mmol) were added to the above solution. The reaction mixture was further stirred for 3 hrs to give a brown solution and allowed to separated, which was filtered and dried in a calcium chloride desiccator.

Yield: 73 %. Anal. Calc. for $C_{21}H_{16}ClN_2O_7V$ (M = 494.76 g mol^{-1}): C, 50.98; H, 3.26; N, 5.66 %. Found: C, 50.92; H, 3.25; N, 5.62 %. FTIR (KBr, cm^{-1}): ν(C=O) 1632 vs, ν(C=N) 1607 vs, ν(V=O) 972 vs, ν(V-O) 460 m, ν(V-N) 410 cm^{-1}. ESI Mass (m/z) = 496.30.

2.2.11 Synthesis of [VO(L^4)(E-mol)] 11

To a MeOH solution (20mL) of 5-chlorosalicylaldehyde (0.167g, 1.00 mmol), pivalohydrazide (0.116g, 1.00mmol) was added and the resulting solution was heated to reflux for 1 hrs 75 °C. The reaction mixture was cooled at room temperature. To this solution ethylmaltol (0.140g, 1.00 mmol) and $VOSO_4$ (0.163 g, 1.00 mmol) were added to the above solution. The reaction mixture was further stirred for 3 hrs to give a brown solution and allowed to separate, which was filtered and dried in a calcium chloride desiccator.

Yield: 73 %. Anal. Calc. for $C_{19}H_{20}ClN_2O_6V$ (M = 458.77 g mol^{-1}): C, 49.74; H, 4.39; N, 6.11 %. Found: C, 49.72; H, 4.43; N, 6.07 %. FTIR (KBr, cm^{-1}): ν(C=O) 1657 vs, ν(C=N) 1605 vs, ν(V=O) 965 vs, ν(V-O) 432 m, ν(V-N) 417 cm^{-1}. ESI Mass (m/z) = 460.27.

2.3. Antidiabetic activity

2.3.1 α-Glucosidase inhibition activity

The α-glucosidase inhibitory activity assay was performed as described previously [29]. In brief, rat-intestinal acetone powder was dissolved in 100 mL of saline water and sonicated properly at 4°C. After sonication, the suspension was centrifuged (3,000 rpm, 4°C,

30 minutes) and the resulting supernatant was used for the assay. A reaction mixture containing 50 µL of phosphate buffer (50 mM; pH 6.8), 50 µL of rat α-glucosidase and 50 µL sample of varying concentrations (100-800 µg/ mL) was pre-incubated for 5 min at 37°C, and then 50 µL of 3 mM pNPG was added to the mixture as a substrate. After incubation at 37°C for 30 min, enzymatic activity was quantified by measuring the absorbance at 405 nm in a microtiter plate reader (Bio-TEK, USA). Acarbose was used as standard and experiments were done in triplicates. Acarbose was used as a reference and experiments were carried out in triplicate. The inhibition percentage (%) was calculated as follows:

$$\% \text{ inhibition} = \frac{[A_C - A_S]}{A_C \times 100}$$

where A_C is the absorbance of the control and A_S is the absorbance of the tested sample. The concentration of inhibitor required to inhibit fifty percent of enzyme activity under the mentioned assay conditions is defined as the IC_{50} value.

2.3.2. α-Amylase inhibition activity

Pancreatic α-amylase assay was adopted from Apostolidis et al. [30]. 50 µL of different dilutions of test compounds and 50 µL of 0.02 M sodium phosphate buffer (pH 6.9 with 0.006 M sodium chloride) containing α-amylase solution (0.5 mg/ mL) were incubated at 25°C for 10 min. After pre-incubation, 50 µL of 1% starch solution in 0.02 M sodium phosphate buffer (pH 6.9 with 0.006 M sodium chloride) was added to each tube. The reaction was incubated at 25°C for 10 min. The reaction was stopped with 100 µL of DNS colour reagent. The microplate was incubated (85-90°C) for 10 min to develop colour and left to cool at room temperature. The reaction mixture was diluted with 105 µL of distilled water. Enzymatic activity was quantified by measuring the absorbance at 540 nm in a microtiter plate reader (Bio-TEK, USA). Acarbose was used as standard and experiments were done in triplicates. Acarbose was used as a reference. The α-amylase activity was estimated using the equation:

$$\% \text{ inhibition} = \frac{[A_C - A_S]}{A_C \times 100}$$

where A_C is the absorbance of the control and A_S is the absorbance of the tested sample. The concentration of inhibitor required to inhibit fifty percent of enzyme activity under the mentioned assay conditions is defined as the IC_{50} value.

3 Results and Discussion

3.1 Synthesis and Spectroscopic Properties

Complexes **1** was synthesized by taking aqueous vanadyl sulphate solution and methanolic solution of 2,2'-bis(pyridylmethyl)amine in a 1:1 ratio (Scheme 1). Similarly, mixed ligand complexes **2** and **3** were synthesized by taking a methanolic solution of vanadyl sulphate, 2,2'-bis(pyridylmethyl)amine and 1,10-phenanthroline or 2,2-bipyridyl in a 1:1:1 molar solution. The resulting precipitate was filtered off, washed with methanol and dried in calcium chloride desiccators. Likewise, the oxidovanadium(V) complexes **4-11** [VO(L^{1-4}) (Mol/E-mol)] (L^{1-4} are four tridentate ligands and Mol/E-mol are maltol and ethyl maltol, respectively). The tridentate L^{1-4} aroylhydrazones ligands have not been pre isolated (L^1 = (E)-N'-(2-hydroxy-5-nitrobenzylidene)benzohydrazide, L^2 = (E)-N'-(5-bromo-2 hydroxybenzylidene)-3-hydroxybenzohydrazide, L^3 = (E)-N'-(5-chloro-2-hydroxybenzylidene)-3-hydroxybenzohydrazideand L^4 =(E)-N'-(5-chloro-2-hydroxybenzylidene)pivalohydrazide). In situ syntheses of aroylhydrazones are shown in Scheme 2 and 3. The complexes have been isolated in good yield from a single step reaction of salicylaldehydes, hydrazides, $VOSO_4$ and maltol in a mixture of solvents using air as an oxidizing agent. The automatic oxidation is due to lowering of the reduction potential at the vanadium centre owing to OO^- ion coordination [31]. The five negative charge appear from the phenolate oxygen O1(-1), the enolate oxygen O2(-1), the oxo oxygen O3(-2) of tridentate hydrazone and oxygen O4(-1) of maltol or ethyl maltol. The synthetic routes of complexes are shown in Scheme 2. These complexes were characterized by elemental analysis, Powder XRD, FTIR, UV-Vis, TG-DTA analyses, CV and EPR spectroscopy. All the complexes are air-stable. The complexes are insoluble in water, hexane, benzene, and petroleum ether but soluble in DMSO, DMF, and acetonitrile. Molar conductivity (Λ_m/S) of value for complexes **1-3** all complexes in DMSO solution (3.0×10^{-3}mol L^{-1}) was 110-130 Ω^{-1} cm^2 mol^{-1}corresponding to a 1:1 electrolyte [32-34]. The other complexes **4-11** are non-electrolytic in nature having value in the range of 27.52-38.50 Ω^{-1} cm^2 mol^{-1}.

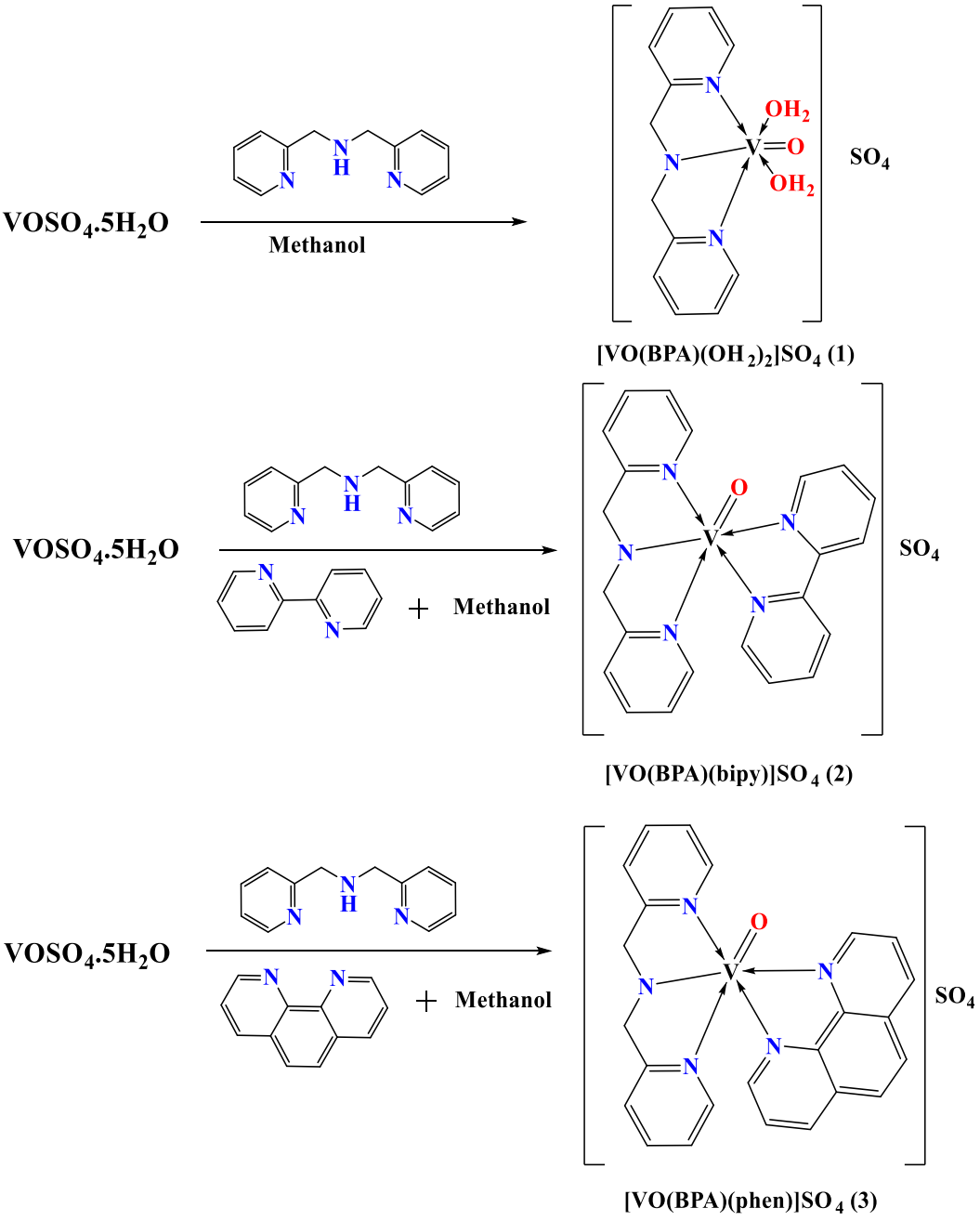

Scheme 1 Synthetic route of complexes **1-3**.

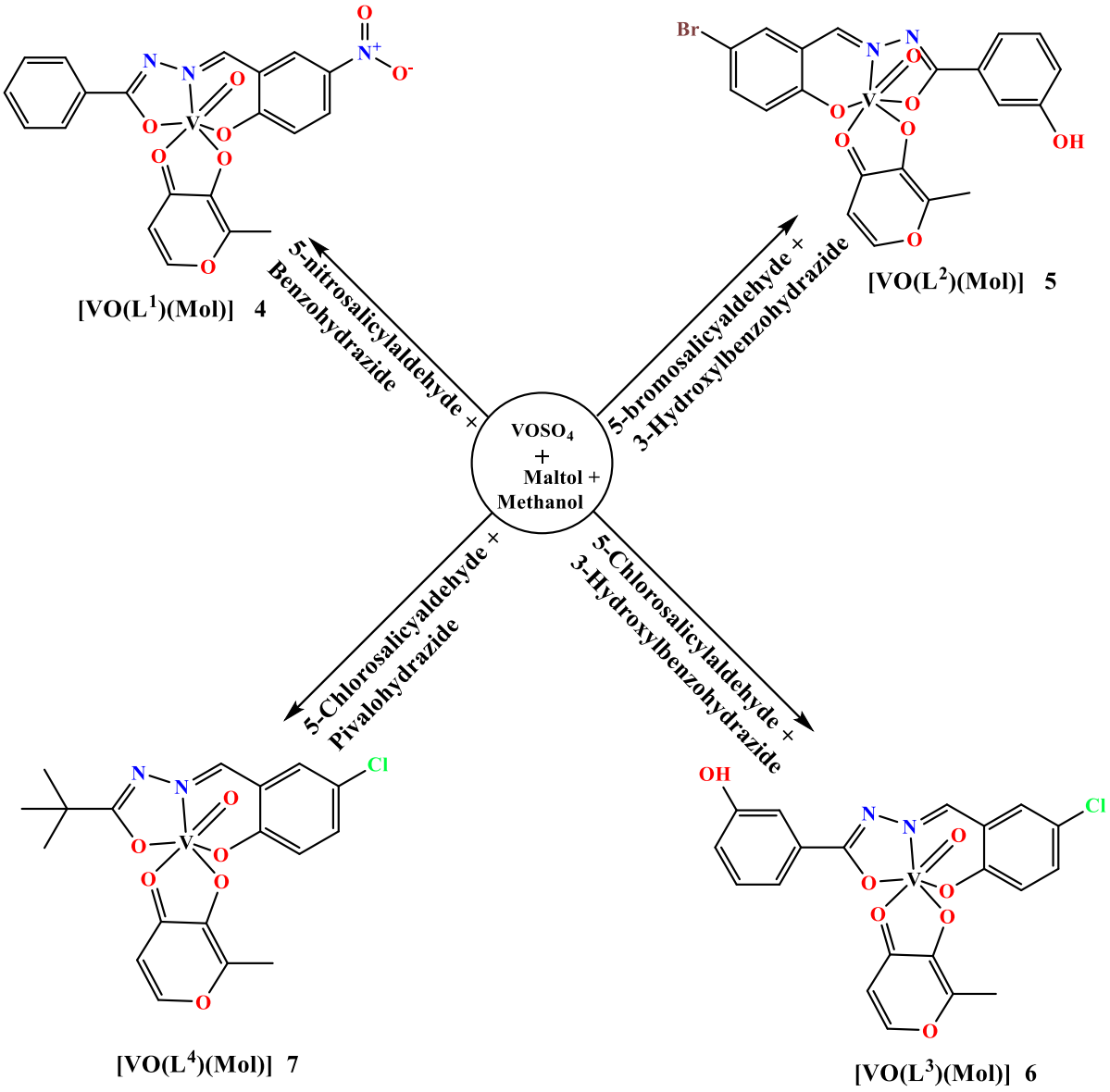

Scheme 2 Synthetic route of complexes **4-7** (with maltol).

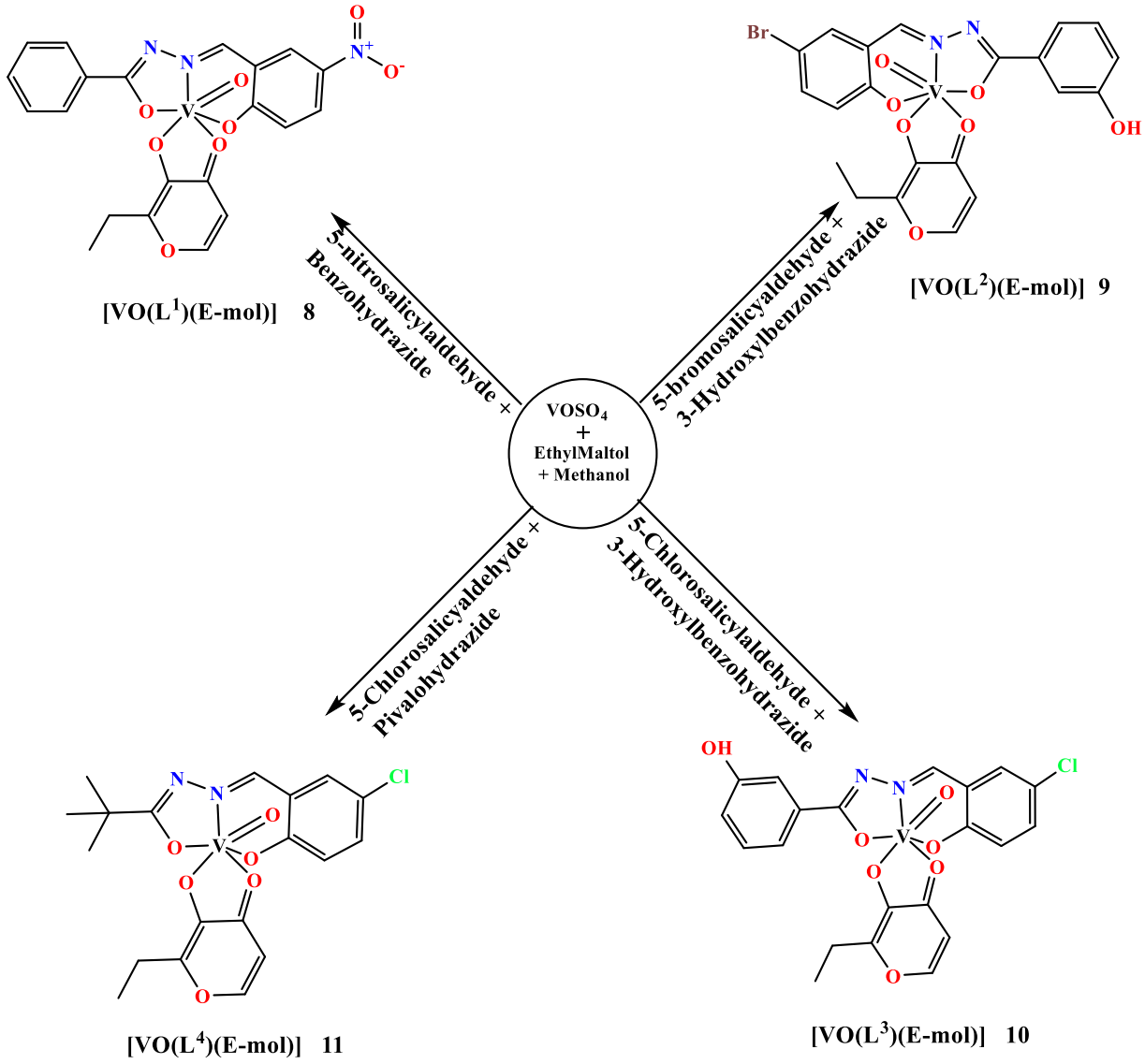

Scheme 3 Synthetic route of complexes **8-11** (with Ethyl maltol).

3.2 Powder XRD

X-ray diffractograms are used to determine the phase purity of transition metal complexes **1-3**. Diffraction was performed to obtain evidence about the structure of the metal complexes. X-ray diffractogram of complexes was scanned in the range 4-85 degrees. The diffractogram obtained for the oxidovanadium(IV) complexes were given in Fig. **1-3**. Each peak has been determined by cell parameters and corresponding values. The XRD patterns the major peak which showed relative intensity greater than 10% indexed by computer program [35]. Sharp peaks were observed in diffractograms of all complexes which suggests

that the complexes formed are crystalline [36]. The diffraction peaks show that these complexes are in the nanometres range.

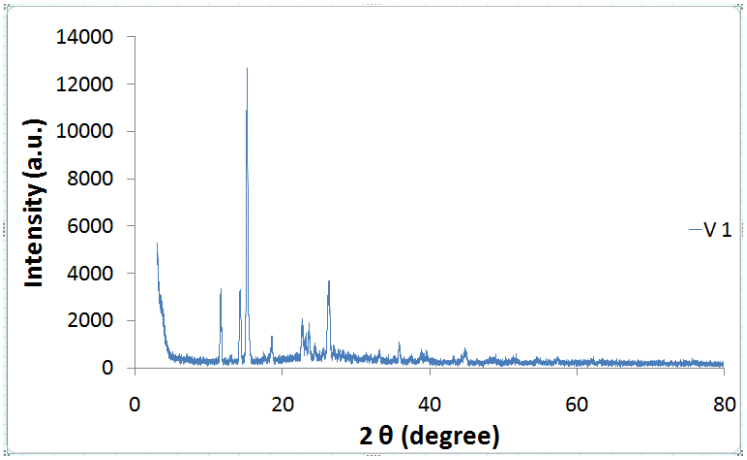

Fig. 1. Powder XRD data of complex **1.**

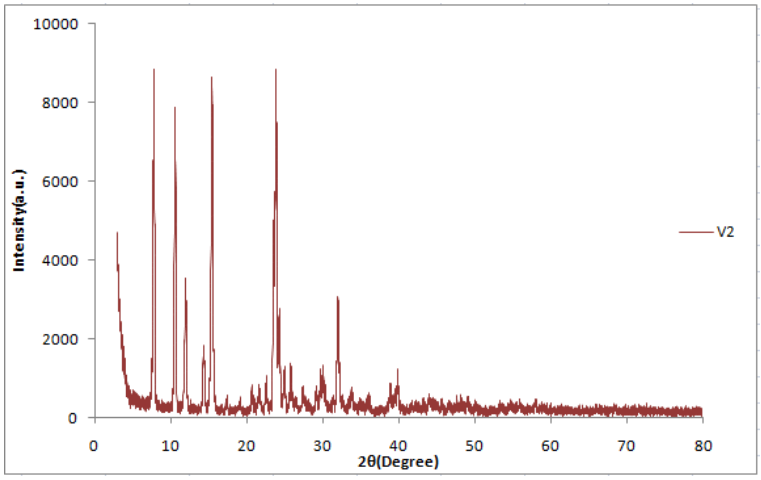

Fig. 2. Powder XRD data of complex **2.**

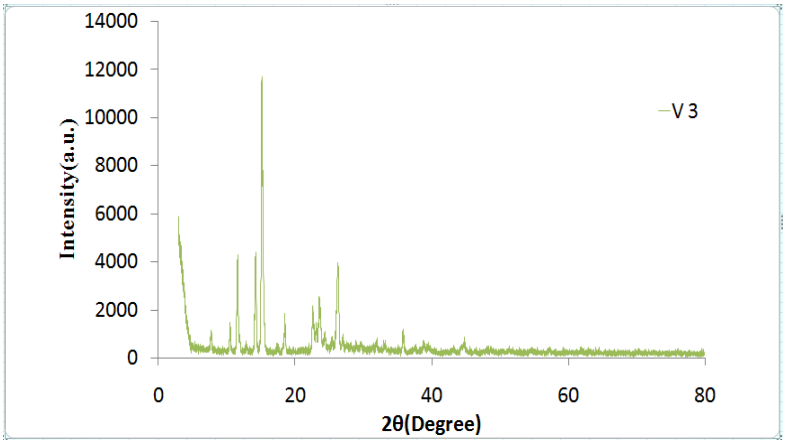

Fig. 3. Powder XRD data of complex **3.**

3.3. FTIR Analysis

3.3.1 FTIR spectra of complexes 1-3

The FTIR spectra of complexes should some additional structural information. The FTIR spectrum of complexes **1-11** was recorded in the range of 400-4000 cm^{-1}. In FTIR spectrum of complexes **1-3,** a strong band observed in the region of 978-956 cm^{-1}, which is consistent with six-coordinated vanadium complexes [37]. In all spectra, the band corresponding to υ(N-H) at ~ 3079 cm^{-1} is observed due to the tertiary amine moiety of BPA [38,39]. The IR spectrum of complex **1** shows a band at 3434 cm^{-1}, which can be attributed to the coordinated water molecules Fig. 4. The band corresponding to υ(C=N) of pyridyl moieties of the ligand is observed at ~ 1608 cm^{-1}, similarly, ionic sulphate shows the stretch mode in the range is 1153-1074 and 657-621 cm^{-1}. The band in the regions 476-483, and 430-440 cm^{-1} can be attributed to the stretching modes of the vanadium to ligand bonds, ν(V-O) and ν(V-N), respectively. The FTIR data of complexes **1-3** is given in Table 1. In complexes, the fingerprint region of the range 1200-1000 cm^{-1} becomes broadened to polypyridyl ligands Fig. 5 and 6.

Table 1 IR spectral data of complexes **1-3**.

Complex	ν(OH)	ν(N-H)	ν(C=N)	ν(V=O)	ν(V-O)	ν(V-N)
1	3434	3146	1608	978	483	430
2	-	3145	1610	921	476	440
3	-	3254	1608	975	482	431

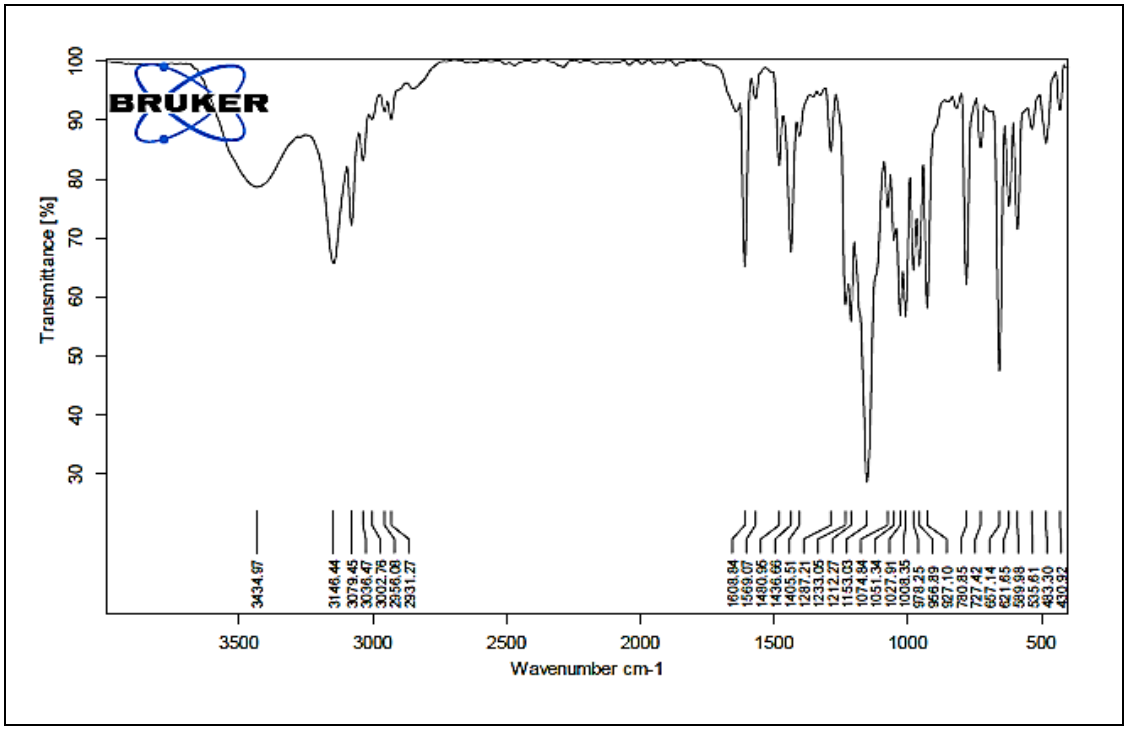

Fig. 4. FTIR spectrum of complex **1**.

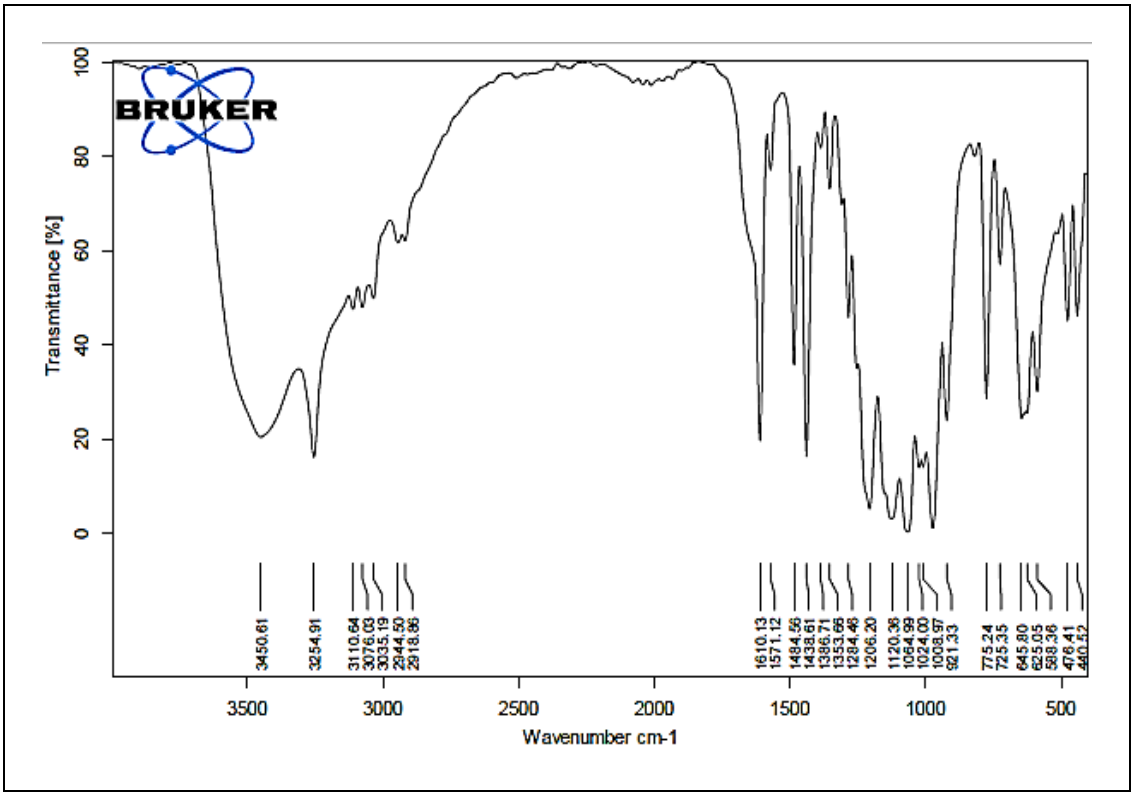

Fig. 5. FTIR spectrum of complex **2**.

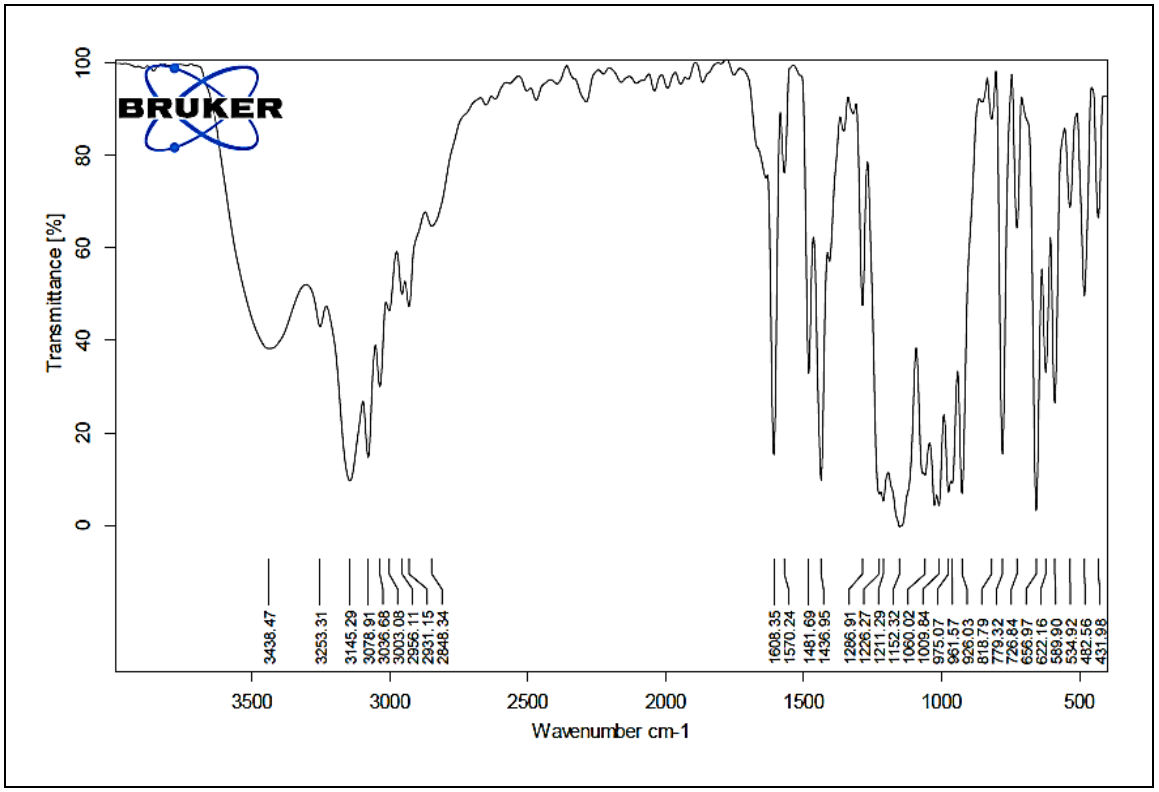

Fig. 6. FTIR spectrum of complex **3**.

3.3.2 FTIR Spectra of complexes 4-11

The FTIR spectra of complexes (**4-11**) the free aroylhydrazone ligands exhibit bonds in the spectral regions 3020-3185 cm^{-1} due to N-H stretching vibrations, respectively [40-42]. The FTIR data of complexes are given in Table 2. These absorption bands are absent in the present complexes, indicating the conversion of carbonyl moiety to an enolic moiety and resulting replacement of the phenolic moiety to enolic hydrogens [43]. A new band present at 1289-1303 cm^{-1} region in the complexes assigned to the ν(C-O) (enolato) stretching mode [44]. The absorption bands in the 1596-1606 cm^{-1} range, indicate the coordination of azomethine nitrogen to the vanadium. Moreover, the band in the regions 432-484, and 410-417cm^{-1} can be attributed to the stretching modes of the vanadium to ligand bonds, ν(V-O) and ν(V-N), respectively [45]. Besides, the complexes show a strong band in the 952-975cm^{-1} range owing to the complexes due to the terminal V=O stretching, reveals a hexacoordinated sphere around the vanadium center [46, 47]. The FTIR spectra of complexes **4-11** are shown in Fig. 7-14.

Table 2 FTIR spectral data of complexes **4-11**.

Complex	ν(OH)	ν(C=N)	ν(C=O)	ν(C-O)	ν(V=O)	ν(V-O)	ν(V-N)
4	3436	1604	1632	1289	952	432	417
5	3382	1596	1621	1301	975	484	445
6	3485	1606	1632	1300	972	459	409
7	3429	1605	1633	1298	973	444	410
8	-	1602	1633	1302	957	483	436
9	3425	1603	1635	1297	971	461	415
10	3428	1607	1632	1299	972	460	410
11	-	1605	1657	1303	965	432	417

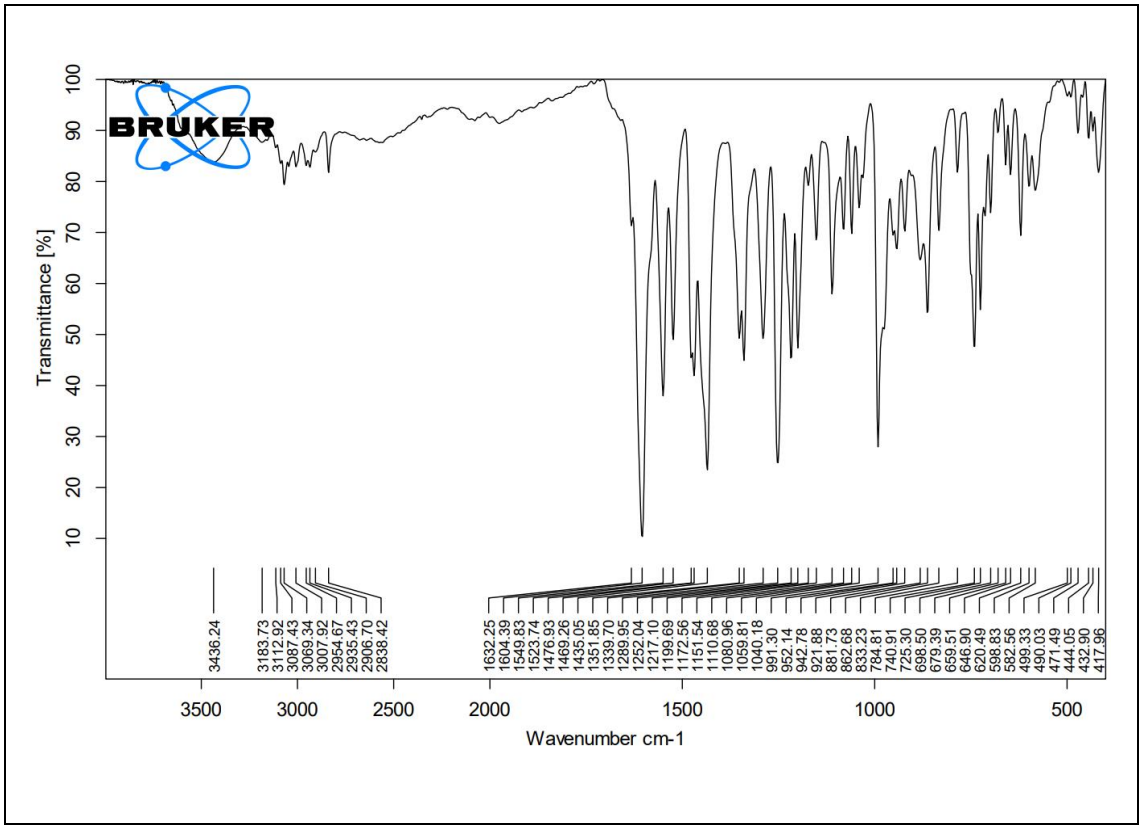

Fig. 7. FTIR spectrum of complex **4**.

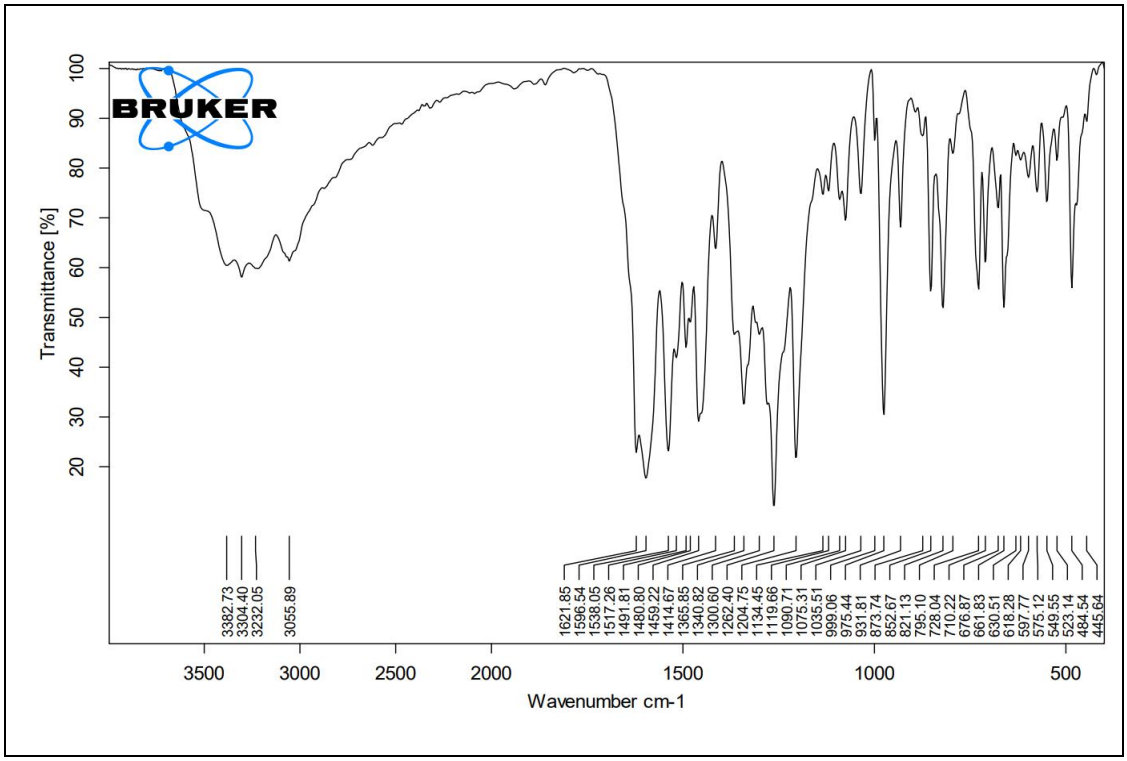

Fig. 8. FTIR spectrum of complex **5**.

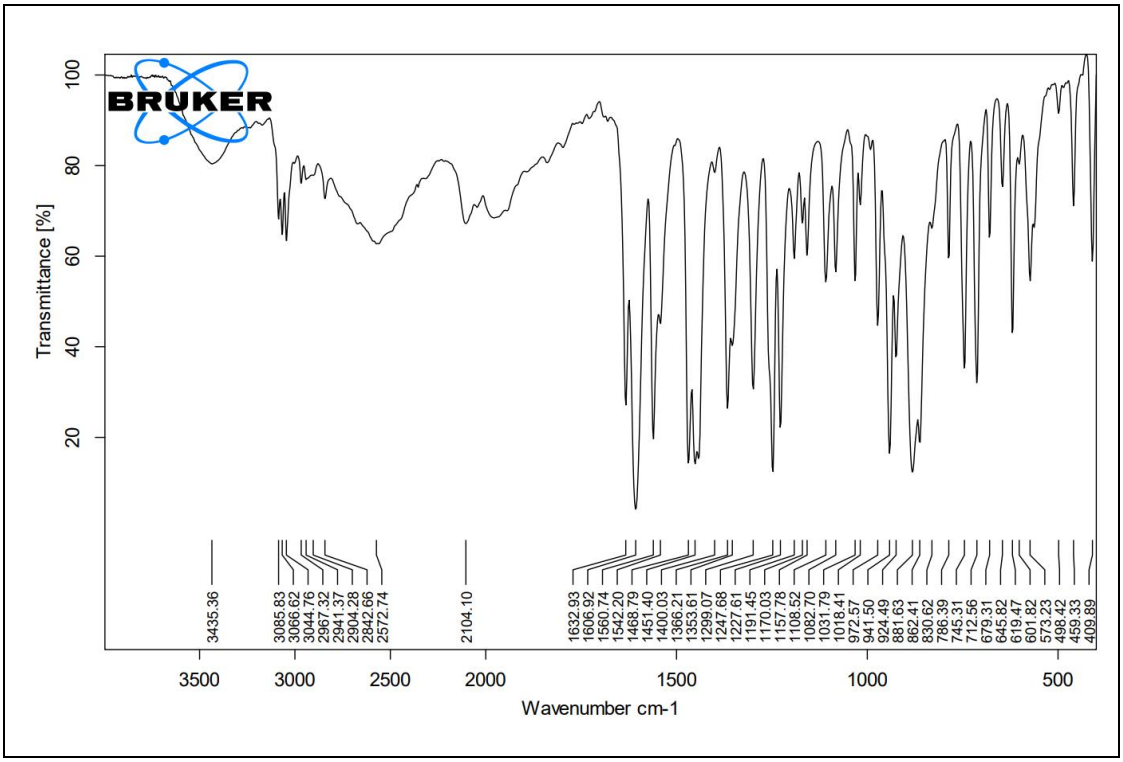

Fig. 9. FTIR spectrum of complex **6**.

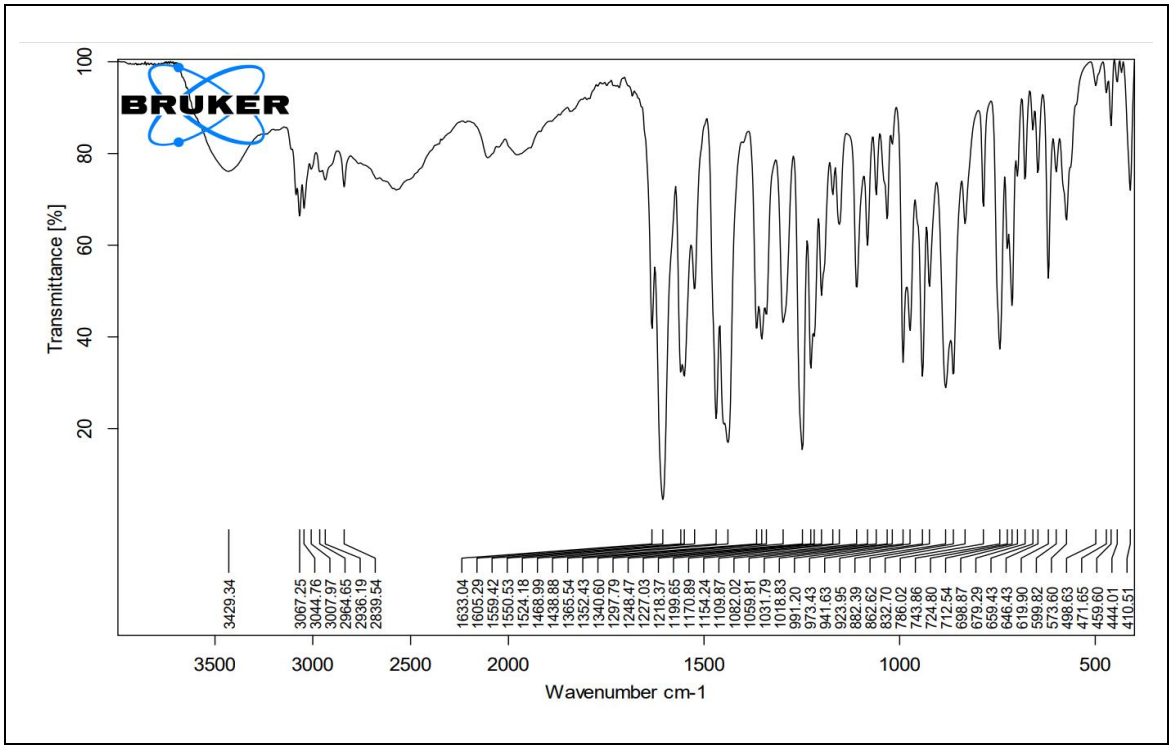

Fig. 10. FTIR spectrum of complex 7.

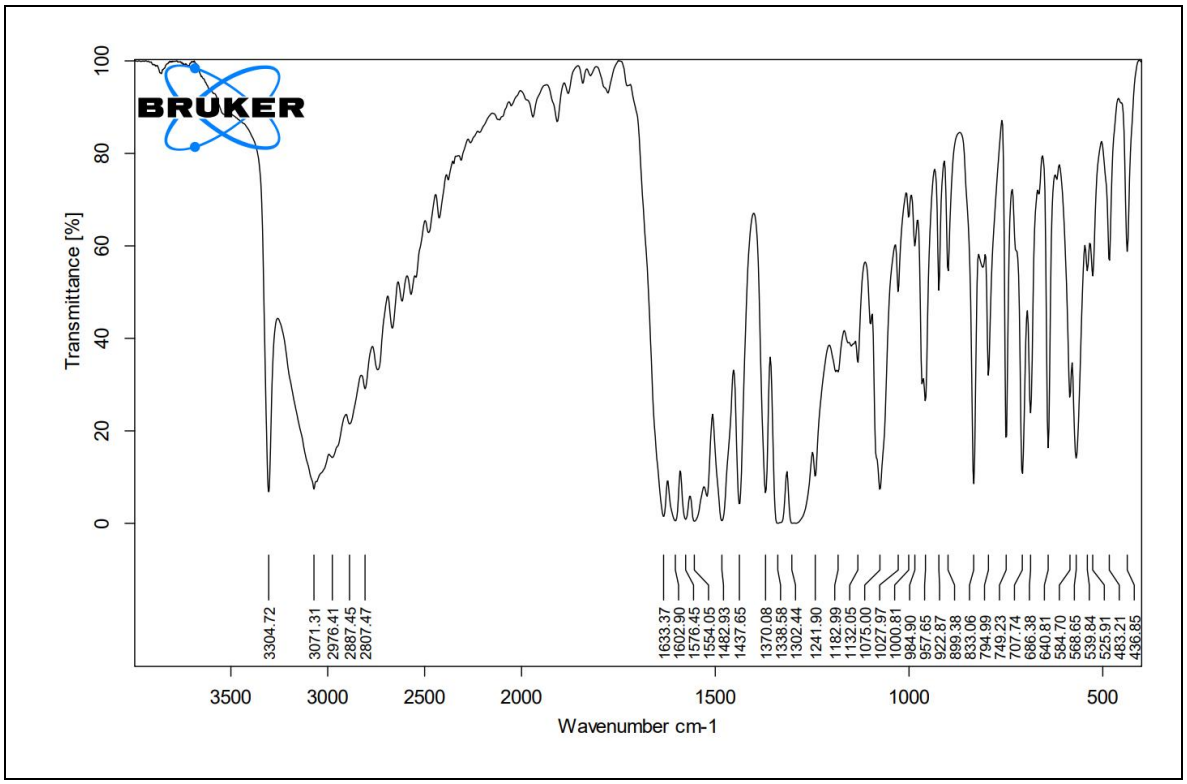

Fig. 11. FTIR spectrum of complex **8**.

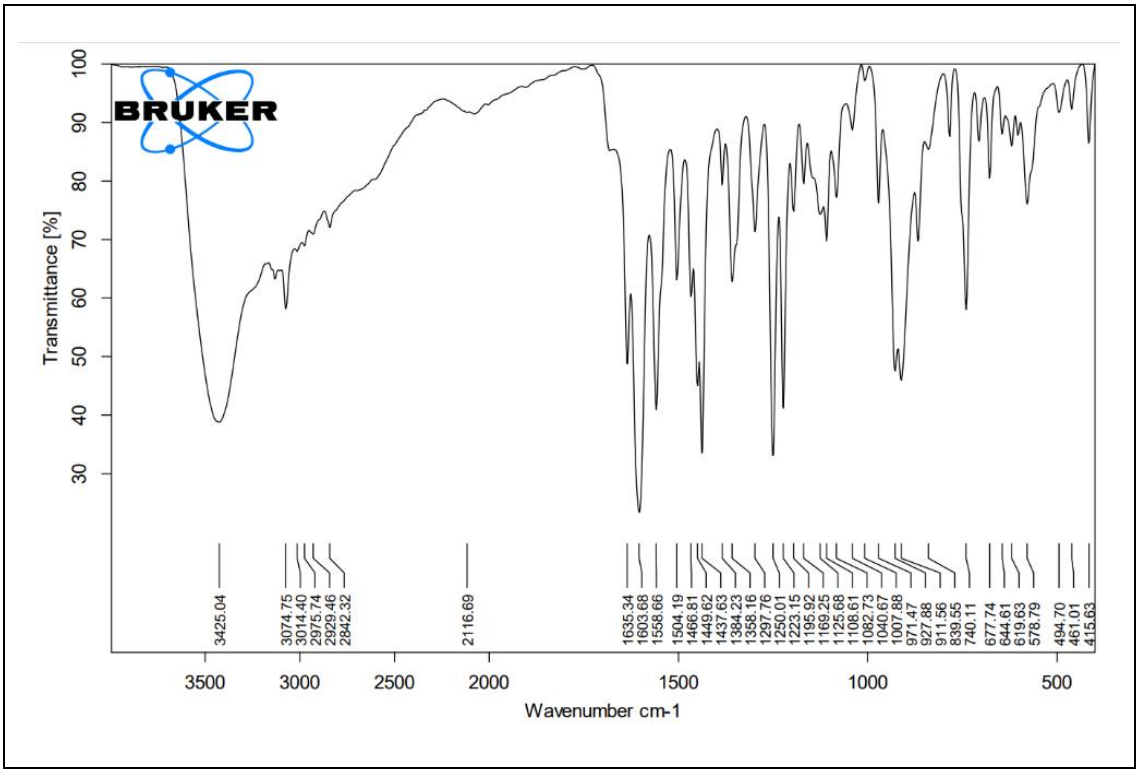

Fig. 12. FTIR spectrum of complex **9**.

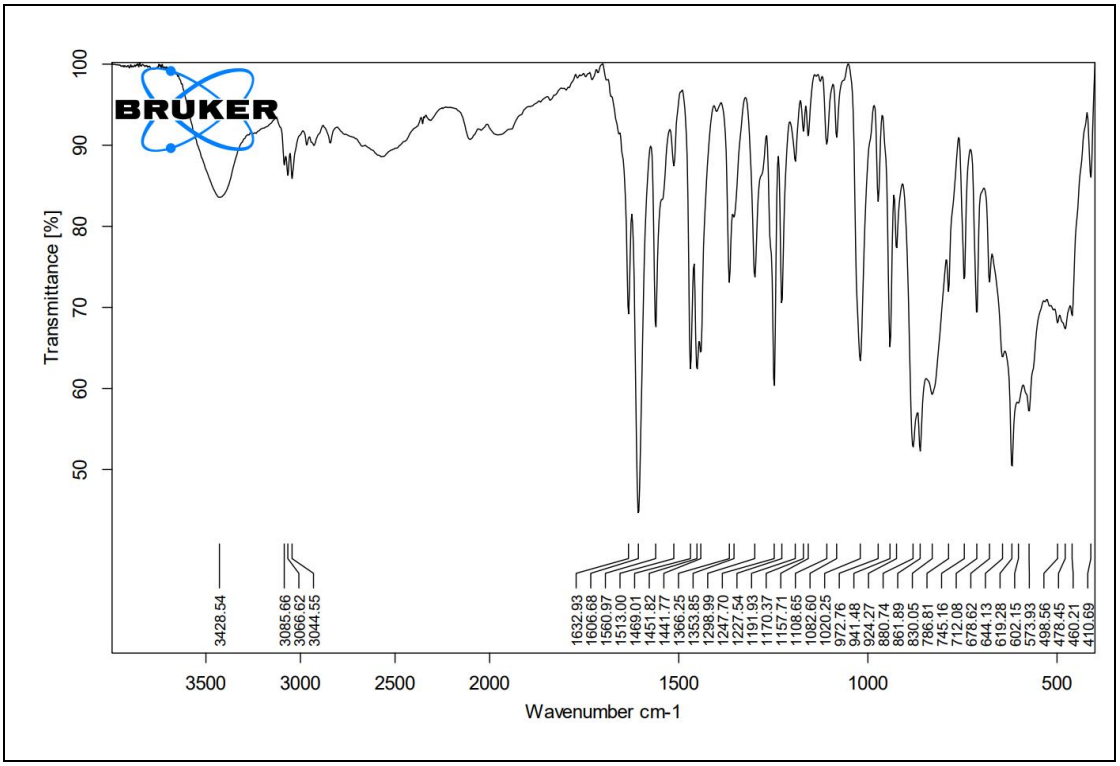

Fig. 13. FTIR spectrum of complex **10**.

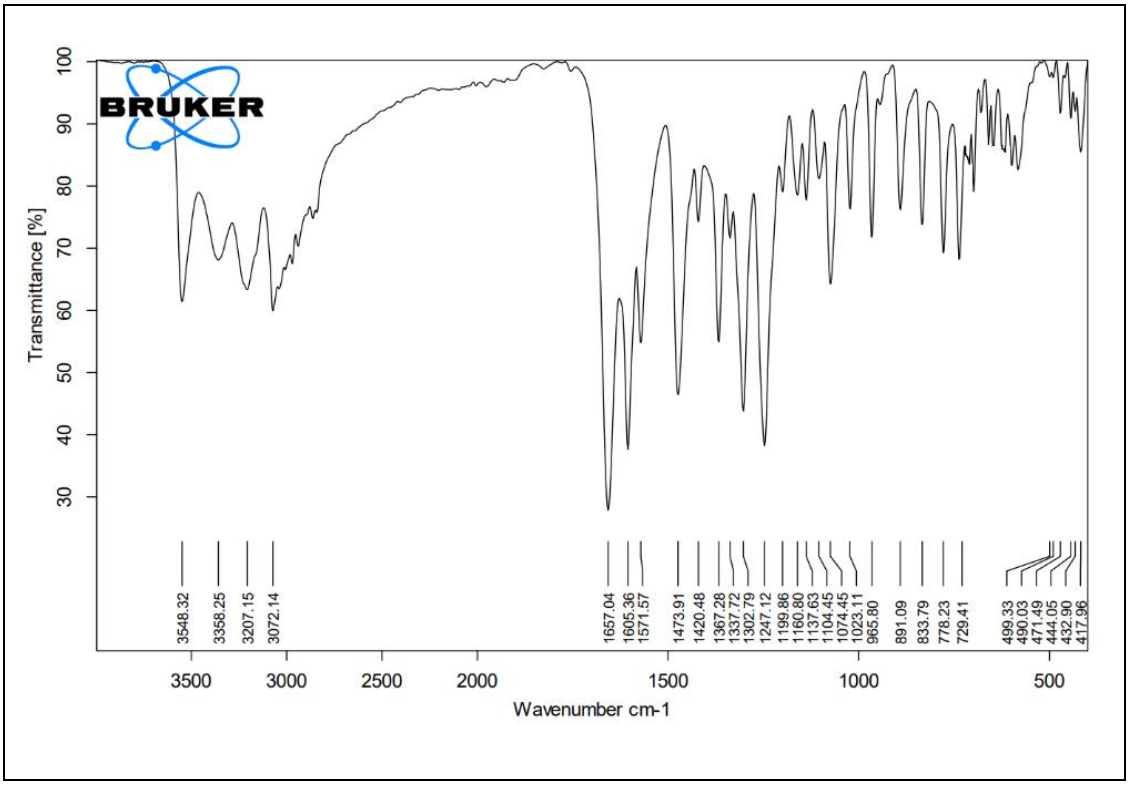

Fig. 14. FTIR spectrum of complex **11**.

3.4 ESI Mass Analysis

As single crystals of complexes, **1-11** could not obtain so an ESI mass of complexes was done to confirm the molecular weight of complexes. Positive mode ESI-mass of complexes were done. The ESI mass of complexes is almost similar to the calculated mass of the complexes. The mass of complexes was obtained in $[M + 1]^+$ and $[M + 2]^+$ mode. The mass of complexes is given in Fig. 15-25.

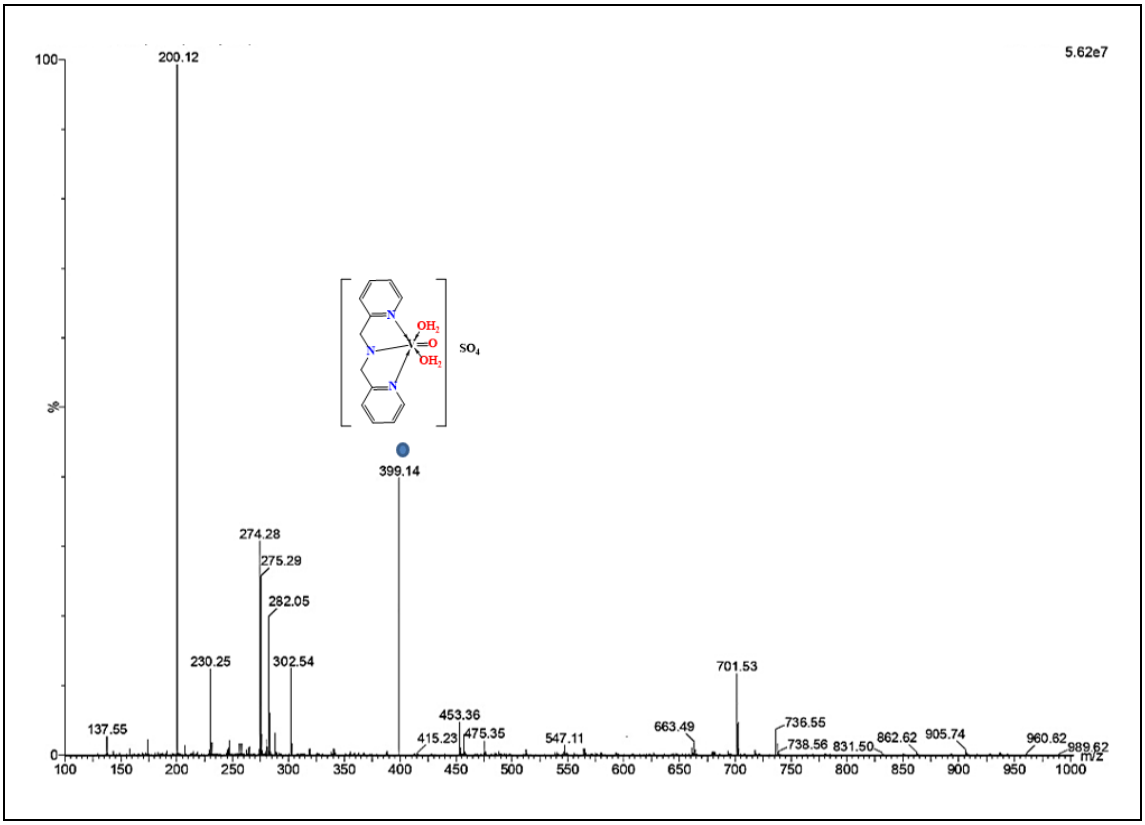

Fig. 15. ESI Mass spectrum of complex **1**.

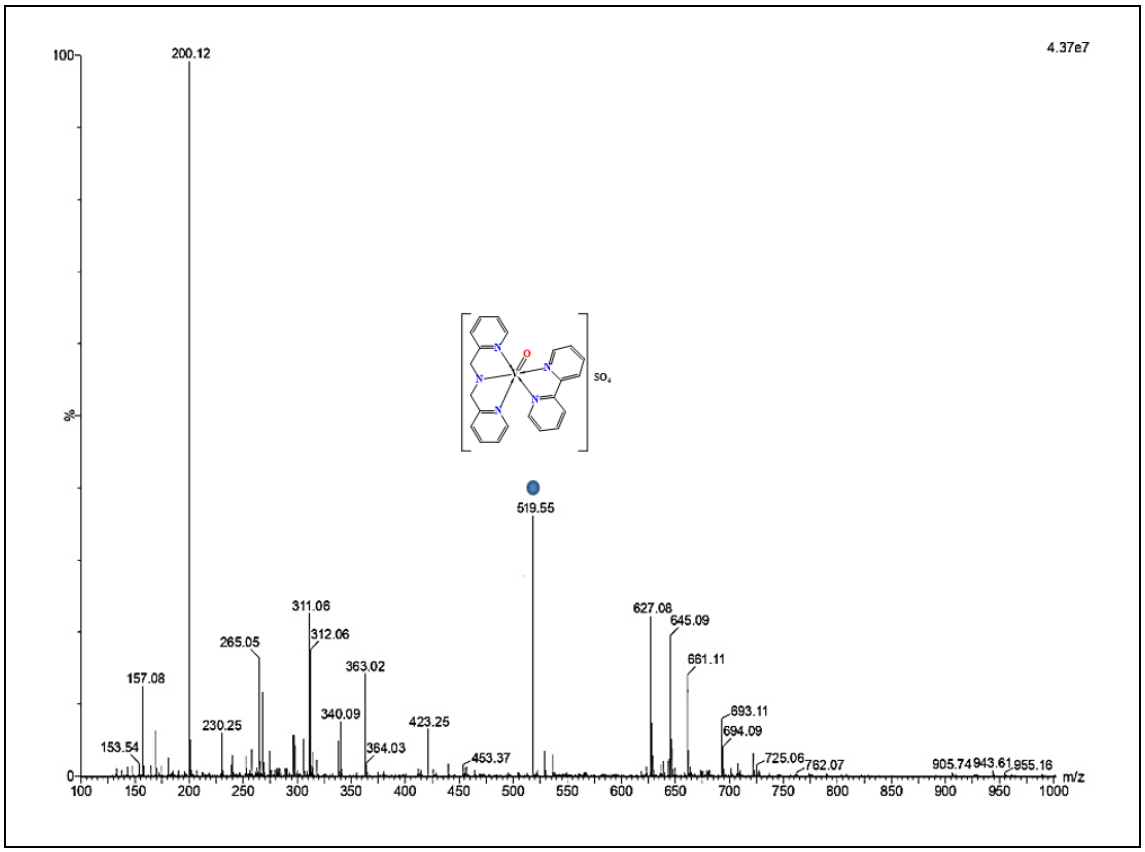

Fig. 16. ESI Mass spectrum of complex **2**.

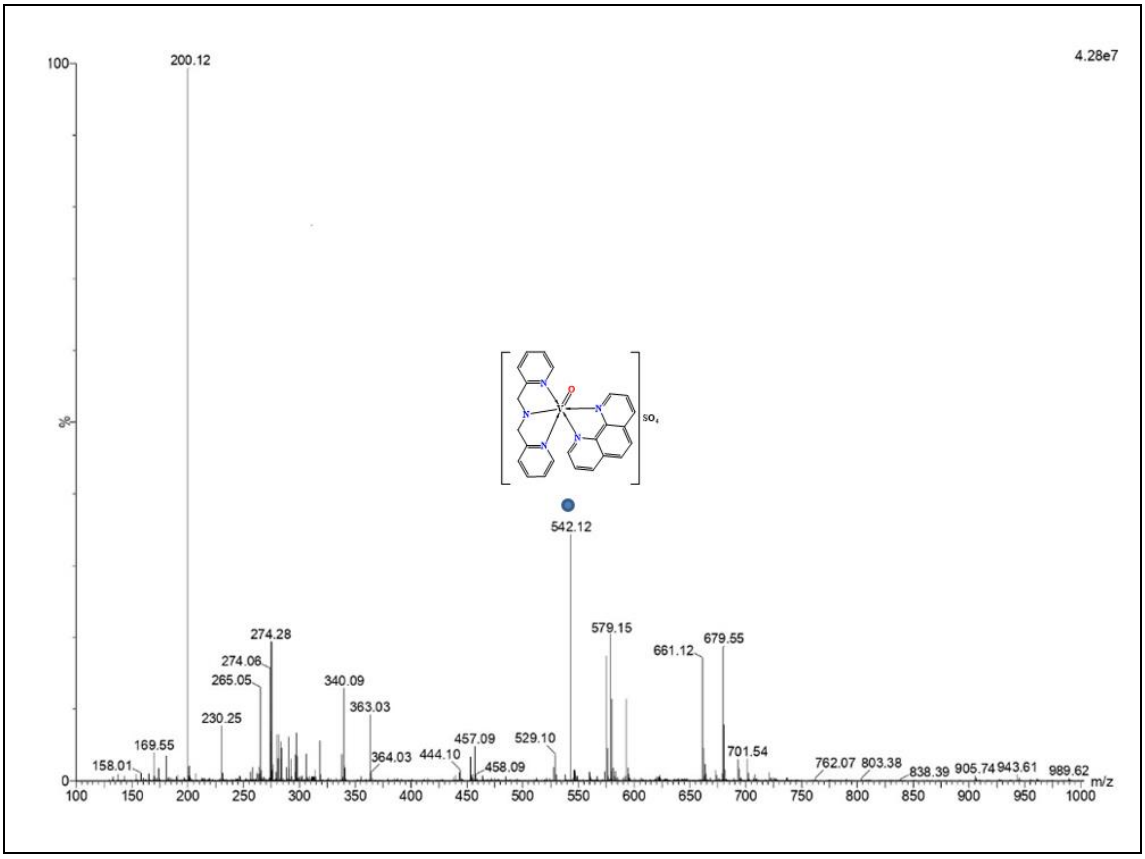

Fig. 17. ESI Mass spectrum of complex **3**.

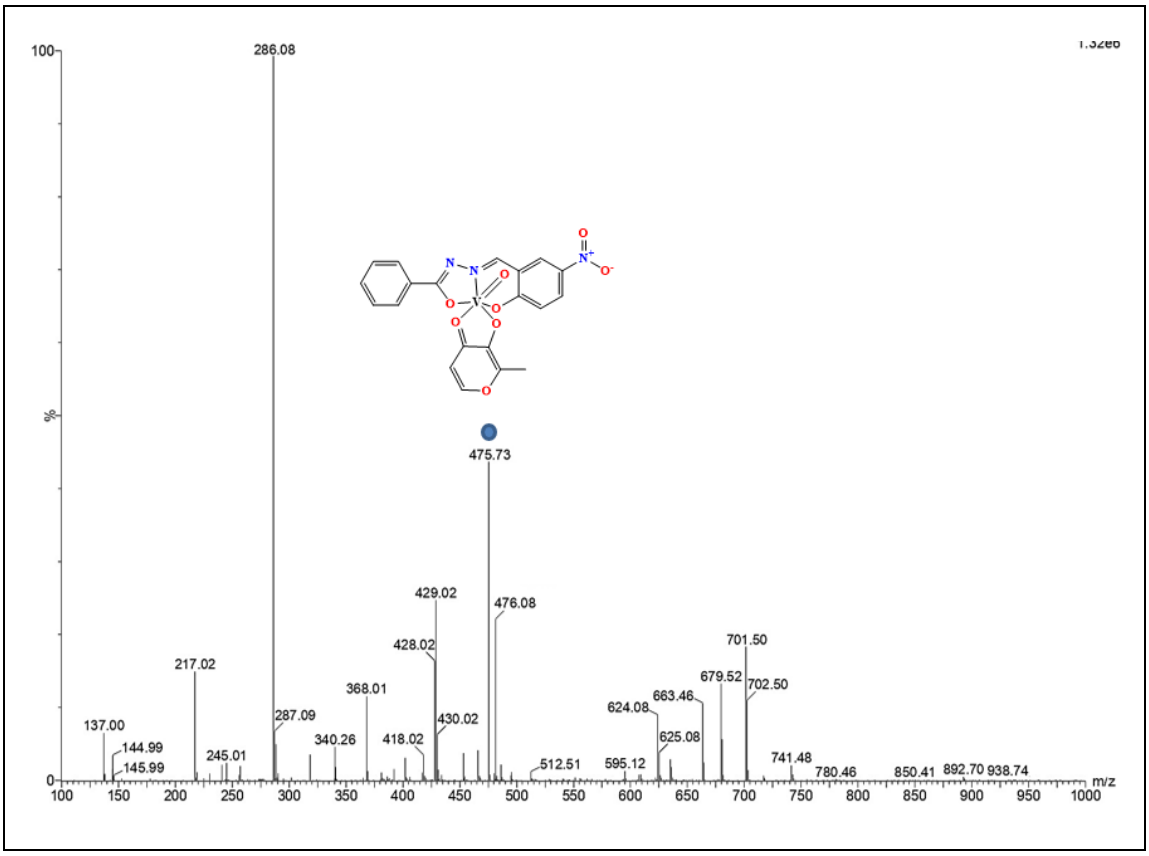

Fig. 18. ESI Mass spectrum of complex **4**.

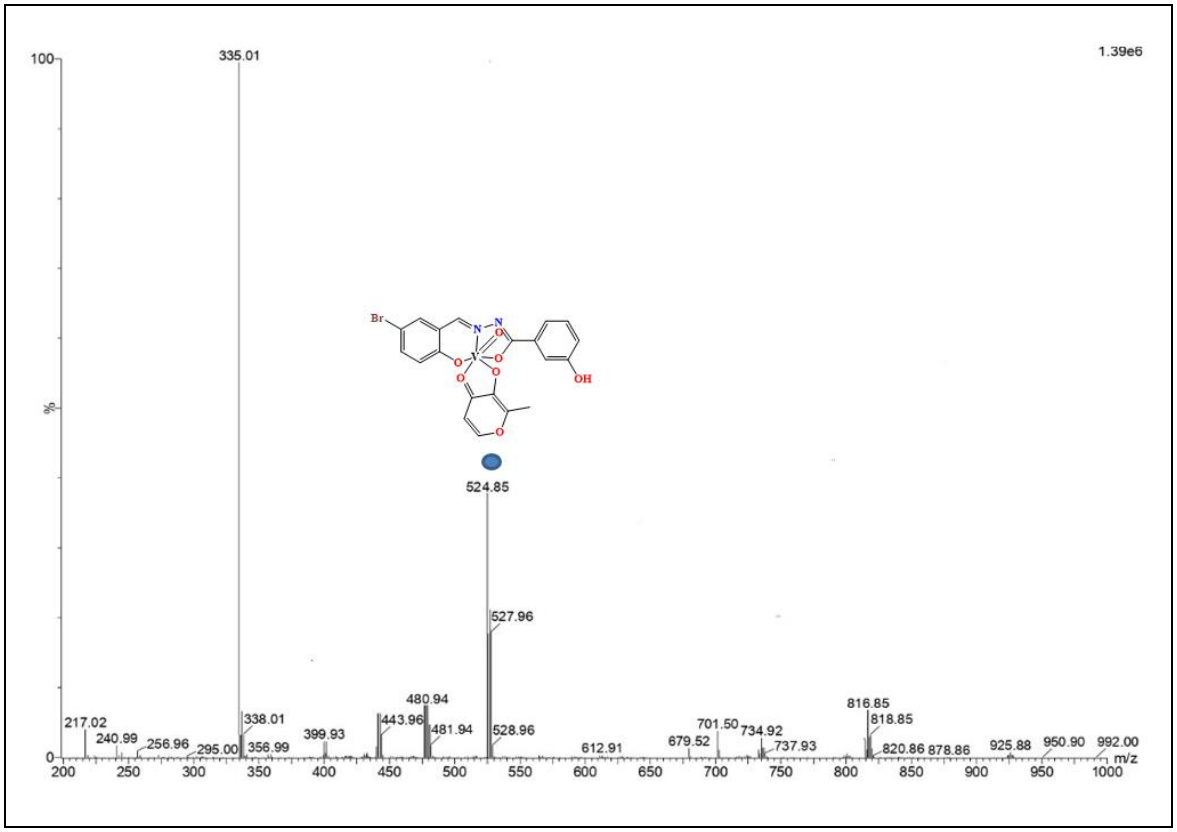

Fig. 19. ESI Mass spectrum of complex **5**.

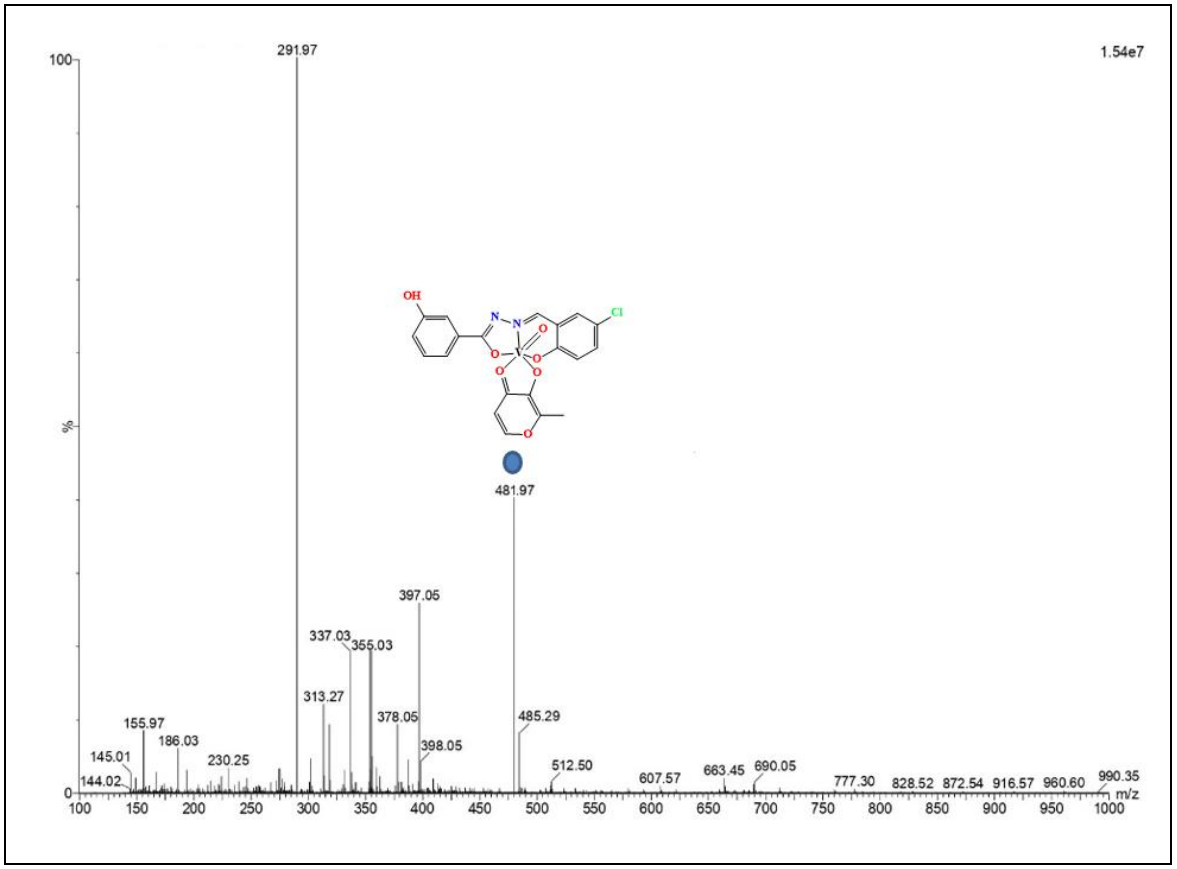

Fig. 20. ESI Mass spectrum of complex **6**.

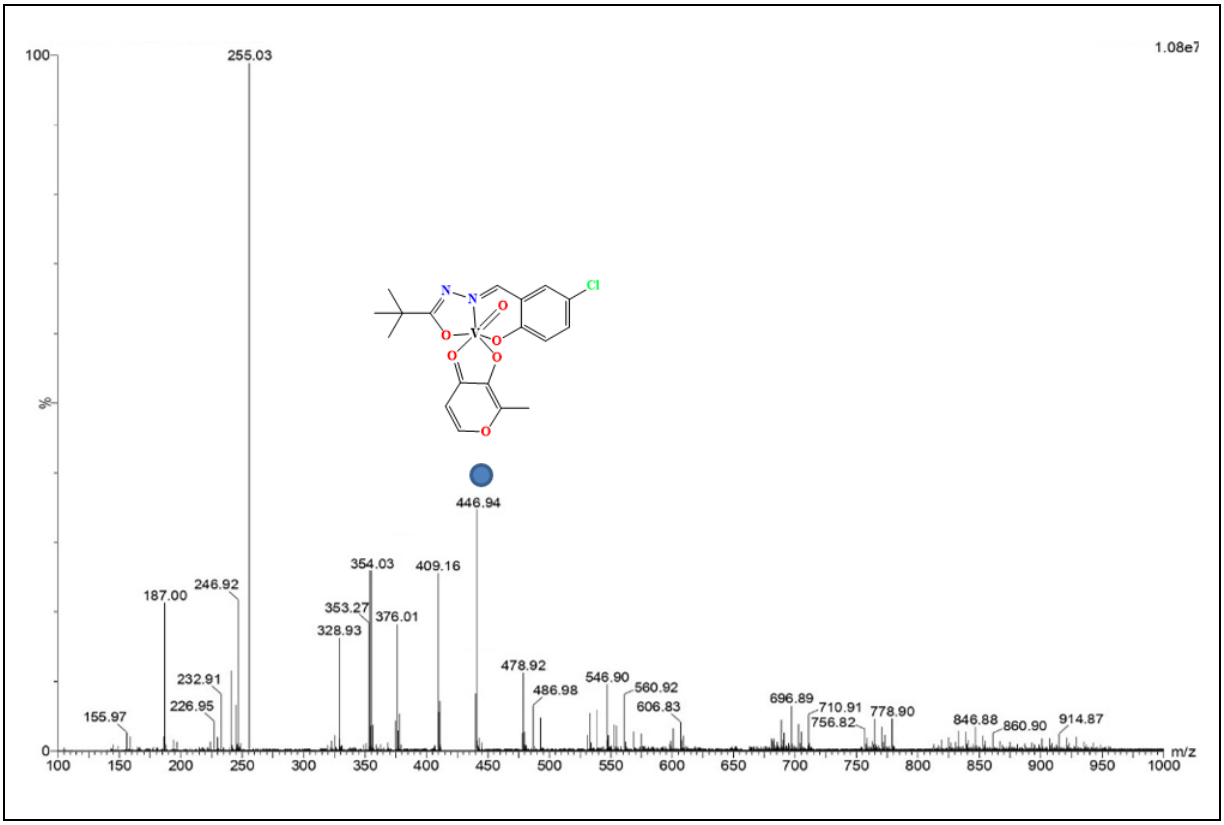

Fig. 21. ESI Mass spectrum of complex **7**.

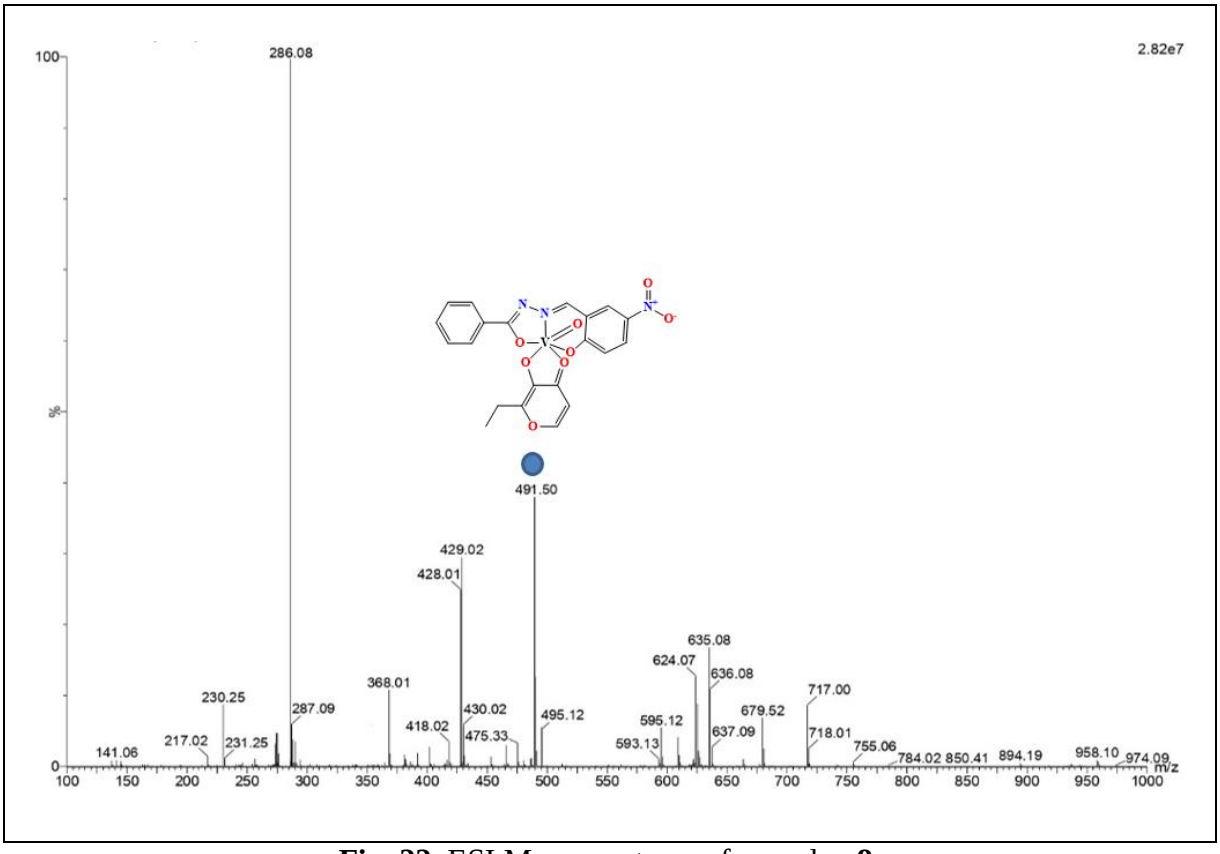

Fig. 22. ESI Mass spectrum of complex **8**.

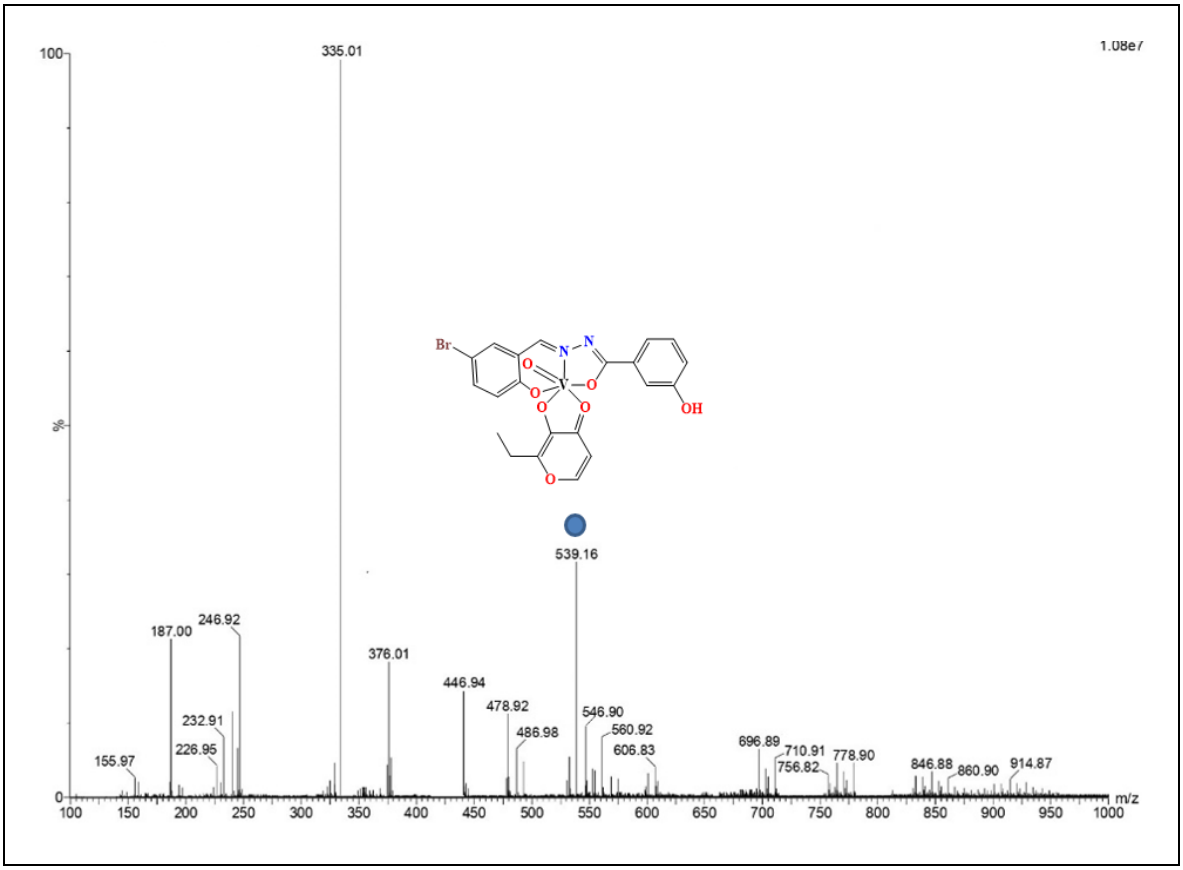

Fig. 23. ESI Mass spectrum of complex **9**.

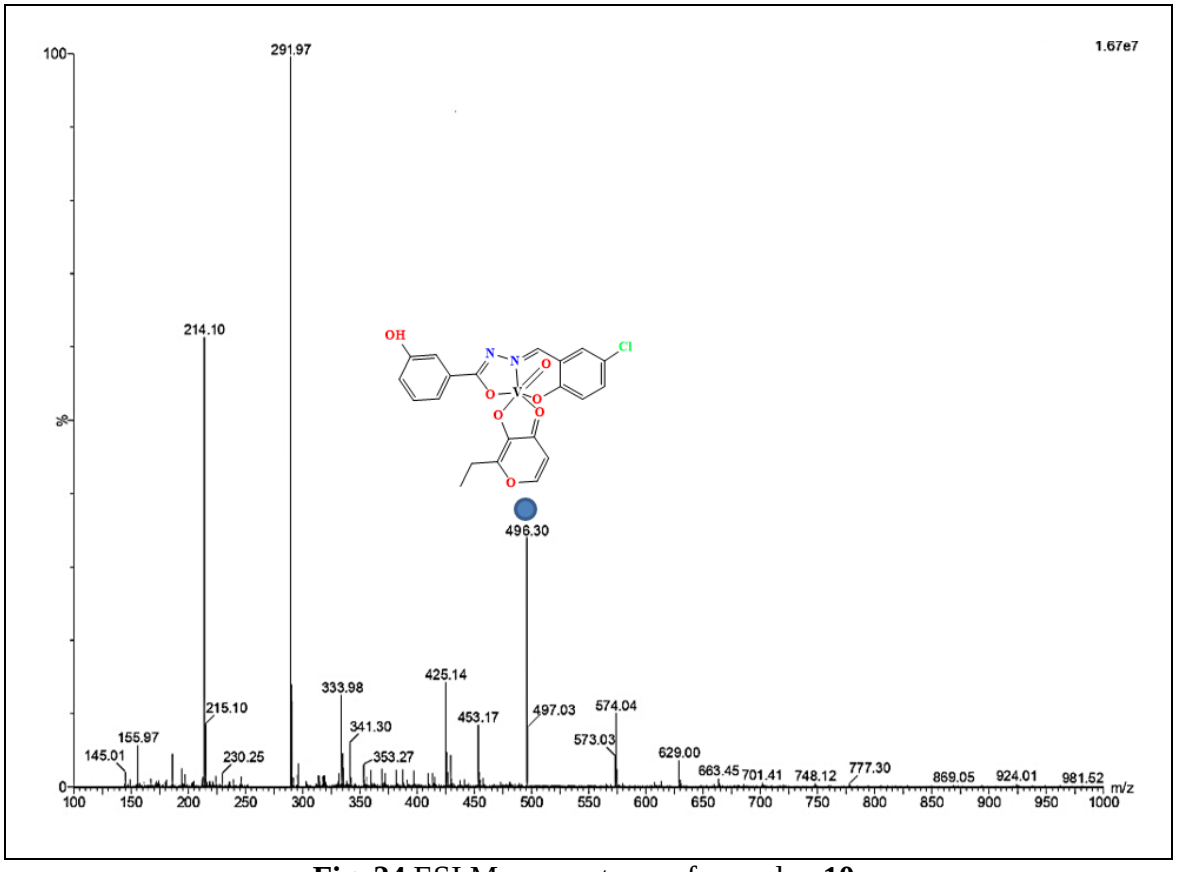

Fig. 24.ESI Mass spectrum of complex **10**.

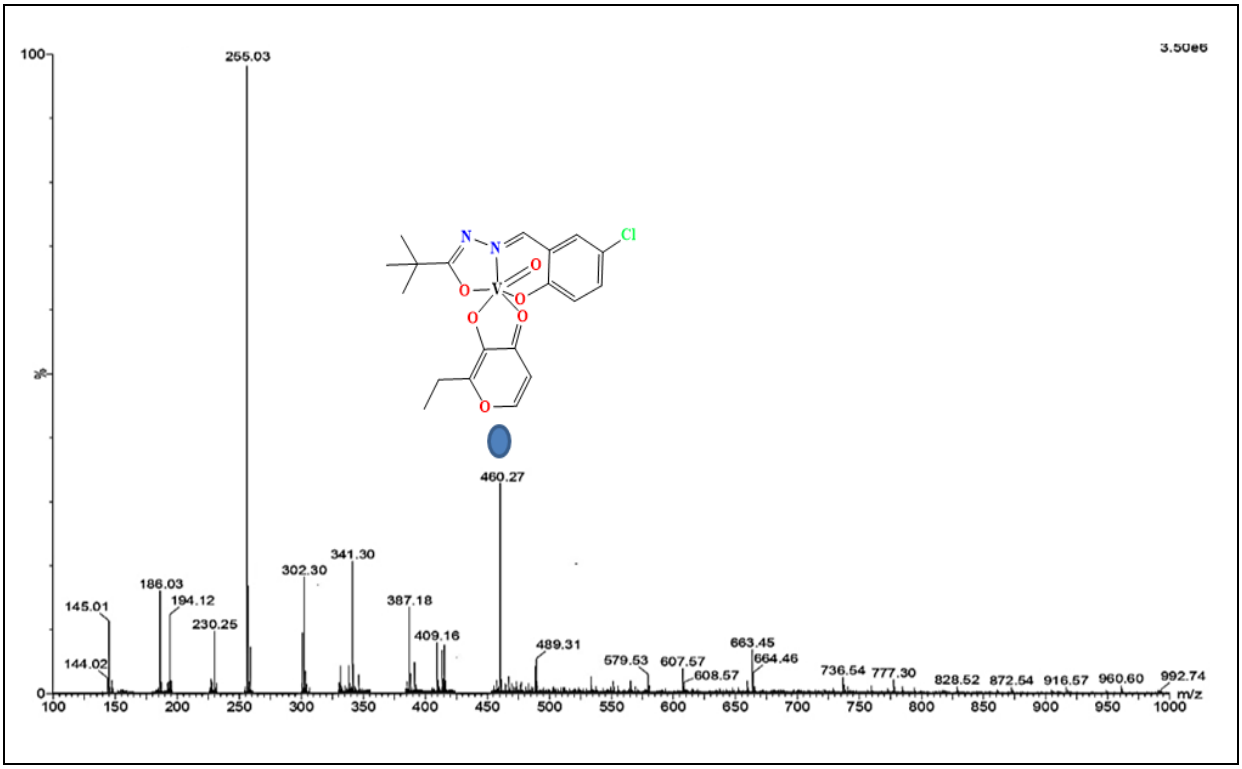

Fig. 25. ESI Mass spectrum of complex **11**.

3.5 Magnetic and EPR spectral properties

Magnetic susceptibility data of all complexes (**1-3**) were measured at room temperature. The complexes **1-3** exhibit magnetic moment 1.81, 1.79 and 1.83 BM respectively, in accord with a spin only value of vanadium complexes having VO^{2+} ion [48]. Vanadium(IV) complexes and are quite close to the value related to these complexes [49].

The full range (3200–2000 G) X-band EPR spectra for the oxidovanadium(IV) complexes (frozen liquid state and room temperature solid-state) were recorded. The ESR spectra of all the complexes show a typical eight-line pattern which suggests that single vanadium is present in the molecule, i.e., it is mononuclear. The g and A-values were computed from the spectra using TCNE free radical as g marker. EPR parameters were evaluated from RT and LNT spectra (Table 3). EPR spectra of all complexes in DMSO solution at RT yield light isotropic lines in which unpaired electron is coupled to the nuclear spin I = 7/2 of oxidovanadium(IV) nucleus [50]. The appearance of light isotropic ions consistent with the magnetic moments and reveal that the dissociation of the complex has not occurred during sample preparation. The values of room temperature EPR parameters (A_{iso}

and g_{iso}) confirm the presence of oxidovanadium(IV), $3d^1$ in a distorted octahedral geometry. The EPR spectra of the DMSO frozen solution were recorded at LNT (Fig. 26-28). These spectra are consistent with the existence of the $[VO]^{2+}$ state in an octahedral geometry [51-57]. The electronic and nuclear spin features are used to reveal the types of sites coordinated to a particular complexion. Additively relationship is used to predict the $A_{\parallel}$ of such complexes based on the contribution to $A_{\parallel}$ from each of four equatorial donor positions [56]. The calculations were done according to additively relationship [58]. This relationship gives a valid criterion to predict the donor atoms of such complexes.

Table 3 Spin Hamiltonian parameters of vanadyl complexes at room temperature and liquid nitrogen temperature in 3.0×10^{-3} M DMSO solution.

Complex	RT		LNT			
	g_{iso} (cm^{-1})	A_{iso} (x 10^{-4} cm^{-1})	g_z (x 10^{-4} cm^{-1})	g_x, g_y (x 10^{-4} cm^{-1})	A_z(x 10^{-4} cm^{-1})	A_x, A_y (x 10^{-4} cm^{-1})
1	1.978	95	1.937	2.009	166	67
2	1.967	93	1.940	2.007	167	67
3	1.982	95	1.937	2.008	157	70

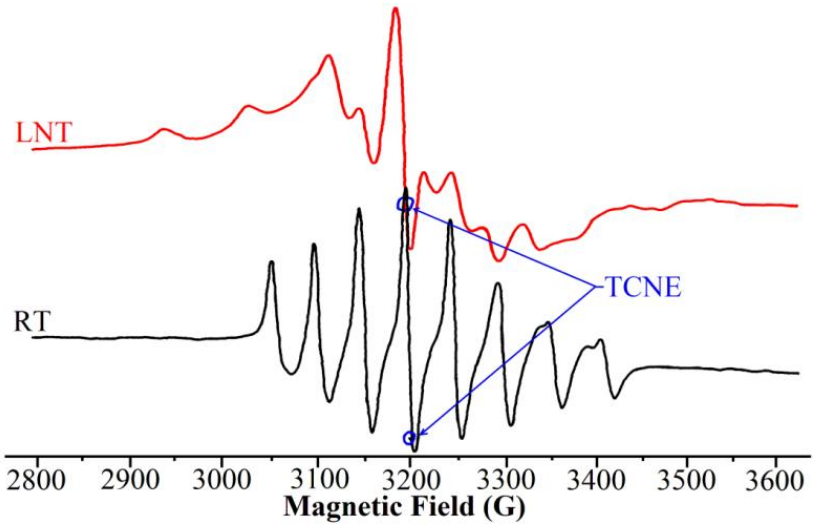

Fig. 26. X-band EPR spectra of complex **1** in polycrystalline state (RT) and DMSO solution at LNT.

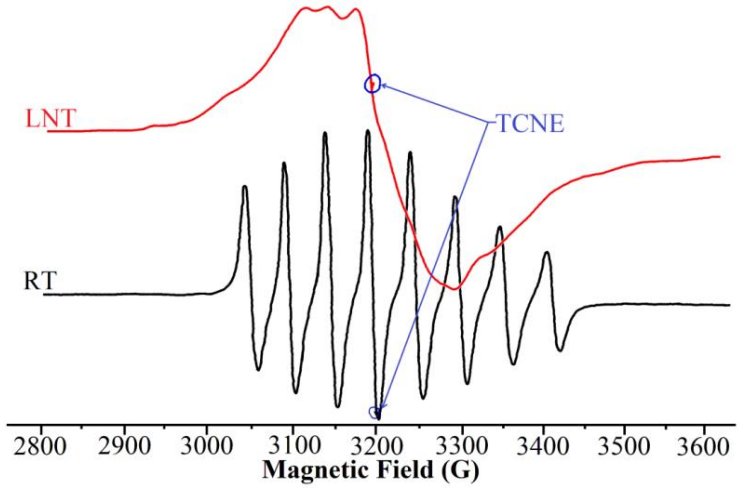

Fig. 27. X-band EPR spectra of complexes **2** in the polycrystalline state (RT) and DMSO solution at LNT.

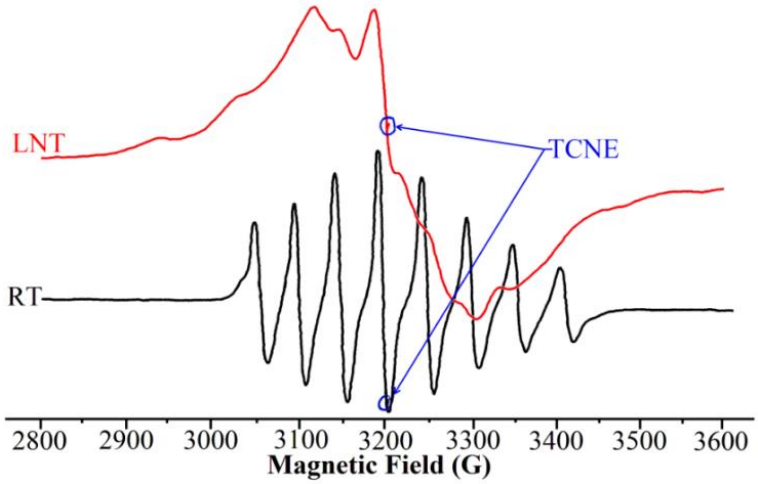

Fig. 28. X-band EPR spectra of complex **3** in the polycrystalline state (RT) and DMSO solution at LNT.

3.6 Electronic spectra

3.6.1 Electronic spectra of complexes 1-3

UV-visible spectra of all complexes were recorded in DMSO solution (3.0×10^{-3} M). The UV-vis spectrum of all complexes has similar spectral features. The oxidovanadium(IV) complexes **1-3** exhibit bands in the range 250-500 nm, among which the two high energy bands in the UV region are attributed to the ligand centered transitions π-π* and n-π* transitions. Also, a new band of medium intensity appears in the range 450-550 nm, which is assigned to the ligand to metal charge transfer band [59, 60] (Fig. 29) upon dissolution these

complexes tend to hydrolyse and oxidize. These bands at 750 nm are due to d-d transitions. Such bands observed in oxidovanadium(IV) octahedral complexes, [61] such electronic spectra reveal that in present complexes vanadium is present in V^{4+} state [62].

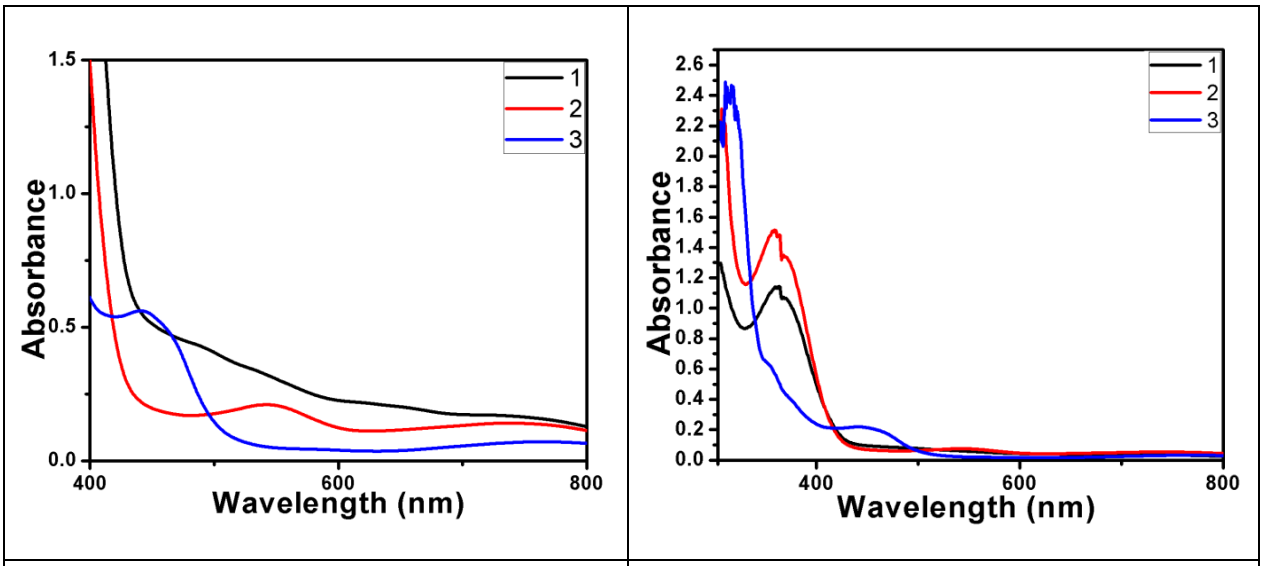

Fig. 29(a). Absorption spectra of the complexes **1-3** show low-intensity broadband in 6.0 × 10^{-5} M DMSO solution. **(b)** Display strong absorption bands in the high energy region of complexes **1–3** in 3.0 × 10^{-3} DMSO solution.

In the electronic spectra of complexes **4-11,** the bands in the range 300-375 nm are due to the intraligand π→π* absorption of the azomethine group [63]. The absorption bands of 400-425 nm are assignable to n→π* of carbonyl group [64]. In all complexes, an intense absorption band at 425-500 nm is assigned to the phenolic $N_{(p)}/O_{(p)}\rightarrow V_{(dx)}$ ligand to metal charge transfer (LMCT) band [65-66]. The d-d absorption bands were not observed in all complexes being d^{10} vanadium systems Fig. 30. The UV-Visible data of all complexes are given in Table 4.

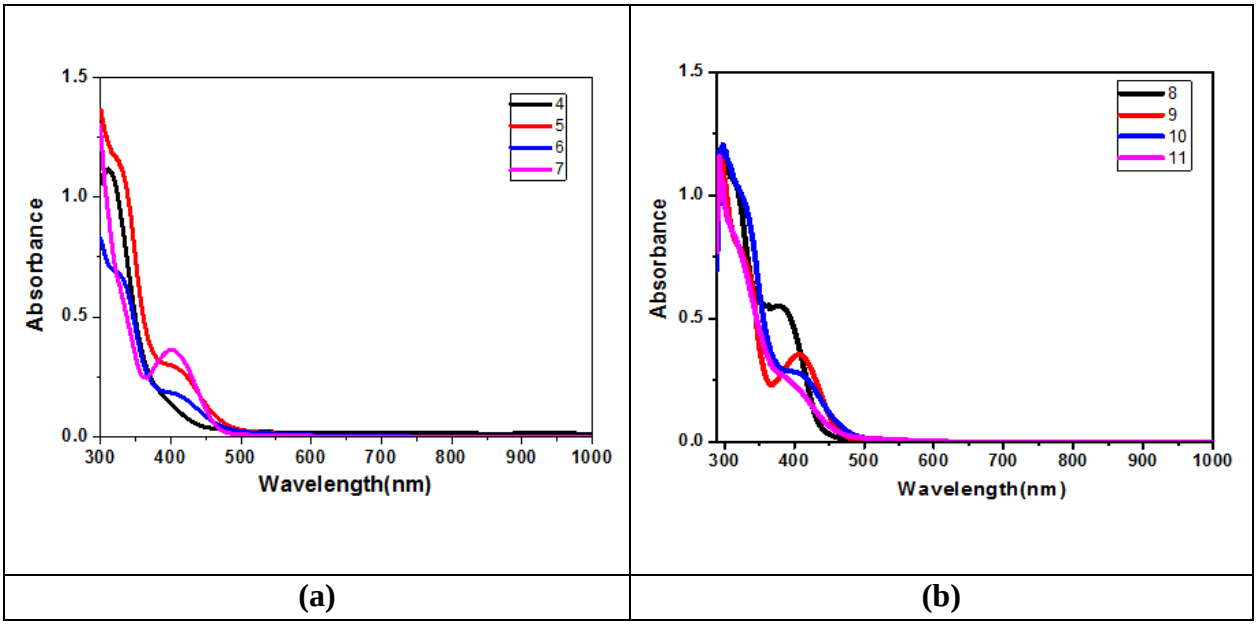

Fig. 30. Electronic spectra of complexes **4-11** in DMSO solution.

Table 4 Electronic spectral assignments (nm) of oxidovanadium(V) complexes.

Complex	π →π*	n→π*	LMCT
1	310	378	520
2	315	370	550
3	332	375	450
4	298	312	409
5	293	329	413
6	297	325	410
7	294	326	401
8	303	362	379
9	294	323	409
10	296	328	415
11	297	328	401

3.7 Electrochemical Study

3.7.1 Electrochemical Study of complexes 1-3

The electrochemical behaviours of complexes (**1-3**) have been initiated using cyclic voltammetry (CV) and differential pulse voltammetry (DPV) in DMSO in the presence of 0.1

M TBAP solution. The cyclic voltammogram of **1-3** reveals a similar pattern. Only a single reduction wave at ~0.7 V is observed due to the V(IV)/V(III). The corresponding reduction wave is not observed [67]. A similar observation was made by the DPV experiments. At more negative potential i.e., at ~0.7 V is due to V(IV)→V(III) electrode reaction (Fig. 31). An additional cathodic wave at less negative potential was observed in each ion due to the reduction of ligand moiety.

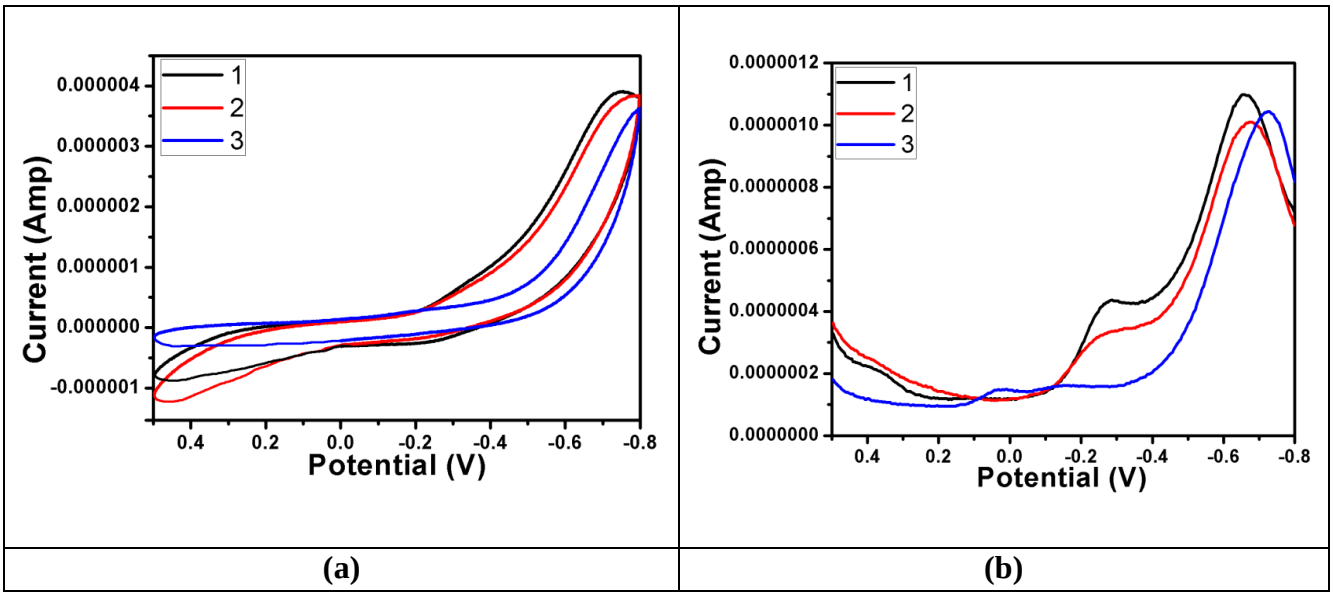

(a) **(b)**

Fig. 31 (a) Cyclic voltammograms of complexes **1–3** in DMSO at an Ag/AgCl electrode with a scan rate of 300 mV s^{-1} and temperature 20 °C. **(b)** Differential pulse voltammogram of complexes 1–3 at room temperature using a scan rate of 20 mV s^{-1} in DMSO. The pulse amplitude is 50 mV.

3.7.2 Electrochemical studies of complexes 4-11

The electrochemical properties of complexes **4-11** were also studied at room temperature by cyclic voltammetry (CV) and differential pulse voltammetry (DPV) in DMSO containing 0.1 M tetrabutylammonium perchlorate (TBAP) as a supporting electrolyte. The reduction potential data are summarized in Table 5. The cathodic peak potentials at -(0.6271-0.7085 V) Fig. 32. The reduction process exhibits one-electron transfer i.e. the reduction of vanadium(V) to vanadium(IV) [68]. In complexes **4** and **7** one cathodic peak is due to the reduction of ligand moiety [49]. Such reduction processes were verified by differential pulse voltammetric experiments Fig. 33. The reduction potential at - (0.753- 0.8175 V) can be the one-electron reduction process from vanadium (V) to vanadium (IV). The CV of all

complexes is without any response. Although, the less defined peak observed in DPV at positive potential is due to the reduction of ligand moiety.

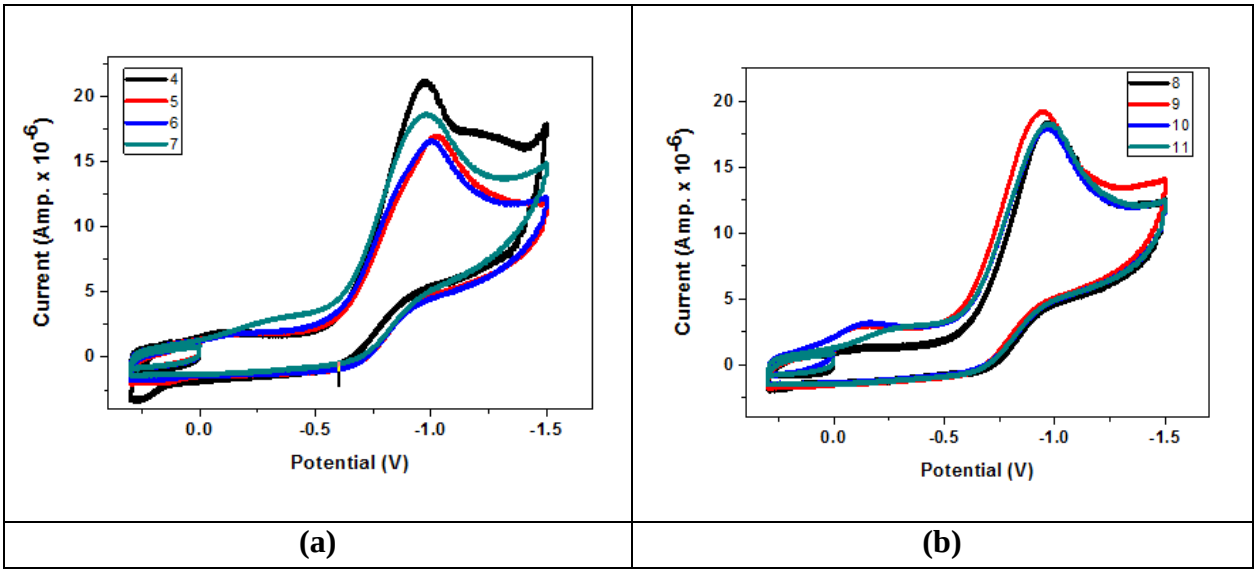

Fig. 32. Cyclic voltammograms of complexes **4-11** in DMSO (1.0×10^{-3}M) at an Ag/AgCl electrode at a scan rate of 300 mVs^{-1} and temperature of 20 ˚C.

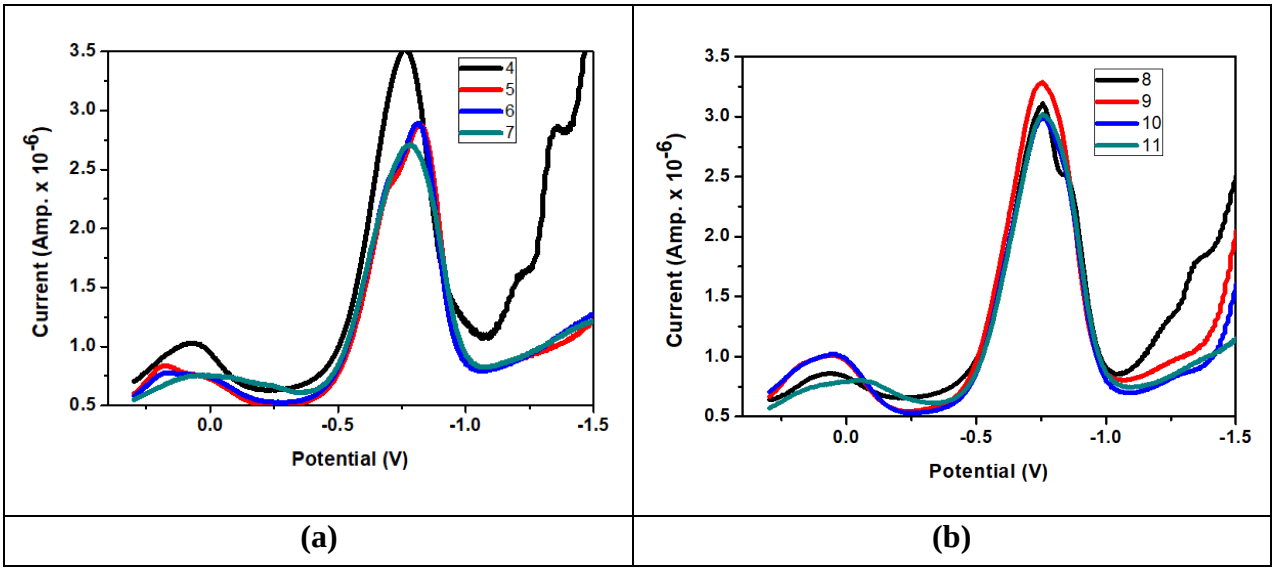

Fig. 33. Differential pulse voltammograms of complexes **4-7** at 20 ˚C in DMSO (1.0×10^{-3}M) solution (pulse amplitude = 50 mV).

Table 5 Electrochemical data of complexes at RT in DMSO.

Complex	E_{pc}(V)	E_{pa}(V)	$E_{(dpv)}$(V)
4	-0.975, -1.193	-0.676, -1.147	
5	-1.019	-0.677	+0.104, -0.801
6	-1.004	-0.658	+0.070, -0.817
7	-0.980	-0.695	+0.053, -0.779
8	-0.972	-0.708	+0.066, -0.757
9	-0.945	-0.527	
10	-0.971, -0.147	-0.634	+0.044, -0.753
11	-0.972	-0.650	+0.001, -0.757

3.8 Thermogravimetric Analysis (TGA)

The synthesized oxidovanadium complexes **1**-**3** were found to be air-stable and have higher thermal stability. The thermal study was carried out using the thermogravimetric technique with a heating rate of 10 °C min^{-1}. TGA graphs of complexes are shown in Fig. 34. All complexes show a two-step decomposition pattern. The decomposition pattern is shown in Scheme 4. The experimental results revealed that degradation occurred in two stages. In complex **1** up to 300 °C no mass loss is observed but after 300 °C there is mass loss about 2.9 % due to moisture or water content in the complex. The complex slowly started to decompose within the range of 300-400 °C, weight loss about 45.3 % which corresponds to the loss of 2,2'-bis(pyridylmethyl)amine molecules leaving behind the final product of the thermal decomposition. Whereas in complex **2** and **3** degradation start at 300-400 °C (33.5 % in **2** and 37.3 % in **3**) is due to pyrolysis of the molecule 2,2'-bis(pyridylmethyl)amine is observed. In the temperature range, 450-600 °C the mass loss is due to the pyrolysis of another ligand that is 2,2-bipyridyl for complex **2** about 12.2 % and 1,10-phenanthroline for complex **3** about 17.2 % leaving behind the final product V_2O_5.

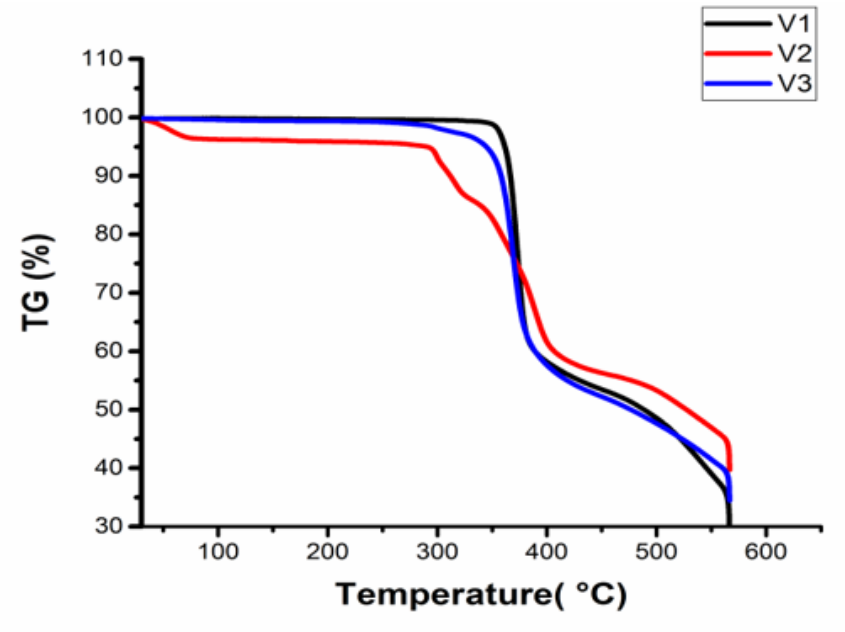

Fig. 34. TGA curves of complexes **1-3** recorded in the temperature range of 25-600 °C with a nitrogen atmosphere.

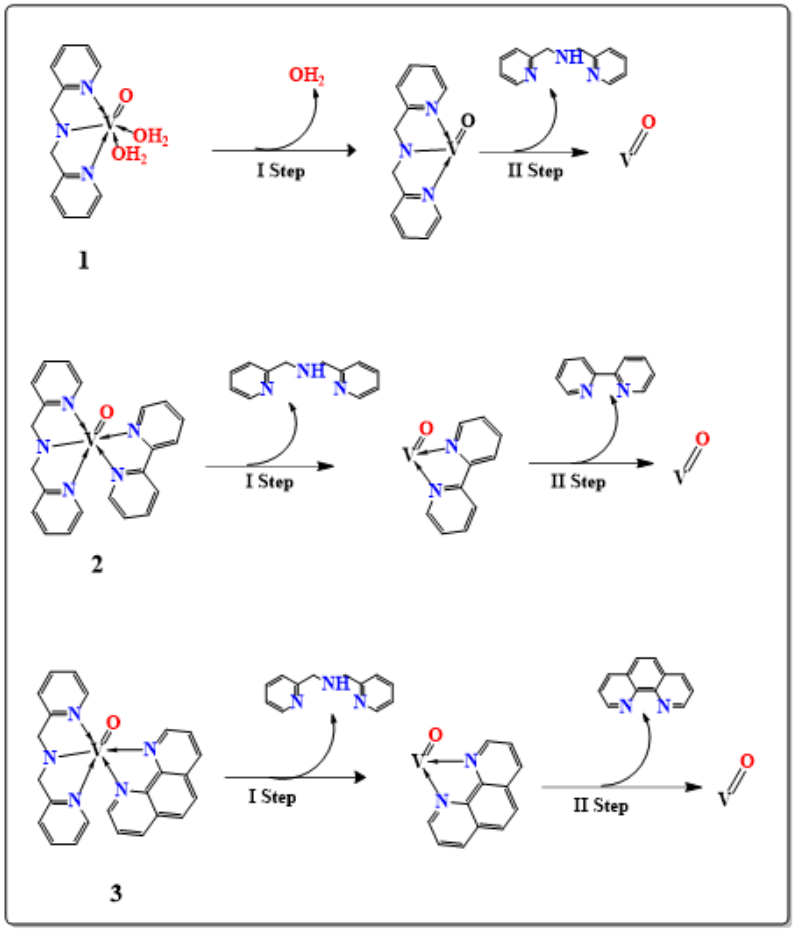

Scheme 4 TGA Decomposition pattern of complexes **1-3**.

3.9 Antidiabetic activity

3.9.1 α-Glucosidase inhibition activity

The pharmacologically active state of vanadium was evaluated concerning the interaction of vanadium ions and isolated rat intestinal acetone power. From these experimental results, the vanadyl state is proposed to be an active form of vanadium in enhancing insulin action by interacting with glucose carriers [69]. It is found that the oxidovanadium complexes enhancing glucose utilization in a concentration-dependent manner over the concentration range of 100 µg/mL to 900 µg/mL. The maximum response can be compared with % inhibition of α-amylase induced by present complexes (**1-3**). Complex **3** showed the lowest IC_{50} (Table 6). Therefore, complex **3** seems efficient and potent compared to other complexes. Complexes **1** and **2** also showed good antidiabetic mimetic activity. Therefore, here we conclude that all complexes showed good α-glucosidase inhibition and showed concentration-dependent activities Table 6. The observed data showed the lowest IC_{50} value in **3** (288.785±5.444), while the highest IC_{50} was found in **2** (1300.01 ± 7.513) and moderately in **1** (505.019 ± 130.0) are showing α-glucosidase inhibition in different concentration. The IC_{50} values for α-glucosidase inhibition activity were ranged from 100-900 µg/mL. Complex **3** seems potent among all the complexes with IC_{50} value 288.785 µg/mL while **2** was the cheapest inhibitor with IC_{50} value 1300.01 µg/mL Fig. 35. These observations are similar to the results of reported similar oxidovanadium(IV) complexes [70].

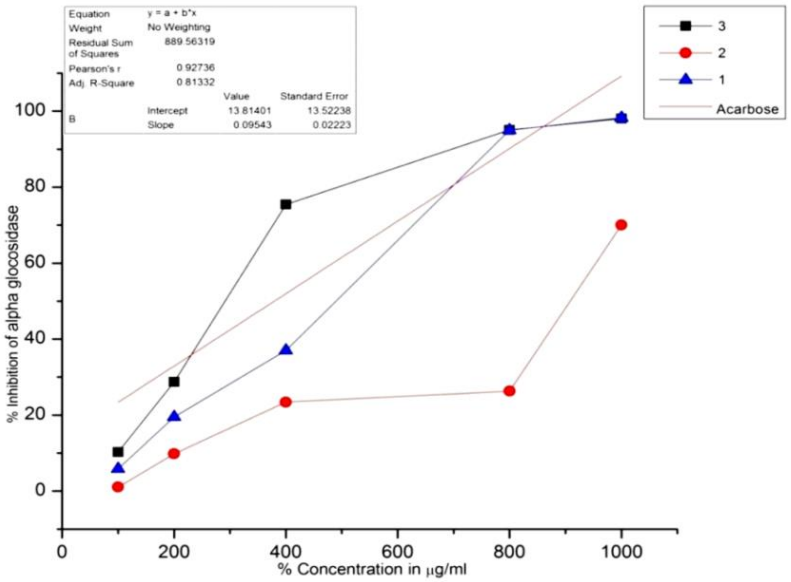

Fig. 35. α-Glucosidase inhibition of complexes **1-3**.

3.9.2 α-Amylase inhibition activity

The insulin-mimetic activity of the complexes was also estimated using the α-amylase inhibition method *in vitro*. The inhibition data exhibit that the oxidovanadium(IV) complexes stimulated glucose utilization in a concentration range of 100-900 µg/mL. The IC_{50} values for the α-amylase graph are shown in Fig. 36. The observed trend of α-amylase inhibition shown by complexes is as: **3** > **1** > **2**. From these observations, we conclude that these low molecular weight oxidovanadium(IV) complexes may be a promising candidate as antidiabetic agents. These resuts were similar to those reported by the previous workers [42].

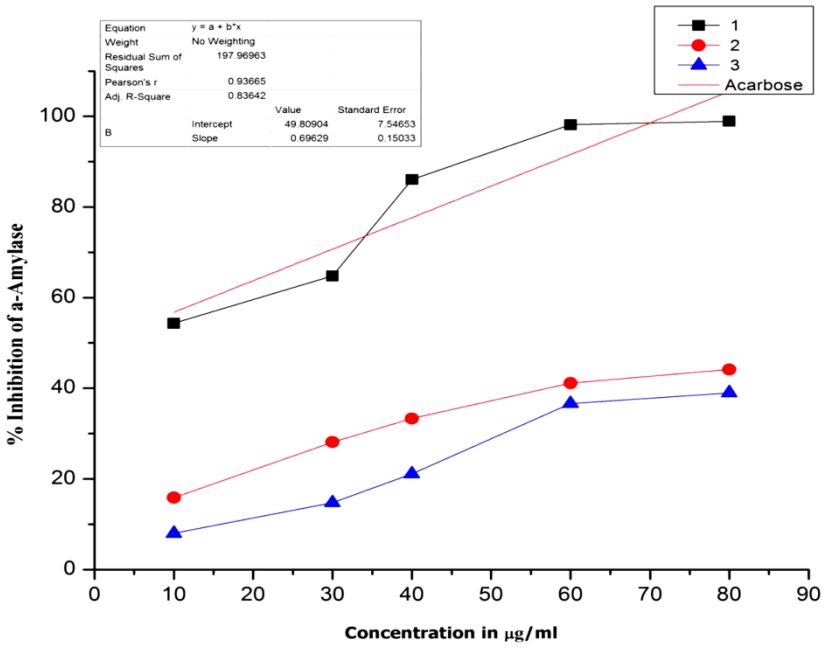

Fig. 36. α-Amylase inhibition of complexes **1-3.**

Table 6 Percent inhibition of α-glucosidase and α-amylase.

Concentration µg/mL	1	2	3
α-Glucosidase			
100	5.88	1.06	10.30
200	19.48	9.82	28.74
400	37.10	23.43	75.48
800	95.00	26.32	95.09
1000	98.22	70.08	98.04

α-Amylase			
10	7.97	15.87	54.35
30	14.71	28.12	64.76
40	21.13	33.33	86.03
60	36.62	41.15	98.17
80	38.97	44.15	98.92
100	45.07	55.91	99.61

3.9.3 α-Glucosidase inhibition activity

The α-glucosidase inhibition activity of complexes **4**-**7** was determined using α-glucosidase inhibition assay method [70]. The IC_{50} value for present complexes was evaluated from the percentage inhibition *vs.* concentration plot (Fig. 37) The IC_{50} values of complexes are shown in Table 7. In the same Table α-glucosidase activity is also listed. The observed trend in α-glucosidase activity is: **4** > **6** > **7** > **5**. Complex **4** showed the highest α-glucosidase activity and **5** showed the lowest activity. The observed trend inactivity is similar to the energy gap trend of these complexes. For complex **4** the energy gap is (ΔE) minimum and for **5** is maximum. The ΔE is also associated with the global softness (S). The value of S is highest for **4** and lowest for **5**. Therefore, these observations of crucial electronic parameters supported the trend of α-glucosidase reactivity. These complexes bind theα-glucosidase enzymes in the active or allosteric site through the vacant coordination site of vanadium(V)center in complexes. After binding, the establishment of H-bonding and hydrophobic interactions establish the inhibitor cooperatively [71]. Then mode of inhibition was checked for complex with the best IC_{50}.

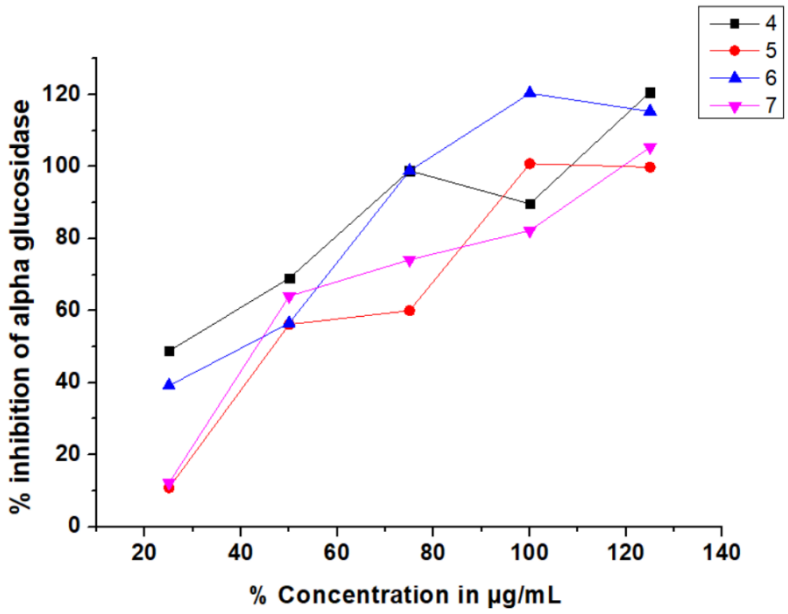

Fig. 37. α-Glucosidase inhibitory activity of complexes **4-7**.

Table 7 Antidiabetic parameters of complexes **4-7**.

Complex	IC_{50} (µg/mL)	α-glucosidase activity ($µg^{-1}$)
4	25.78	38.79
5	46.86	21.34
6	40.18	24.89
7	43.63	22.92

3.9.4 α-Amylase inhibition activity

The percentage of α-amylase enzyme activity of complexes 4-7 was screened by the reported α-amylase inhibition assay method [72]. The percentage inhibition *vs.* concentration is shown in Fig. 38. From this plot IC_{50} value was determined and presented in Table 8. In the same table value of α-amylase inhibition activity parameters is also listed in Table 8. The found trend in α-amylase of present complexes is similar to that of α-glucosidase inhibition activity. This trend is parallel to the trend of global reactivity parameters. Complex **4**is the global highest soft less hard molecule that showed the α-amylase activity. All complexes showed good α-amylase activity. The square pyramidal geometry of present complexes may bind near the active sites through hydrogen bonds or other hydrophobic interactions. Consequently, block the access to the active site of the enzyme is no longer active for hydrolysis of the starch molecule.

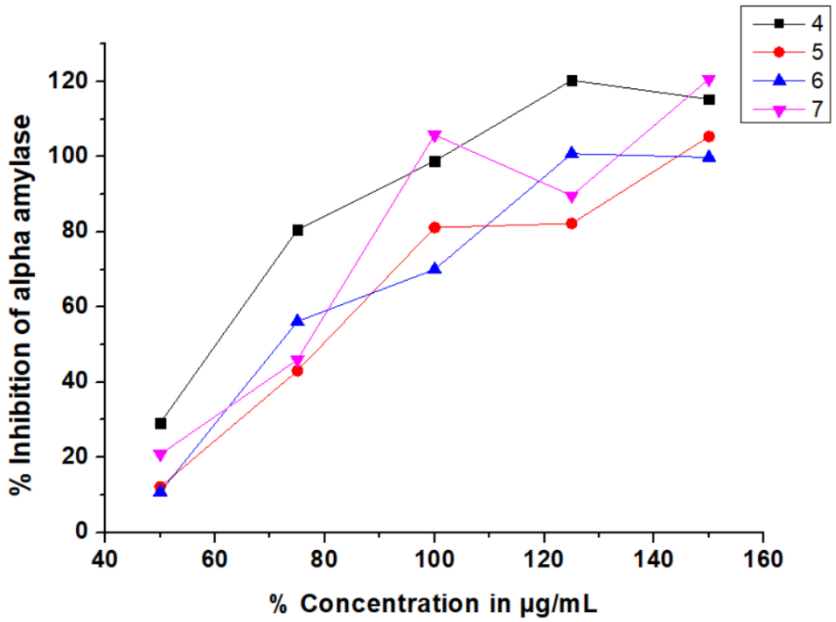

Fig.38. α-Amylase inhibitory activity of complexes **4-7**.

Table 8 Antidiabetic parameters of complexes **4-7**.

Complex	IC_{50} (µg/mL)	α-amylase activity ($µg^{-1}$)
4	60.01	16.66
5	80.40	12.44
6	71.97	13.89
7	76.66	13.04

3.9.5 α-Glucosidase inhibition activity

The α-glucosidase activity of complexes **8-11** was evaluated by using pNPG as substrate. The % inhibition *vs.* concentration plot is shown in Fig. 39. The antidiabetic activity parameters are listed in Table 9. The major constituently of carbohydrates in biological systems are glucose, fructose, maltose and sucrose. The water-soluble constituents can be easily absorbed into the blood stream from the gastrointestinal tract. The role of α-glucosidase is to transform te polysaccharides into Monosaccharides. Hence, diabetes and obesity can be controlled by inhibiting the enzyme activity of α-glucosidase to slow the absorption of these carbohydrates from our diet. The trend of α-glucosidase inhibition activity is **11** > **10** > **8** > **9**. This observed trend is similar to the trend of global reactivity parameters. Complex **11** showed higher global softness (S) and minimum energy gap ΔE in FMO.

Therefore, showed the highest activity. Whereas, complex **9** having the highest global hardness exhibited lowest α-glucosidase inhibition activity. This result of α-glucosidase inhibition activity might because hydrogen bond can be established in the amino or carboxylic moiety of bound α-glucosidase through a vacant active site in the complex. These results are consistent with the previous finding on similar vanadium complexes [49,73].

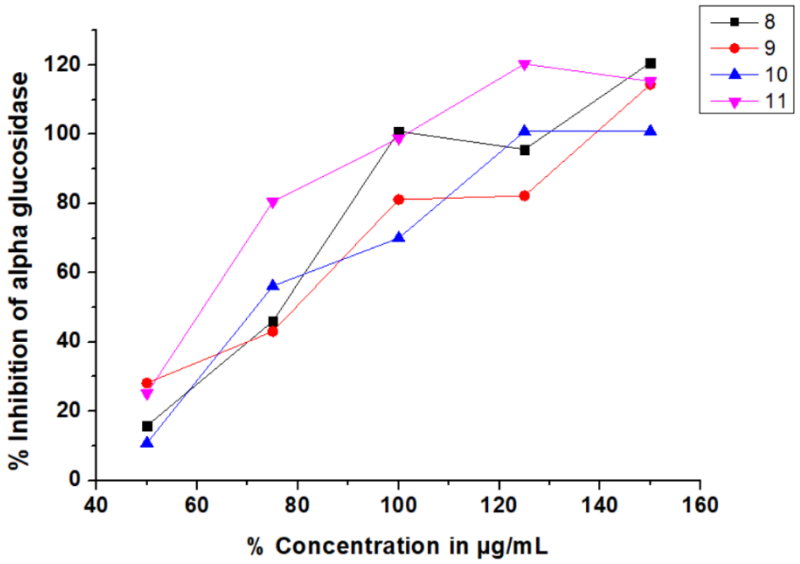

Fig. 39. α-Glucosidase inhibitory activity of complexes **8-11**.

Table 9 Antidiabetic parameters of complexes **8-11**.

Complex	IC_{50} (µg/mL)	α-glucosidase activity ($µg^{-1}$)
8	77.21	12.95
9	80.02	12.50
10	71.80	13.93
11	60.56	16.51

3.9.6 α-Amylase inhibition activity

The α-amylase activity of complexes **8-11** was also collected reported α-amylase inhibition assay [72]. α-amylase is a vital digestive enzyme used in breaking starch into glucose before uptake into blood [74]. This enzyme has been considered as one of the most targets in the treatment o diabetes patients [75]. The α-amylase inhibition activity was determined from the % inhibition *vs.* concentration plot (Fig. 40). α-amylase inhibition parameters of **8-11** are given in Table 10. Complex **11** showed the highest α-amylase

inhibition activity to due to the minimum energy gap (ΔE) in FMO and having the highest global softness. On the other hand complex, **9** showed the least inhibition activity due to its highest global hardness and maximum ΔE in FMO. The inhibition results of complexes **8-11** revealed that these complexes might be useful for inhibiting the α-amylase inhibition activity.

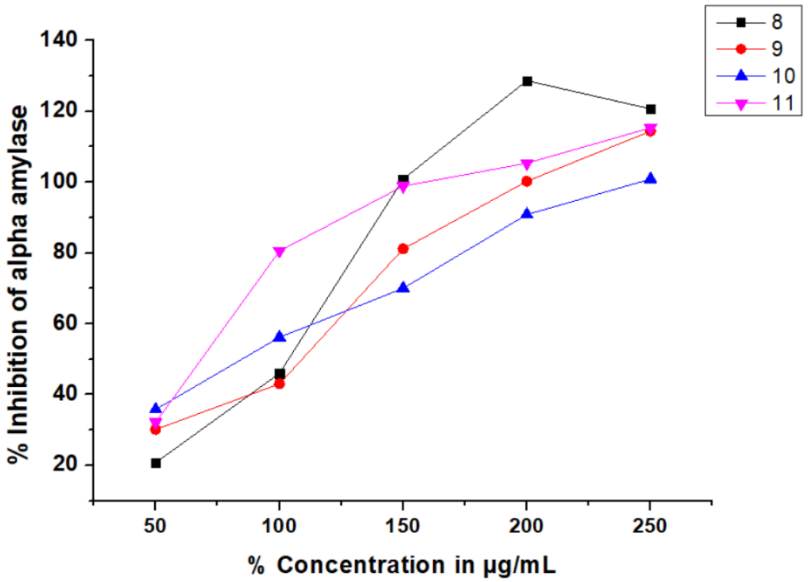

Fig. 40. α-Amylase inhibitory activity of complexes **8-11**.

Table 10 Antidiabetic parameters of complexes **8-11**.

Complex	IC_{50} (µg/mL)	α-amylase activity ($µg^{-1}$)
8	104.83	9.54
9	111.10	9.00
10	86.96	11.50
11	68.98	14.49

3.10 Computational Study

3.10.1 Optimized structure of complexes

Full geometry optimizations were carried out using the density functional theory (DFT) method at the B3LYP level for complex [75], all elements except Cu were assigned the 6-31G(d) basis set [76]. LANL2DZ with effective core potential for Cu atom was used [77]. The DFT optimized structure of complexes **1-3** is given in Fig. 41-43 and bond length and angle are given in Table 11. The vibrational frequency calculations were performed to

ensure that the optimized geometries represent the local minimum and that there is only a positive Eigenvalue. In the computational model, the cationic complex was taken into account. All calculations were performed with the GAUSSIAN 09 program [78] with the aid of the Gauss View visualization program. Vertical electronic excitations based on B3LYP geometries were computed using the time-dependent density functional theory (TD-DFT optimized) formalism [79] in DMSO, using a conductor-like polarizable continuum model (CPCM) [80]. DFT analysis was performed to elucidate the bonding pattern. In all complexes distorted octahedral geometry remains around the V(IV) ion. In complex **1**, the resulting coordination sphere has N_3O_3 donors atoms whereas in **2** and **3** N_5O donor atoms constitute the coordination sphere.

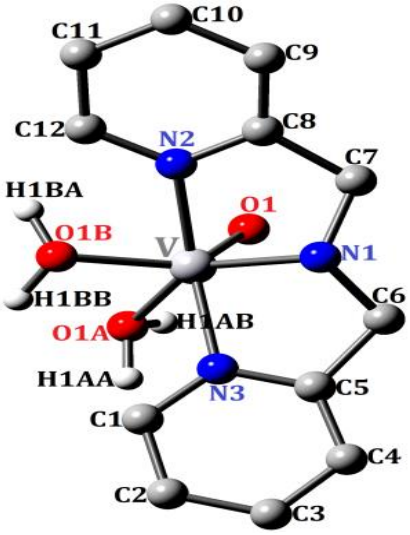

Fig. 41. Optimized structure of complex **1**.

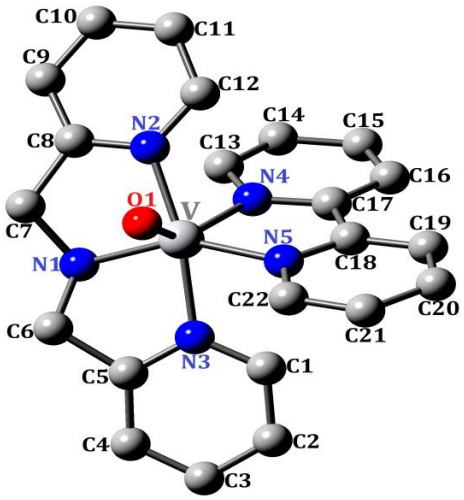

Fig. 42. Optimized structure of complex **2**.

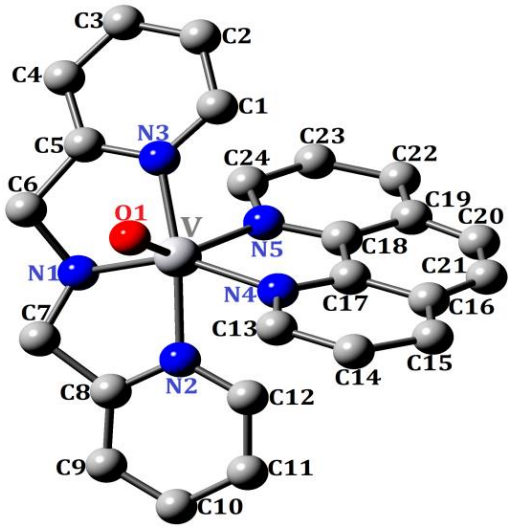

Fig. 43. Optimized structure of complex **3**.

Geometry optimization complexes **4-11** have performed using the density functional theory (DFT) method [81]. Optimized molecular structures are shown in Fig. 44-51. and the B3LYP calculated geometric parameters *viz.*, bond lengths, bond angles, optimized energies, frontier molecular orbitals (HOMO and LUMO) and energy gap (ΔE) have been also calculated using the B3LYP-6-31G/LanL2DZ levels using the Gaussian 09 program package. The V(V) ion has a distorted octahedral coordination environment. The proligand Schiff base acts as tridentate ligand (NOO) (L^{2-}) and maltol (L^{-}) acts as bidentate (OO) ligand. The donor atoms of proligands (NOO) and hydroxyl oxygen atom of complex whereas axial positions are occupied by carbonyl oxygen atom of maltol / ethyl maltol and oxygen atom of oxido group. In remaining complexes axial positions are occupied by oxido O atom and O/N atom of tridentate Schiff base. The sum (∑) of the transoid bond angles in all complexes are not equal to 360°, suggesting that the base plane is not perfectly square planar, in agreement with a distorted octahedral coordination geometry Table 11 [81-84]. The transoid and cisoid angles are deviated from 180° and 90°, again confirming that the coordination geometry around V(V) centre is distorted octahedral. Also, these six-coordinate oxidovanadium (V) complexes are tetragonally distorted ($T = R_{in}/R_{out}$) [81-84]. The value of the present complexes remains in the range of 0.83-0.9 Å, revealing that the complexes show a dynamic John-Teller distortion [81].

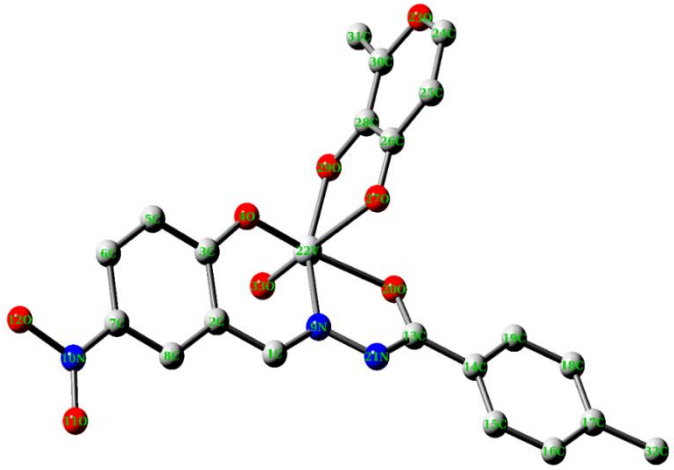

Fig. 44. Optimized structure of complex **4**.

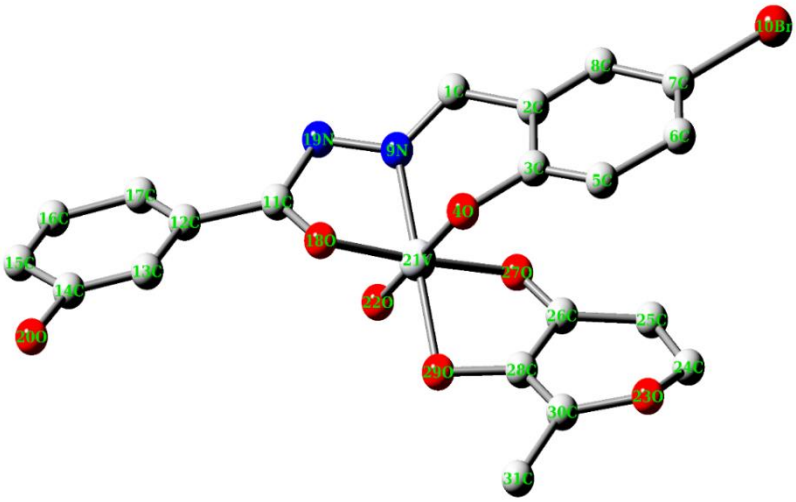

Fig. 45. Optimized structure of complex **5**.

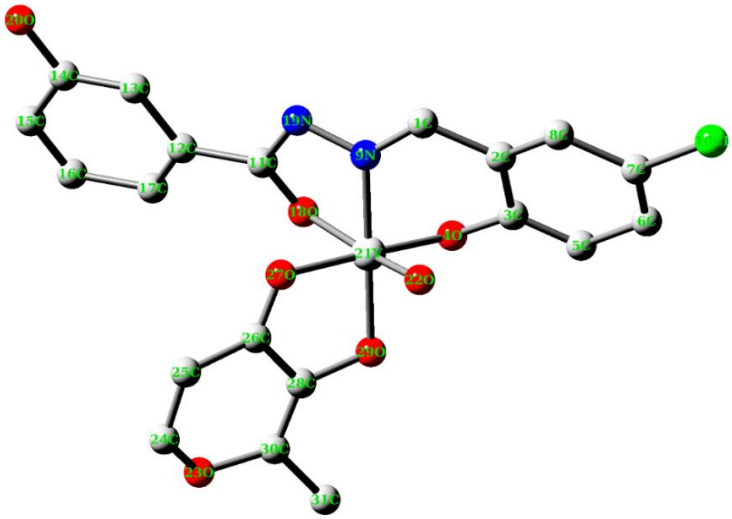

Fig. 46. Optimized structure of complex **6**.

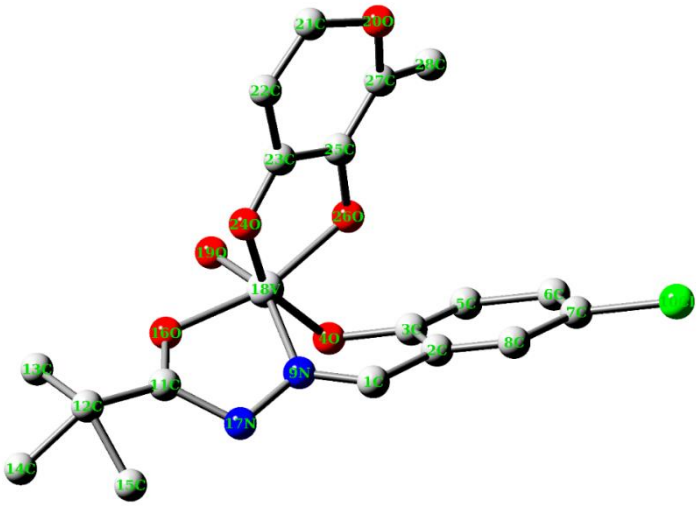

Fig. 47. Optimized structure of complex **7**.

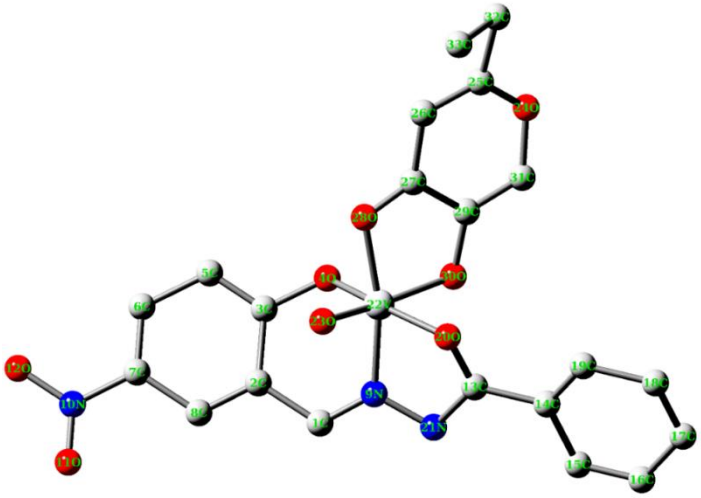

Fig. 48. Optimized structure of complex **8**.

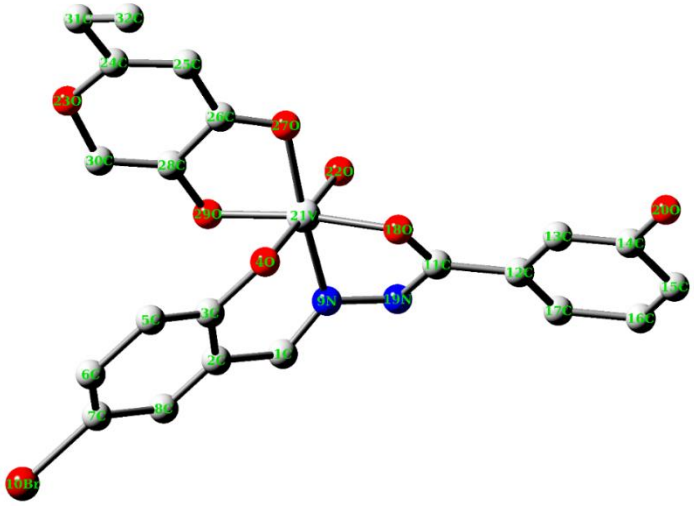

Fig. 49. Optimized structure of complex **9**.

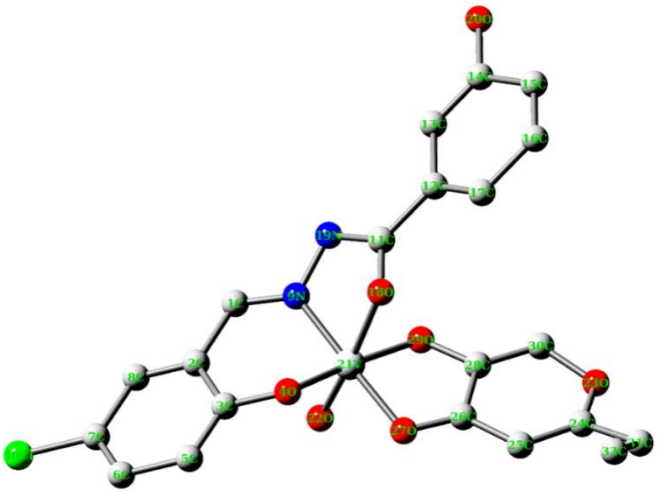

Fig. 50. Optimized structure of complex **10.**

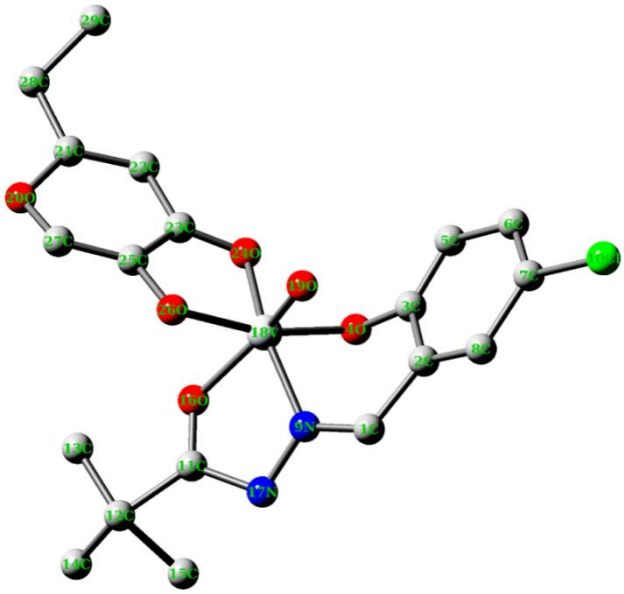

Fig. 51. Optimized structure of complex **11**.

Table 11 Theoretical Bond lengths [Å] and angles [°] for complexes **1-11**.

1			
Bond length			
V-N(1)	1.453	V-O(1)A	1.070
V-N(2)	1.535	V-O(1)B	1.084
V-N(3)	1.578	V-O(1)	0.825
Bond angles			
N(3)-V-N(1)	65.785	N(2)-V-O(1)A	121.041
N(3)-V-N(2)	132.720	O(1)A-V-O(1)B	66.903
N(1)-V-N(2)	66.934	O(1)-V-O(1)A	53.097
N(3)-V-O(1)B	106.238	O(1)-V-O(1)B	120.000

N(1)-V-O(1)B	121.072	O(1)-V-N(2)	174.142
N(2)-V-O(1)B	54.138	O(1)-V-N(1)	118.096
N(3)-V-O(1)A	172.022	O(1)-V-N(3)	53.141
N(1)-V-O(1)A	118.926		
2			
Bond length			
V-N(1)	1.455	V-N(4)	1.258
V-N(2)	1.576	V-N(5)	1.376
V-N(3)	1.535	V-O(1)	0.824
Bond angles			
N(3)-V-N(1)	66.939	N(2)-V-N(5)	177.333
N(3)-V-N(2)	132.697	N(2)-V-N(4)	99.946
N(1)-V-N(2)	65.758	O(1)-V-N(2)	49.972
N(3)-V-N(5)	49.971	O(1)-V-N(1)	115.730
N(3)-V-N(4)	127.356	O(1)-V-N(3)	177.333
N(1)-V-N(5)	116.910	O(1)-V-N(5)	127.359
N(1)-V-N(4)	165.695	O(1)-V-N(4)	49.974
3			
Bond length			
V-N(1)	1.451	V-N(4)	1.181
V-N(2)	1.573	V-N(5)	1.195
V-N(3)	1.534	V-O(1)	0.825
Bond angles			
N(3)-V-N(1)	67.078	N(2)-V-N(5)	92.830
N(3)-V-N(2)	132.930	N(2)-V-N(4)	179.316
N(1)-V-N(2)	65.851	O(1)-V-N(2)	46.747
N(3)-V-N(5)	134.239	O(1)-V-N(1)	112.598
N(3)-V-N(4)	46.389	O(1)-V-N(3)	179.679
N(1)-V-N(5)	158.682	O(1)-V-N(5)	46.083
N(1)-V-N(4)	113.468	O(1)-V-N(4)	133.933
4			
Bond lengths			
V(22)-O(4)	1.863	V(22)-O(29)	1.868
V(22)-O(20)	1.865	V(22)-O(33)	1.636
V(22)-O(27)	1.866	V(22)-N(9)	1.887
Bond angles			
O(4)-V(22)-N(9)	95.593	N(9)-V(22)-O(33)	89.664
O(4)-V(22)-O(27)	89.094	O(20)-V(22)-O(27)	86.246
O(4)-V(22)-O(29)	88.541	O(20)-V(22)-O(29)	96.998
O(4)-V(22)-O(33)	89.487	O(20)-V(22)-O(33)	95.727
N(9)-V(22)-O(20)	79.260	O(27)-V(22)-O(29)	87.951
N(9)-V(22)-O(27)	96.330	O(29)-V(22)-O(33)	86.131

5			
Bond lengths			
V(21)-O(4)	1.872	V(21)-O(27)	1.871
V(21)-O(18)	1.826	V(21)-O(29)	1.862
V(21)-O(22)	1.614	V(21)-N(9)	1.827
Bond angles			
O(4)-V(21)-N(9)	93.905	N(9)-V(21)-O(27)	94.893
O(4)-V(21)-O(18)	88.448	O(18)-V(21)-O(22)	91.362
O(4)-V(21)-O(27)	90.910	O(18)-V(21)-O(29)	98.379
O(4)-V(21)-O(29)	86.156	O(22)-V(21)-O(27)	89.281
N(9)-V(21)-O(18)	81.612	O(22)-V(21)-O(29)	93.814
N(9)-V(21)-O(22)	86.123	O(27)-V(21)-O(29)	85.116
6			
Bond lengths			
V(21)-O(4)	1.848	V(21)-O(27)	1.880
V(21)-O(18)	1.864	V(21)-O(29)	1.881
V(21)-O(22)	1.635	V(21)-N(9)	1.869
Bond angles			
O(4)-V(21)-N(9)	92.229	N(9)-V(21)-O(27)	96.818
O(4)-V(21)-O(18)	93.620	O(18)-V(21)-O(27)	79.266
O(4)-V(21)-O(22)	94.544	O(18)-V(21)-O(29)	105.617
O(4)-V(21)-O(29)	83.708	O(22)-V(21)-O(27)	94.697
N(9)-V(21)-O(18)	80.266	O(22)-V(21)-O(29)	87.232
N(9)-V(21)-O(22)	87.413	O(27)-V(21)-O(29)	88.109
7			
Bond lengths			
V(18)-O(4)	1.859	V(18)-O(24)	1.885
V(18)-O(16)	1.870	V(18)-O(26)	1.892
V(18)-O(19)	1.636	V(18)-N(9)	1.911
Bond angles			
O(4)-V(18)-N(9)	85.096	N(9)-V(18)-O(26)	112.532
O(4)-V(18)-O(16)	119.342	O(16)-V(18)-O(19)	79.671
O(4)-V(18)-O(19)	88.530	O(16)-V(18)-O(24)	83.750
O(4)-V(18)-O(24)	155.044	O(16)-V(18)-O(26)	162.891
O(4)-V(18)-O(26)	73.791	O(19)-V(18)-O(24)	106.063
N(9)-V(18)-O(16)	80.960	O(19)-V(18)-O(26)	90.342
N(9)-V(18)-O(19)	153.289	O(24)-V(18)-O(26)	85.752
N(9)-V(18)-O(24)	89.856		
8			
Bond lengths			
V(22)-O(4)	1.869	V(22)-O(28)	1.873
V(22)-O(20)	1.863	V(22)-O(30)	1.878

V(22)-O(23)	1.636	V(22)-N(9)	1.884
Bond lengths			
O(4)-V(22)-N(9)	92.731	N(9)-V(22)-O(30)	101.905
O(4)-V(22)-O(20)	163.466	O(20)-V(22)-O(23)	94.255
O(4)-V(22)-O(23)	100.682	O(20)-V(22)-O(28)	107.356
O(4)-V(22)-O(28)	81.428	O(20)-V(22)-O(30)	77.584
O(4)-V(22)-O(30)	88.847	O(23)-V(22)-O(28)	84.025
N(9)-V(22)-O(20)	81.060	O(28)-V(22)-O(30)	88.801
N(9)-V(22)-O(23)	86.512		
9			
Bond lengths			
V(21)-O(4)	1.855	V(21)-O(27)	1.873
V(21)-O(18)	1.859	V(21)-O(29)	1.877
V(21)-O(22)	1.636	V(21)-N(9)	1.879
Bond angles			
O(4)-V(21)-N(9)	95.508	N(9)-V(21)-O(29)	93.703
O(4)-V(21)-O(18)	92.889	O(18)-V(21)-O(22)	85.781
O(4)-V(21)-O(27)	90.264	O(18)-V(21)-O(27)	99.215
O(4)-V(21)-O(29)	84.850	O(22)-V(21)-O(27)	87.128
N(9)-V(21)-O(18)	79.682	O(22)-V(21)-O(29)	96.808
N(9)-V(21)-O(22)	87.075	O(27)-V(21)-O(29)	87.651
10			
Bond lengths			
V(21)-O(4)	1.858	V(21)-O(27)	1.872
V(21)-O(18)	1.865	V(21)-O(29)	1.876
V(21)-O(22)	1.636	V(21)-N(9)	1.880
Bond angles			
O(4)-V(21)-N(9)	94.600	N(9)-V(21)-O(29)	91.866
O(4)-V(21)-O(18)	96.030	O(18)-V(21)-O(27)	99.484
O(4)-V(21)-O(22)	90.149	O(18)-V(21)-O(29)	80.716
O(4)-V(21)-O(27)	85.465	O(22)-V(21)-O(27)	89.196
N(9)-V(21)-O(18)	78.959	O(22)-V(21)-O(29)	94.151
N(9)-V(21)-O(22)	92.360	O(27)-V(21)-O(29)	87.945
11			
Bond lengths			
V(18)-O(4)	1.840	V(18)-O(24)	1.872
V(18)-O(16)	1.869	V(18)-O(26)	1.879
V(18)-O(19)	1.636	V(18)-N(9)	1.921
Bond angles			
O(4)-V(18)-N(9)	82.865	N(9)-V(18)-O(26)	109.687
O(4)-V(18)-O(16)	114.428	O(16)-V(18)-O(19)	152.116
O(4)-V(18)-O(19)	90.307	O(16)-V(18)-O(24)	96.231

O(4)-V(18)-O(24)	79.527	O(16)-V(18)-O(26)	74.830
N(9)-V(18)-O(16)	80.432	O(19)-V(18)-O(24)	101.012
N(9)-V(18)-O(19)	90.688	O(19)-V(18)-O(26)	83.592
N(9)-V(18)-O(24)	158.833	O(24)-V(18)-O(26)	89.277

3.10.2 HOMO-LUMO analysis

Interestingly, the singly occupied molecular orbital (SOMO/α-spin HOMO) is localized completely on the proligand in **4** and **6** and on tilery on metal centre in **5** and **7** in maltol (co-ligand) containing complexes except in HOMO-3. Similarly, ethyl maltol-containing complexes (**8-11**) the HOMO-LUMO energies have been estimated to find out the energetic nature and energy distribution (Fig. 52-59). The HOMO frontier molecular HOMO represents electron releasing ability whereas LUMO gives information about the electron gain ability of the ligand. The estimated HOMO and LUMO energy values for complexes **4-11** are given in Tables 12 and 13. The energy gap (ΔE) between HOMO and LUMO frontier orbitals is the critical parameter in evaluating the molecular electrical transport properties *viz.*, chemical reactivity, kinetic stability and softness-hardness of a chemical moiety. The chemical (global) hardness is a good indicator of chemical stability.

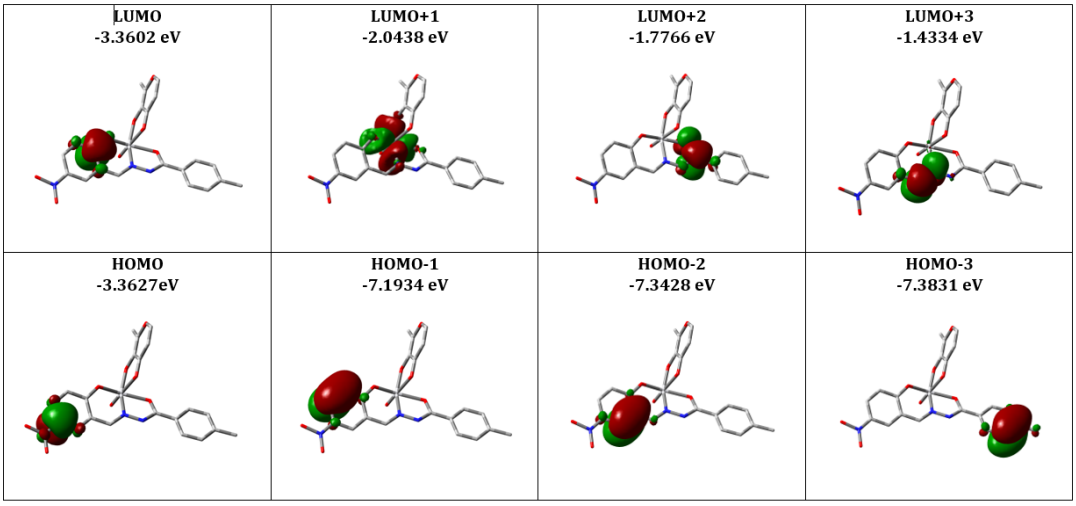

Fig. 52. HOMO-LUMO of complex **4**.

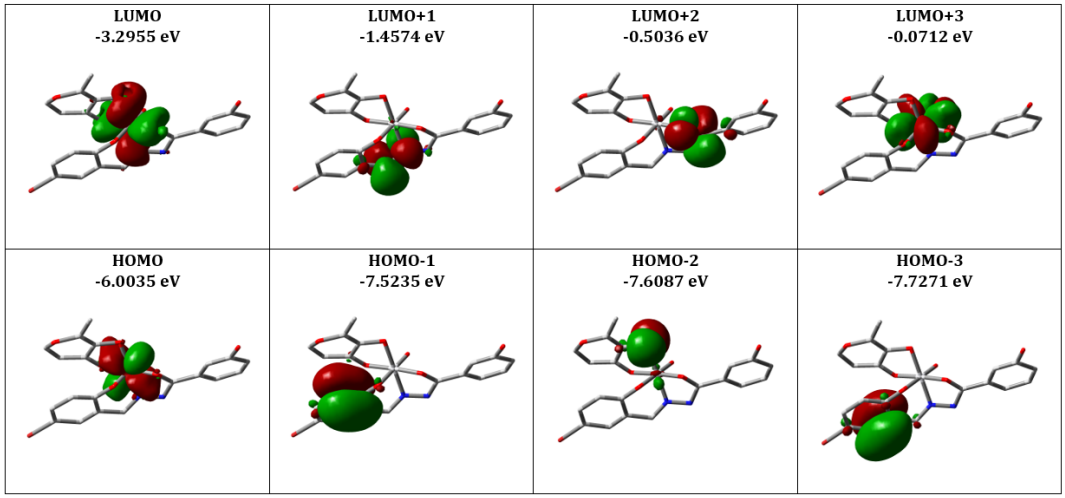

Fig. 53. HOMO-LUMO of complex **5**.

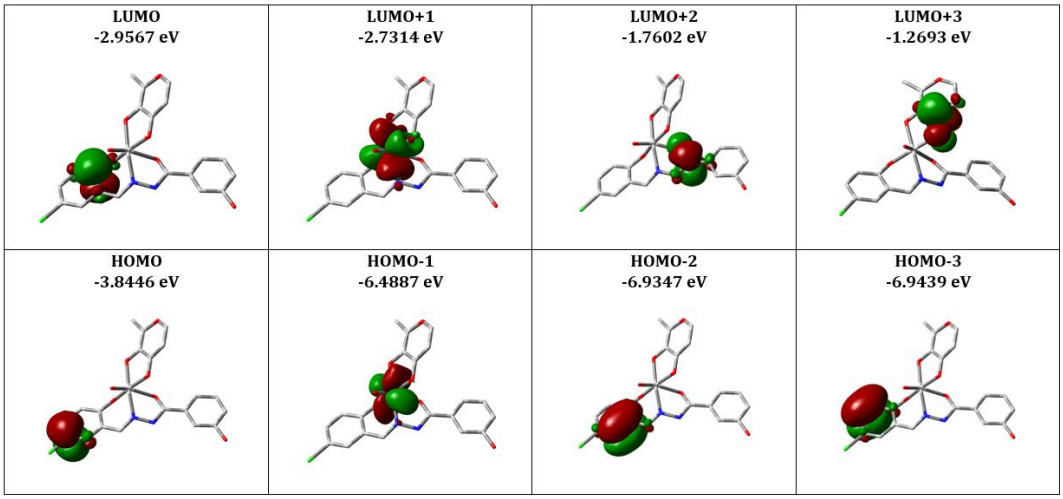

Fig. 54. HOMO-LUMO of complex **6**.

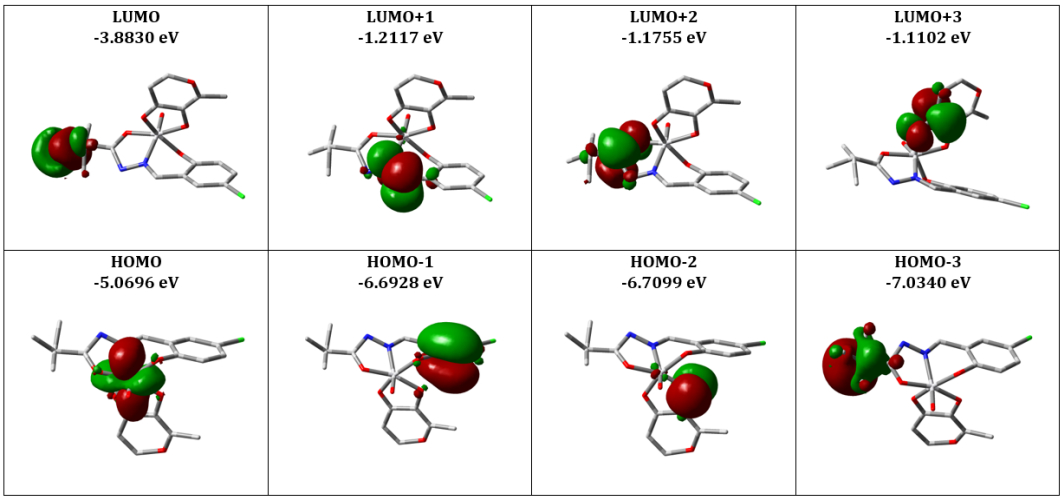

Fig. 55. HOMO-LUMO of complex **7**.

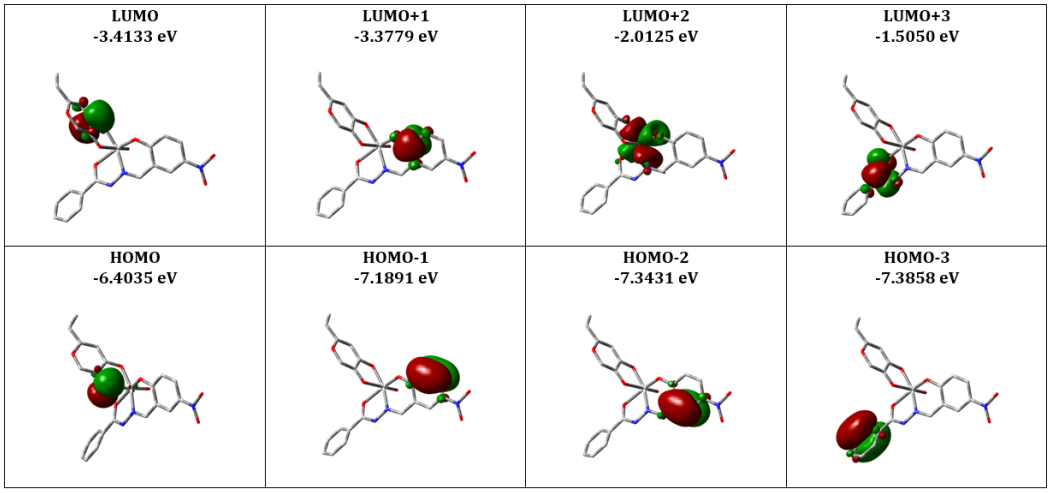

Fig. 56. HOMO-LUMO of complex **8**.

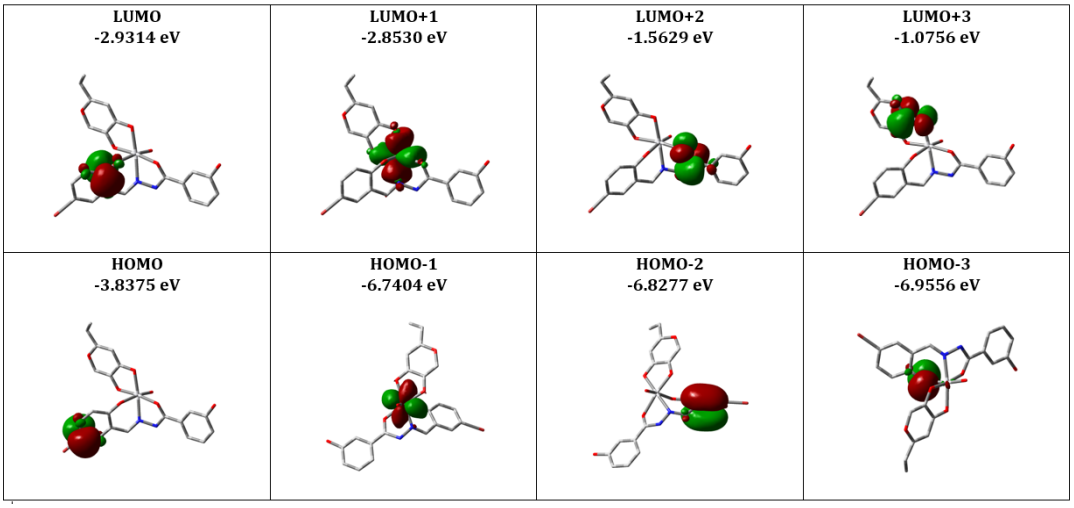

Fig. 57. HOMO-LUMO of complex **9**.

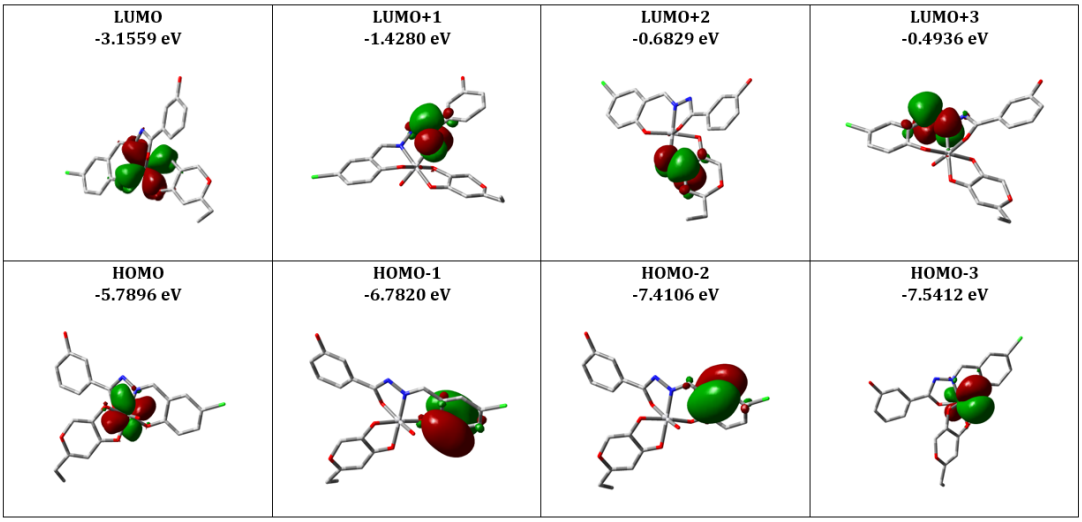

Fig. 58. HOMO-LUMO of complex **10**.

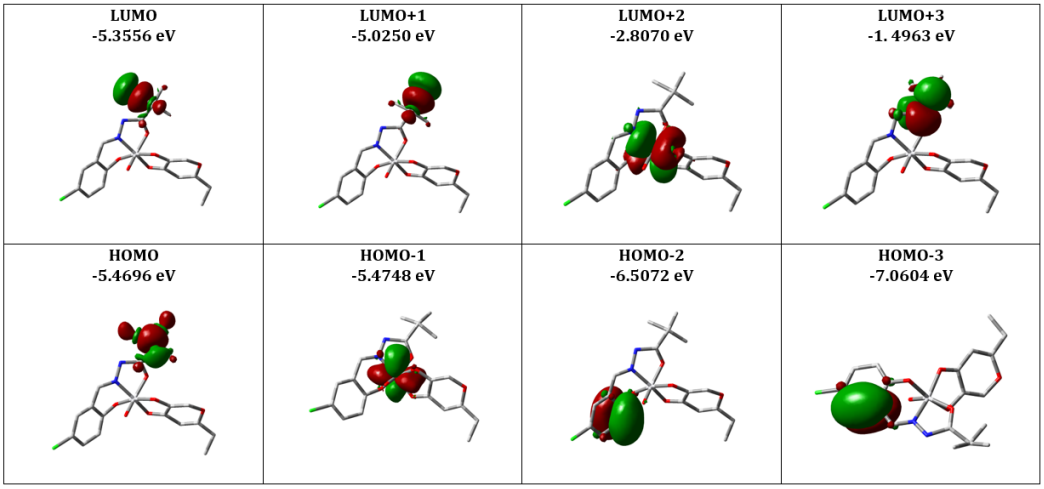

Fig. 59. HOMO-LUMO of complex **11**.

3.10.3 Global reactivity parameters

The estimated values of the reactivity descriptors of complexes **4-11** are given in Tables 12 and 13. The energies of HOMO and LUMO frontier molecular orbitals are useful in quantum chemical calculations and are related to ionization potential (IP) and electron affinity as: IP = $-E_{HOMO}$ and EA = $-E_{LUMO}$. The other crucial chemical descriptors such as chemical potential (μ) the resistance to alternation in electron distribution are related to the stability and reactivity of a chemical moiety. The global softness (S) is the inverse of the hardness (η). The chemical species having a small ΔE is referred to as soft and with large ΔE as hard species. The electronegativity (χ) of a chemical molecule yields information about the negative of the partial derivative of the energy (E) of a molecule concerning the number of the electron (N) with a constant external potential ($\upsilon(\eta)$). Similarly, the global electrophilicity (ω) descriptor gives the information about lowering of the energy due to maximal electron flow between donor and acceptor atoms [85]. These descriptors can be calculated from Koopman's theorem given in Tables 12 and 13 [86]. The negative chemical potential (μ) of the complexes (**4-11**) suggests the stability of complexes. The magnitude of hardness reveals the resistance towards the distortion of the electron cloud of complexes with perturbation and less polarizability [87]. The values of ω are suggestive of good electrophile-nucleophile combination in complexes **4-11**.

Table 12 Global reactivity descriptors vanadium complexes **4-7** in calculated by DFT/B3LYP/LANL2DZ basic.

Molecular properties	**Mathematical description**	**4**	**5**	**6**	**7**
E_{HOMO} (eV)	Energy of HOMO	-3.362	-6.003	-3.844	-5.069
E_{LUMO} (eV)	Energy of LUMO	-3.360	-3.295	-2.956	-3.883
Energy gap (eV)	$\Delta E_g = E_{HOMO} - E_{LUMO}$	0.002	2.708	0.888	1.186
Ionization potential (eV)	$IP = -E_{HOMO}$	3.362	6.003	3.844	5.069
Electron Affinity (eV)	$EA = -E_{LUMO}$	3.360	3.295	2.956	3.883
Electronegativity (eV)	$(\chi) = -½ (E_{Homo} + E_{Lumo})$	3.361	4.649	3.400	4.476
Chemical Potentia (eV)	$\mu = ½ (E_{Homo} + E_{Lumo})$	-3.361	-4.649	-3.400	-4.476
Global Hardness (eV)	$(\eta) = - ½ (E_{Homo} - E_{Lumo})$	0.001	1.354	0.444	0.593
Softness (eV^{-1})	$(S) = 1/2\eta$	500	0.369	1.126	0.843
Electrophilicity index (ω)	$\omega = \mu^2/2\eta$	5648.16	7.98	13.01	16.89

Table 13 Global reactivity descriptors vanadium complexes **8-11** in calculated by DFT/B3LYP/LANL2DZ basic.

Molecular properties	**Mathematical description**	**8**	**9**	**10**	**11**
E_{HOMO} (eV)	Energy of HOMO	-6.403	-3.837	-5.789	-5.469
E_{LUMO} (eV)	Energy of LUMO	-3.413	-2.931	-3.155	-5.355
Energy gap (eV)	$\Delta E_g = E_{HOMO} - E_{LUMO}$	2.990	0.906	2.634	0.114
Ionization potential (eV)	$IP = -E_{HOMO}$	6.403	3.837	5.789	5.469
Electron Affinity (eV)	$EA = -E_{LUMO}$	3.413	2.931	3.155	5.355

Electronegativity (eV)	$(\chi) = -½ (E_{Homo} + E_{Lumo})$	4.908	3.384	4.472	5.412
Chemical Potential (eV)	$\mu = ½ (E_{Homo} + E_{Lumo})$	-4.908	-3.384	-4.472	-5.412
Global Hardness (eV)	$(\eta) = - ½ (E_{Homo} - E_{Lumo})$	1.495	0.453	1.317	0.057
Softness (eV^{-1})	$(S) = 1/2\eta$	0.334	1.103	0.379	8.771
Electrophilicity index(ω)	$\omega = \mu^2/2\eta$	8.056	12.639	7.592	256.927

3.10.4 Electron density

The surfaces of spin density all complexes (**4-11**) are shown Fig. 60-67. Most of the electron density is located on the V(V) centre. The spin population, Mulliken population and natural population on the V(V) centre are given in Table 14.

Table 14 The spin densities of metal and donor atoms for complexes **4-11**.

Complexes	Metal and Donor atom	Spin population	Mulliken population	Natural population
4	V(22)	+0.383	+0.576	+0.696
	N(9)	-0.257	-0.182	-0.265
	O(4)	-0.522	-0.432	-0.545
	O(20)	-0.518	-0.327	-0.573
	O(27)	-0.533	-0.352	-0.619
	O(29)	-0.545	-0.380	-0.583
	O(33)	-0.214	-0.318	-0.294
5	V(21)	+0.375	+0.514	-0.284
	N(9)	-0.240	-0.171	-0.092
	O(4)	-0.612	-0.440	-0.301
	O(18)	-0.442	-0.259	-0.220
	O(22)	-0.346	-0.410	-0.087
	O(27)	-0.495	-0.283	-0.246
	O(29)	-0.581	-0.434	-0.301
6	V(21)	+0.430	+0.568	-0.262
	N(9)	-0.263	-0.161	-0.101
	O(4)	-0.582	-0.453	-0.342
	O(18)	-0.507	-0.333	-0.251
	O(22)	-0.320	-0.387	-0.056

	O(27)	-0.540	-0.357	-0.274
	O(29)	-0.581	-0.405	-0.294
7	V(18)	+0.482	+0.581	-0.171
	N(9)	-0.267	-0.191	-0.104
	O(4)	-0.567	-0.420	-0.320
	O(16)	-0.522	-0.306	-0.242
	O(19)	-0.282	-0.358	-0.053
	O(24)	-0.518	-0.350	-0.260
	O(26)	-0.607	-0.436	-0.309
8	V(22)	+0.402	+0.533	+0.898
	N(9)	-0.208	-0.123	-0.141
	O(4)	-0.528	-0.417	-0.282
	O(20)	-0.490	-0.319	-0.278
	O(23)	-0.329	-0.395	-0.253
	O(28)	-0.469	-0.261	-0.283
	O(30)	-0.629	-0.500	-0.347
9	V(21)	+0.442	+0.561	-0.287
	N(9)	-0.246	-0.164	-0.100
	O(4)	-0.634	-0.507	-0.312
	O(18)	-0.450	-0.280	-0.221
	O(22)	-0.375	-0.434	-0.087
	O(27)	-0.477	-0.284	-0.241
	O(29)	-0.610	-0.458	-0.310
10	V(21)	+0.411	+0.553	-0.285
	N(9)	-0.250	-0.141	-0.098
	O(4)	-0.591	-0.473	-0.338
	O(18)	-0.528	-0.342	-0.263
	O(22)	-0.295	-0.374	-0.039
	O(27)	-0.453	-0.247	-0.225
	O(29)	-0.645	-0.489	-0.328
11	V(18)	+0.483	+0.574	-0.227
	N(9)	-0.238	-0.170	-0.092
	O(4)	-0.624	-0.457	0.353
	O(16)	-0.578	-0.407	-0.290
	O(19)	-0.328	-0.373	-0.073
	O(24)	-0.477	-0.285	-0.240
	O(26)	-0.619	-0.446	-0.323

Additionally, the natural bond order analysis of the complexes **4-11** was performed using B3LYP/LANL2DZ level basics set. The natural bond orbital (NBO) analysis is used to explore inter and intra molecular interactions among the bonds [88], which

corresponds to a stabilizing donor-acceptor interaction [89]. The natural atomic charges of donor atoms are listed in Table 14. The maximum positive charge on V(V) centers in **4** and **8** found to be +0.696e and +0.898e, respectively. In all complexes, donor atoms have negative charges. According to NBO analysis, the natural electronic configuration of V is: [Core] 4s(0.22), 3d(3.59), 4p(0.37). Therefore, core electrons (18), valence electrons (4.183) on 4s, 3d and 4p orbitals and Rydberg electrons (0.093) mainly on 4p, 4d and 5p orbitals yield 22.89 electrons and +0.696 charge on V atom in **1**. The valence electrons and Rydberg electrons for other complexes (**5-11**) are listed in Table 15. This is persistent with the calculated natural charge on V atom 0.11 in complexes, which corresponds to the difference between 22.363 and total no. of electrons in the isolated V atom 23e in **4**. Similar results were obtained in the remaining complexes (**5-11**). On the perusal of data of Tables 14 and 15, it is found that the formal charges of the donor atoms indicate that the electron distribution is not confined to the coordination bonds as the values of DFT calculated formal charges of V centres are small-scale than +5. Scale decreases in the formal charge value are being the complexation, with charge transfer from vanadium to the ligand (MLCT) [90].

Generally, V(V) centre in each complex plays as an electron acceptor in coordinating with proligand (Schiff base) and maltol (as coligand). Electron density is transferred from the lone pair electron of donor atoms to the unoccupied orbitals on vanadium with lower stabilization energies [91].

Table 15 Natural electron configuration of complexes **4-11**.

Complex	Natural Electronic Configuration					Core	Valence	Rydberg
	4s	3d	4p	4d	5s			
4	0.22	3.59	0.37	0.09	-	17.974	4.183	0.093
5	0.24	3.86	0.42	0.12	-	17.977	4.521	0.125
6	0.23	3.59	0.37	0.09	-	17.977	4.194	0.099
7	0.24	3.80	0.39	0.10	0.01	17.975	4.434	0.107
8	0.22	3.60	0.38	0.09	-	17.978	4.201	0.096
9	0.23	3.57	0.36	0.09	-	17.979	4.161	0.097
10	0.24	3.84	0.40	0.12	-	17.977	4.485	0.125
11	0.24	3.78	0.40	0.11	0.01	17.974	4.418	0.123

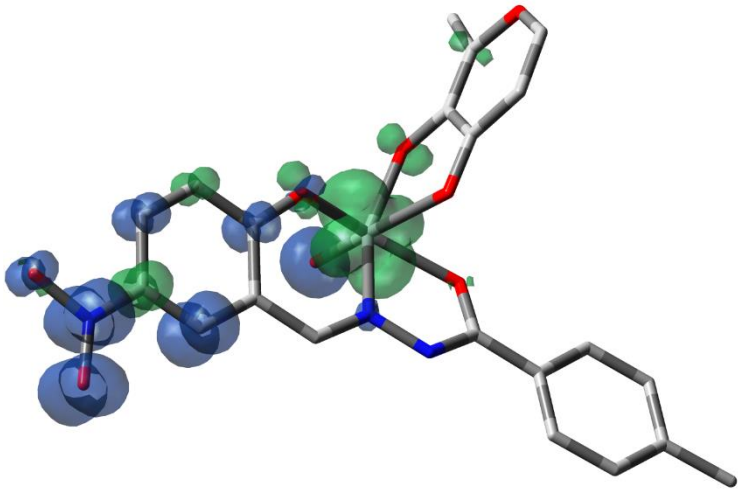

Fig. 60. Spin density of complex **4**.

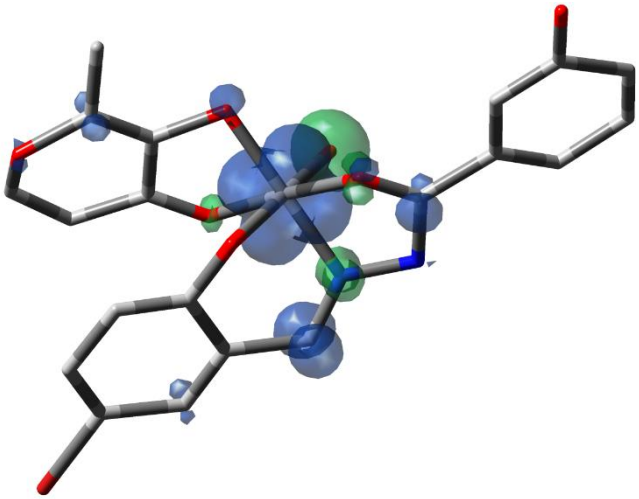

Fig. 61. Spin density of complex **5**.

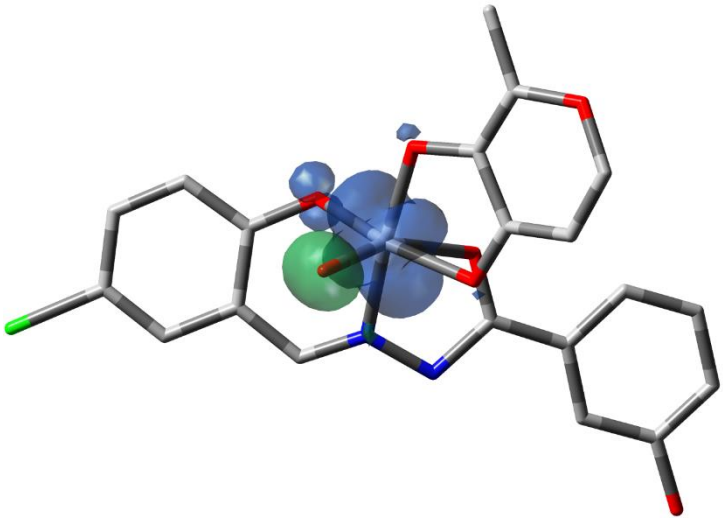

Fig. 62. Spin density of complex **6**.

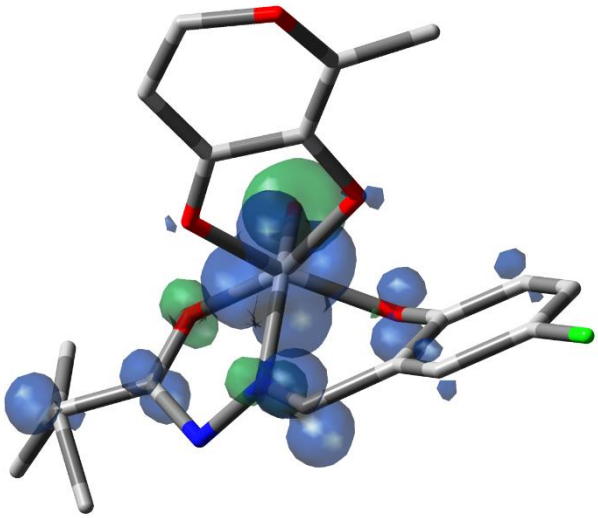

Fig. 63. Spin density of complex **7**.

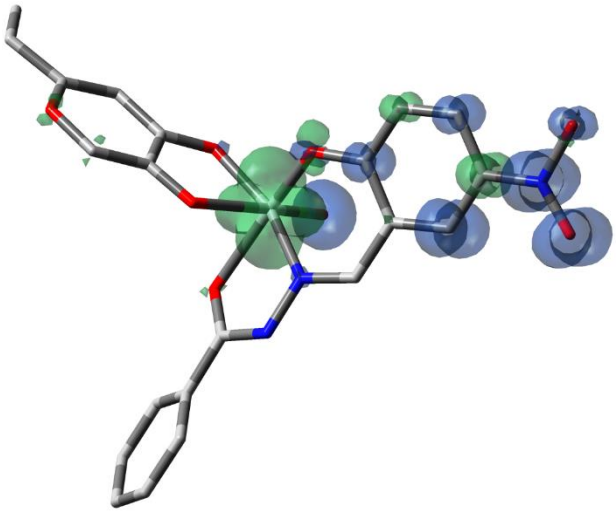

Fig. 64. Spin density of complex **8**.

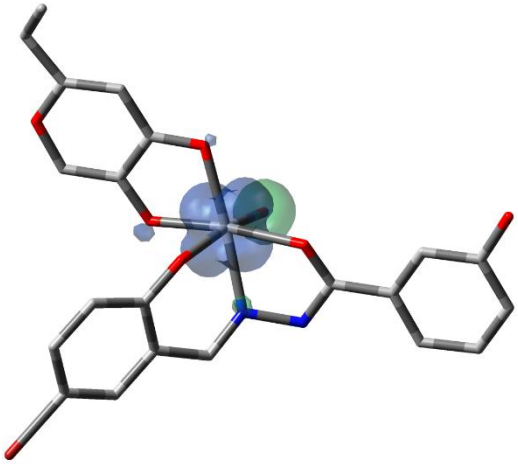

Fig. 65. Spin density of complex **9**.

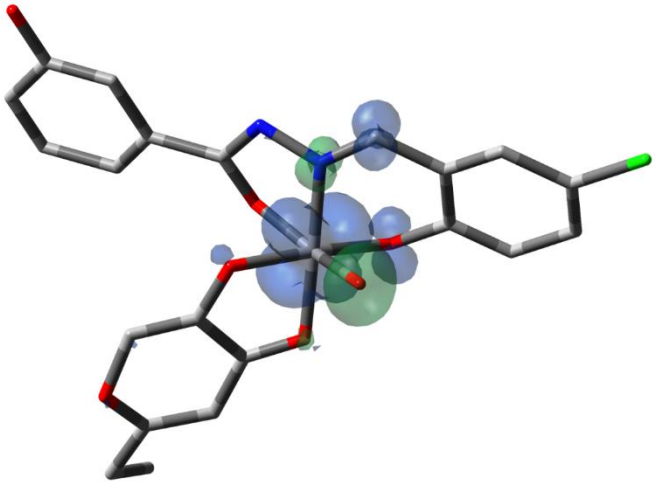

Fig. 66. Spin density of complex **10**.

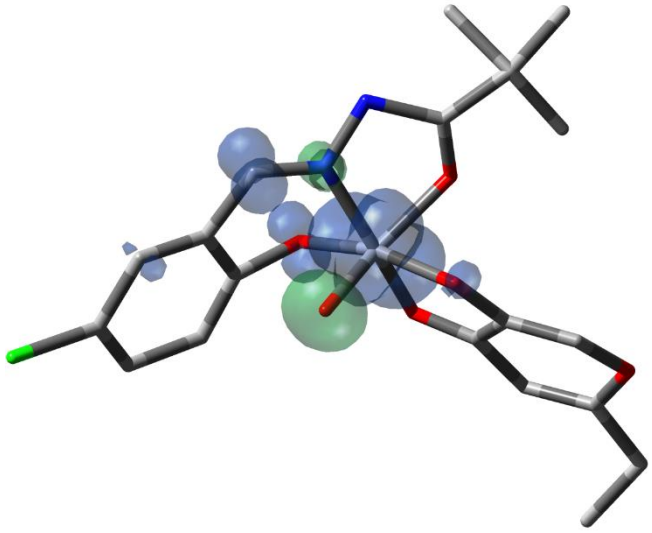

Fig. 67. Spin density of complex **11**.

4 Conclusions

We have synthesized **1-11** oxidovanadium(IV/V) complexes with different ligands using in-situ process. Recent interest of inorganic, bioinorganic chemists and pharmacologists in antidiabetic oxidovanadium(IV) complexes has resulted in synthesis, characterization, and exploration of antidiabetic proportions of three new oxidovanadium(IV) complexes. All the complexes have been characterized by various physicochemical techniques. The molecular structures show the presence of six donor atoms around the oxidovanadium(IV) and hence octahedral geometry is proposed. Paramagnetic d^1 configuration of vanadium complexes (**1-3**) were supported by EPR spectroscopy. These complexes were also evaluated using thermogravimetric analysis and powder X-ray diffraction techniques. The complexes show

moderate *in-vitro* α-glucosidase and α-amylase inhibition. Complex **3** has an interesting insulin-like activity. Complexes **4-11** oxidovanadium(V) derived from maltol / ethyl maltol and various tridentate aroylhydrazones were prepared and well characterized by various spectroscopic techniques. In complexes, **4-11** d-d absorption bands were not observed in all complexes being d^0 vanadium systems. The V ions in complexes **4-11** are in octahedral coordination. In complexes, the **4-11** reduction process exhibits one-electron transfer i.e. the reduction of vanadium(V) to vanadium(IV). Hence, we may conclude that these complexes may be considered antidiabetic agents.

References

1 D.C. Crans, J.J. Smee, E. Gaidamauskas, L. Yang, Chem. Rev. 104 (2004) 849-902.

2 A.S. Tracey, G.R. Willsky, E.S. Takeuchi, Vanadium Chemistry, Biochemistry Pharmacology and Practical Applications, Taylor and Francis Group, Boca Raton, USA, 2007

3 Y. Shechter, I. Goldwaser, M. Mironchik, M. Fridkin, D. Gefel, Coord. Chem. Rev. 237 (2003) 3-11.

4 H. Sakurai, Y. Yoshikawa, H. Yasui, Chem. Soc. Rev. 37 (2008) 2383-2392.

5 D.A. Barrio, S.B. Etcheverry, Curr. Med. Chem. 17 (2010) 3632-3642.

6 A.M. Evangelou, Crit. Rev. Oncol. / Hematol. 42 (2002) 249-265.

7 A. Bishayee, A. Waghray, M.A. Patel, M. Chatterjee, Cancer Lett. 294 (2010) 1-12.

8 B. Mukherjee, B. Patra, S. Mahapatra, P. Banerjee, A. Tiwari, M. Chatterjee, Toxicol. Lett. 150 (2004) 135-143.

9 H. Sigel, A. Sigel (Eds.), Metal ions in biological systems Vanadium and its Role in Life, 31 Marcel Dekker, New York, (1995).

10 A.S. Tracey, D.C. Crans (Eds.), Vanadium Compounds. Chemistry, Biochemistry and Therapeutic Applications, ACS Symposium Series 711, ACS, Washington, D.C. (1998).

11 J.O. Nriagu (Ed.), Vanadium in the Environment. Part 1; Chemistry and Biochemistry, Part 2; Health Effects, John Wiley & Sons, New York (1998).

12 K.H. Thompson, J.H. McNeill, C. Orvig, Chem. Rev. 99 (1999) 2561-2572.

13 H. Sakurai, Y. Fujisawa, S. Fujimoto, H. Yasui, T. Takino, J. Trace Elem. Exp. Med. 12 (1999) 393-401.

14 H. Sakurai, Y. Kojima, Y. Yoshikawa, K. Kawabe, H. Yasui, Coord. Chem. Rev. 226 (2002) 187-198.

15 H. Sakurai, K. Tsuchiya, M. Nukatsuka, M. Sofue, J. Kawada, J. Endocrinol. 126 (1990) 451-459.

16 H. Sakurai, K. Tsuchiya, M. Nukatsuka, M. Sofue, J. Kawada, J. Endocrinol. 126 (1990) 451-459.

17 M. Nakai, H. Watanabe, C. Fujiwara, H. Kakegawa, T. Satoh, J. Takada, R. Matsushita, H. Sakurai, Biol. Pharm. Bull. 18 (1995) 719-725.
18 S.O. Sezer, E. Ince, A. Akdemir, O.O. Ceylan, S. Suzen, H.G.-Orhan, Xenobiotica 49 (2019) 549-556.
19 K. Pyta, A. Janas, M. Szukowska, P. Pecyna, M. Jaworska, M. Gajecka, F. Bartl, P. Przybylski. Eur. J. Med. Chem. 167 (2019) 96 -104.
20 R. Sreenivasulu, K.T. Reddy, P. Sujitha, C.G. Kumar, R.R. Raju. Bioorg. Med. Chem. 27 (2019) 1043-1055.
21 T.J. Hauke, G. Hofner, K.T. Wanner. Chem. Med. Chem. 14 (2019) 583-593.
22 U. Ghani, Bioorg. Chem. 83 (2019) 235-241.
23 H.M.A. Abumelha, J. Heterocyclic Chem. 55 (2018)1738-1745.
24 Y.C. Wu, X.D. Ding, L. Ding, Y.S. Zhang, L. Cui, L. Sun, W. Li, D. Wang, Y.F. Zhao. Eur. J. Med. Chem. 158 (2018) 247-258.
25 U.P. Singh, H.R. Bhat, A. Verma, M.K. Kumawat, R. Kaur, S.K. Gupta, R.K. Singh. RSC Adv. 3 (2013) 17335 -17348.
26 M.R.P. Kurup, E.B. Seena, M. Kuriakose, Struct. Chem. 21 (2010) 599-605.
27 R. Yanardag, T. B.Demirci, B. Ulkuseven, S. Bolkent, S. Tunali, S. Bolkent, Eur. J. Med. Chem. 44 (2009) 818-826.
28 M.N. Islam, A.A. Kumbhar, A.S. Kumbhar, M. Zeller, R.J. Butcher, M.B. Dusane, B.N. Joshi, Inorg. Chem. 49 (2010) 8237- 8246.
29 E. Apostolidis, Y.I.I. Kwon, K.Shetty, Asia Pac. J. Clin.Nutr. 15 (2006) 433-441.
30 I.P. Tripathi, M.K. Mishra, R. Tripathi, C. Mishra, A. Kamal, L. Shastri, A. Dwivedi, U.K. Shukla, K.B. Pandeya, Res. J. Chem. Sci. 4 (2014) 13-17.
31 T. Ghosh, A. Roy, S. Bhattacharya, S. Banerjee, Trans. Met. Chem. 30 (2005) 419-425.
31 W.J. Geary, Coord. Chem. Rev. 3 (1971) 81-122.
32 Y. Singh, R.N. Patel, S.K. Patel, A.K. Patel, N. Patel, R. Singh, R.J. Butcher, J.P. Jasinski, A. Gutierrez, Polyhedron 171 (2019) 155-171.
34 H. Beraldo, W.F. Nacif, L.R. Tiexeira, J.S. Rebouse, Trans. Met. Chem. 27 (2002) 85-88.
35 J.R. Carvajal, T. Roisnel, Winplntr: A Graphic Tool for Power Diffraction, Laboratoir, Lean Brillouin (CEA/CNRS) Cedex, France (2004).
36 Y. Hasebs, R. Imai, M. Hiromo, S. Uchiyama, Anal. Sci. 23 (2007) 71.
37 K. Nakamoto, Infrared and Raman spectra of Inorganic and Coordination complexes, 3rd ed., John Wiley& Sons, New York (1970).
38 K.-Y. Choi, B.-R. Kim, J. Ko, J. Chem. Crystallogr. 37 (2007) 847-852.
39 K. Nakamoto, Infrared and Raman spectra of Inorganic and Coordination complexes, 5th ed., John Wiley & Sons, New York (1997).
40 E.B. Seena, N. Mathew, M. Kuriakose, M.R.P. Kurup, Polyhedron 27 (2008) 1455-1462.
41 M. Zhang, D.M. Xian, H.H. Li, J.C. Zhang, Z.L. You, Aust. J. Chem. 65 (2012) 343-350.

42 Y.L. Sang, X.H. Zhang, X.S. Lin, Y.H. Liu, X.Y. Liu,J. Coord. Chem. 72 (2019) 3144-3155.

43 P.K. Sasmal, A.K. Patra, M. Nethaji, A.R. Chakravarty, Inorg. Chem. 46 (2007) 11112-11121.

44 S. Bhattacharya, T. Ghosh, Indian J. Chem. 38A (1999) 601-603.

45 E.J. Baran, J. Coord. Chem. 54 (2001) 215-238.

46 R. Rahchman, M. Behzad, A. Bezaatpour, V. Jahed, G. Dutkivicz, M. Kubicki, M. Saheli, Polyhedron 30 (2011) 2611-2618

47 G.D. Trian, EI. Tolis, A. Terzis, Inorg. Chim. Acta 43 (2004) 79-91.

48 L.J.H. –Benítez,P.J. –Cruz,K.E.C. –Hernández,A.S. –Peralta,M.F. –Álamo,A.F. –Parra,I.G. –Mora, S.E.C. –Blum, Inorg. Chim. Acta 480 (2018) 197-206.

49 N. Patel, A.K. Prajapati, R.N. Jadeja, R.N. Patel, S.K. Patel, V.K. Gupta, I.P. Tripathi, N. Dwivedi, Inorg. Chim. Acta 493 (2019) 20-28.

50 I.S. Fomenko, A.L. Gushchin, L.S. Shulpina, N.S. Ikonnikov, P.A. Abramov, N.F. Romashev, A.S. Poryvaev, A.M. Sheveleva, A.S. Bogomyakov, N.Y. Shmelev, M.V. Fedin, G.B. Shulpin , M.N. Sokolov, New J. Chem. 42 (2018) 16200-16210.

51 S. Kundu, S. Maity, A.N. Maity, S.-C. Ke, P. Ghosh, Dalton Trans. 42 (2013) 4586-4601.

52 T.S. Smith, C.A. Root, J.W. Kampf, P.G. Rasmussen, V.L. Pecoraro, J. Am. Chem. Soc. 122 (2000) 767-775.

53 M. Rangel, A. Leite, M.J. Amorim, E. Garribba, G. Micera, E.L. -Chruscinska, Inorg. Chem. 45(2006) 8086-8097.

54 S. Ramos, R.O. Duarte, J.J.G. Moura, M. Aureliano, Dalton Trans. (2009) 7985-7994.

55 J. Gatjens, B. Meier, Y. Adachi, H. Sakurai, D. Rehder, Eur. J. Inorg. Chem. (2006) 3575-3585.

56 M.R. Maurya, A. Arya, A. Kumar, J.C. Pessoa, Dalton Trans. (2009) 2185-2195.

57 N.D. Chasteen, L.J. Berlines, J. Reuben, (Eds.: Biological Inorg. Res.), Plenum Press, N.J. (1981) 53-119.

58 T.S. Smith, R.L. Brutto, V.L. Pecoraro, Coord. Chem. Rev. 228 (2002) 1-18.

59 S. Roy, M. Böhme, S.P. Dash, M. Mohanty, A. Buchholz, W. Plass, S. Majumder, S. Kulanthaivel, I. Banerjee, H. Reuter, W. Kaminsky, R. Dinda, Inorg. Chem. 57 (2018) 5767-5781.

60 S. Dutta, A. Chakravorty, Inorg. Chem. 32 (1993) 5343-5348.

61 A. Gomez, R. Fousto, J. Mol. Struct. 689 (2004) 199-212.

62 R.N. Jadeja, J.R. Shah, Polyhedron 26 (2004) 1677-1685.

63 M.R. Maurya, A. Arya, A. Kumar, J.C. Pessoa, Dalton Trans. (2009) 2185-2195.

62 A.G. –Zavaglia, R. Fausto, J. Mol. Struct. 639 (2004) 199-212.

63 S.M. Eimedani, O.A.M. Ali, R.M. Ramadan, J. Mol. Struct. 38 (2005) 171-177.

64 S.Y. Ebrahimipour, M. Abaszadeh, J. Castro, M. Seifi, Polyhedron 79 (2014) 138-150.

65 M. Kuriakose, M.R.P. Kurup, E. Suresh, Polyhedron 26 (2007) 2713-2718.

66 H. Dinda, P. Sengupta, S. Ghosh, T.C.W. Mak, Inorg. Chem. 41 (2002) 1684-1688.

67 Saswati, P. Adao, S. Majumder, S.P. Dash, S. Roy, M.L. Kuznetsov, J.C. Pessoa, C.S.B. Gomes, M.R. Hardikar, E.R.T. Tiekink, R. Dinda, Dalton Trans. 47 (2018) 11358-11374.

68 T.L. Riechel, L.J.D. Hayes, D.T. Sawyer, Inorg. Chem. 15 (1976) 1900-1904.

69 N. Patel, A.K. Prajapati, R.N. Jadeja, R.N. Patel, S.K. Patel, I.P. Tripathi, N. Dwivedi, V.K. Gupta, R. J. Butcher, Polyhedron 180 (2020)114434.

70 I.P. Tripathi, A. Kamal, M.K. Mishra, A. Dwivedi, R. Tripathi, C. Mishra, L. Shastri, Ind. J. Appl. Res. 4 (2014) 66-69.

71 S. Misra, K.B. Pandey, A.K. Tiwari, A.Z. Ali, T. Saradamani, S.B. Agawane, K. Madhusudana, Int. J. Nutr. Metab. 4 (2012) 11-18.

72 E. Apostolidis, Y.I.I. Kwon, K. Shetty, Asian Pac. J. Clin. Nutr. 15 (2006) 433-441.

73 N. Patel, AK Prajapati, R.N. Jadeja, I.P. Tripathi, N. Dwivedi, J. Coord. Chem. 73 (2020) 1131-1146.

74 S. Zhang, S.M. Kim, Appl. Organomet. Chem. 33 (2019) e5102.

75 J. Xio, X. Ni, G. Kai, X. Chem, Crit. Rev. Food Sci. Nutr. 53 (2013) 497-506.

76 G.A. Petersson, M.A. Al. -Laham, J. Chem. Phys. 94 (1991) 6081–6090.

77 P.J. Hay, W.R. Wadt, J. Chem. Phys. 82 (1985) 270–283.

78 M.J. Frisch, G.W. Trucks, H.B. Schlegel, G.E. Scuseria, M.A. Robb, J.R. Cheeseman, G. Scalmani, V. Barone, B. Mennucci, G.A. Petersson, H. Nakatsuji, M. Caricato, X. Li, H.P. Hratchian, A.F. Izmaylov, J. Bloino, G. Zheng, J.L. Sonnenberg, M. Hada, M. Ehara, K. Toyota, R. Fukuda, J. Hasegawa, M. Ishida, T. Nakajima, Y. Honda, O. Kitao, H. Nakai, T. Vreven, J.A. Montgomery Jr., J.E. Peralta, F. Ogliaro, M. Bearpark, J.J. Heyd, E. Brothers, K.N. Kudin, V.N. Staroverov, R. Kobayashi, J. Normand, K. Raghavachari, A. Rendell, J.C. Burant, S.S. Iyengar, J. Tomasi, M. Cossi, N. Rega, J.M. Millam, M. Klene, J.E. Knox, J.B. Cross, V. Bakken, C. Adamo, J. Jaramillo, R. Gomperts, R.E. Stratmann, O. Yazyev, A.J. Austin, R. Cammi, C. Pomelli, J.W. Ochterski, R.L. Martin, K. Morokuma, V.G. Zakrzewski, G.A. Voth, P. Salvador, J.J. Dannenberg, S. Dapprich, A.D. Daniels, O. Farkas, J.B. Foresman, J.V. Ortiz, J. Cioslowski, D.J. Fox, Gaussian 09, Revision D.01, Gaussian Inc., Wallingford CT, (2009).

79 R. Bauernschmitt, R. Ahlrichs, Chem. Phys. Lett. 256 (1996) 454–464.

80 M. Cossi, N. Rega, G. Scalmani, V. Barone, J. Comput. Chem. 224 (2003) 669–681.

81 T. Mossman, J. Immunol. 65 (1993) 55-63.

82 S. Ramakrishnan, M. Palaniandavar, Dalton Trans. 29 (2008) 3866–3878.

83 B. Murphy, M. Aljabri, A.M. Ahmed, G. Murphy, B.J. Hathaway, M.E. Light, T. Geilbrich, M.B. Hursthouse, Dalton Trans. 2 (2006) 357–367.

84 S. Ramakrishnan, D. Shakthipriya, E. Suresh, V.S. Periasamy, M.A. Akbarsha, M. Palaniandavar, Inorg. Chem. 50 (2011) 6458–6471.

85 B. J. Hathaway, P. G. Hodgson, Polyhedron 35 (1973) 4071–4081.

86 R.G. Par, R.G. Pearson, J. Am. Chem. Soc. 105 (1983) 7512-7516.

87 T.A. Koopmans, Z.U. Oie, Physica 1 (1934) 104-113.

88 R.G. Pearson, Chem. Sci. 117 (2005) 369-377.

89 F. Weinhold, C. Landis, Valency and bonding: A Natural Bond Orbital Donor-Acceptor Perspective, Cambridge University Press Cambridge (2005).

90 A.E. Reed, L.A. Curtius, F. Weinhold, Chem. Rev. 88 (1988) 899-926.

91 A.A. Soliman, M.A. Amin, A.M. Sayed, A.A.A.A. –Hussein, W. Linert, Polyhedron 161 (2019) 213-221.

Published Paper from this chapter

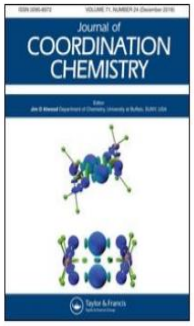

Journal of Coordination Chemistry

ISSN: 0095-8972 (Print) 1029-0389 (Online) Journal homepage: https://www.tandfonline.com/loi/gcoo20

Experimental, quantum computational study and *in vitro* antidiabetic activity of oxidovanadium(IV) complexes incorporating 2,2′-bis(pyridylmethyl)amine and polypyridyl ligands

Neetu Patel, A. K. Prajapati, R. N. Jadeja, I. P. Tripathi & N. Dwivedi

To cite this article: Neetu Patel, A. K. Prajapati, R. N. Jadeja, I. P. Tripathi & N. Dwivedi (2020): Experimental, quantum computational study and *in vitro* antidiabetic activity of oxidovanadium(IV) complexes incorporating 2,2'-bis(pyridylmethyl)amine and polypyridyl ligands, Journal of Coordination Chemistry, DOI: 10.1080/00958972.2020.1774562

To link to this article: https://doi.org/10.1080/00958972.2020.1774562